UW SSEC Pub#83.06.M2

Western Australian Institute of Technology

SCHOOL OF PHYSICS AND GEOSCIENCES

Report No.: SPG 320 / 1983 / AP 56

Notes On

SATELLITE METEOROLOGY

by

Dr. Paul Menzel
Visiting Fellow

June, 1983

This document is the accumulation of lecture notes from the course in Satellite Meteorology delivered in 1983 on the WAIT campus. Dr. Mervyn Lynch was most helpful in organizing the material for effective presentation. Ms. Deirdre Hollingsworth patiently typed the various versions of the notes. I thank them both.

TABLE OF CONTENTS

Table of Contents

(Cont'd)

LECTURE 1

EVOLUTION OF SATELLITE METEOROLOGY

Rocket probing of the atmosphere after World War II produced the first composite photographs of the top of the atmosphere. On 4 October 1957 the era of satellite meteorology began as the Soviets launched Sputnik I. The United States accelerated its program to launch the first meteorological satellite TIROS-1 on 1 April 1960. Global weather observations were realized immediately and the operational meteorological satellite program evolved rapidly thereafter. A total of 10 TIROS satellites were launched (the last on 2 July 1965) which carried vidicon camera systems for daytime visible imaging and passive infrared radiometers for sensing during both day and night. The Automatic Picture Transmission (APT) capability was developed in this time; very simple ground receivers could now receive real time satellite images.

The experimental TIROS series gave way to the ESSA satellites (9 in all from 1966 to 1969) which exploited the TIROS developments on a fully operational basis. In parallel the NIMBUS research satellite system continued testing remote sensing concepts and instruments. With the successful creation of global picture of the earth's surface and atmosphere accomplished in 1964, the primary emphasis shifted toward measuring the atmosphere's vertical distribution of temperature and moisture to better initialize global numerical weather prediction models.

Meteorological derivations from space are made through the electromagnetic radiation leaving the atmosphere. Outgoing radiation from earth to space varies with wavelength for two reasons:

(a) Planck function dependence on wavelength, and
(b) absorption by atmospheric gases of differing molecular structure hence differing wavelength (CO_2, H_2O, O_3.....).

Around absorbing bands of the constituent gases of the atmosphere, vertical profiles of atmospheric parameters can be derived. Sampling in the spectral region at the centre of the absorption band yields radiation from the upper levels of the atmosphere (e.g. radiation from below has already been absorbed by the atmospheric gas); sampling in spectral regions moving away from the center yields radiation from successivily lower levels of the atmosphere. Away from the absorption band are the windows to the bottom of the atmosphere. The IRIS (Infrared Interferometer Spectrometer) in 1969 observed surface temperatures of 320°K in the 11 μm window region of the spectrum and tropopause emissions of 210°K in the 15 μm absorption band. As the spectral region moves toward the center of the CO_2 absorption band, the radiation temperature decreases due to the decrease of temperature with altitude in the lower atmosphere.

The derivation of temperature profiles is complicated by the fact that upwelling radiance sensed at a given wavelength arises from a rather large vertical depth of the atmosphere. Weighting functions inherent in the radiative transfer equation show that the radiance arises from

deep overlapping layers for the spectral regions employed. This causes the radiance observations to be dependent and the inverse solution to the RTE for temperature profiles to be non-unique. Differing analytical approaches and types of ancillary data to constrain the solution will render temperature profiles.

Accurate temperature retrievals were accomplished with the SIRS (Satellite Infrared Spectrometer) aboard Nimbus-4 in 1969. Comparison with radiosonde observed profiles show the satellite derived T(p) to be very representative overall, with detailed vertical features smoothed out. The major problems with the early SIRS observations were induced by clouds which usually existed within the instrument's 225 Km field of view. Also the SIRS observed only along the suborbital track and consequently there were large gaps in data between orbits. In spite of these problems the SIRS data immediately showed promise of benefiting the current weather analysis/forecast operation and was put into operational use on 24 May 1969, barely a month after launch. For example the first numerical forecast impact experiment conducted for a meteorological situation on 24 June 1969 revealed that the inclusion of SIRS data in the analysis of 500 mb height over the Pacific was considerably different than that excluding the data. Namely, the SIRS data indicated a cut-off low with an intense jet to the north instead of a diffusely defined trough. Extended range (72 hr) forecasts for North America displayed maximum errors based on the analyses with SIRS of only half the magnitude of those resulting without the use of the data. Unfortunately, further forecast impact tests of NMC have shown both negative and positive impacts of the data and there was debate as to whether or not the negative results were due to a deficiency of the sounding data or to the deficiencies of the analysis/forecast system itself.

A scheme was soon devised for alleviating the influence of clouds with higher spatial resolution (30 Km) and spatially contiguous sounding observations possible with cross track scanning of the seven channel ITPR (Infrared Temperature Profile Radiometer) on board Nimbus 5 in 1972. In this adjacent field of view method, it is assumed that variation in radiance between two adjacent fields of view is due to cloud amount only. Consequently, the cloud radiance can be eliminated and the clear column radiance for any channel can be expressed in terms of the observed radiances for the two fields of view and a parameter, N*, which is equal to the ratio of the amounts of cloud for the two fields. N* can be obtained from radiances observed in the window channel and the Planck radiance corresponding to a known surface temperature. The ITPR concept was highly successful in alleviating the influence of clouds on the synoptic scale. In fact, soundings to the earth's surface could be achieved with an average spacing of 250 n.mi.over 95% of the globe.

Also on board Nimbus 5 was the first microwave sounding device NEMS (Nimbus Experimental Microwave Spectrometer), a nadir viewing 5 channel instrument. The NEMS demonstrated the capability to probe through clouds, even dense overcast. Good comparisons of ITPR, NEMS, and radiosonde data were achieved. It was found, however, that best results were achieved from an amalgamation of infrared and microwave radiance data in the temperature profile inversion process thereby providing the maximum available thermal information, regardless of cloud condition.

From the available results and studies, in the early 1970's it was recognized that the optimum temperature profile results would be achieved by taking advantage of the unique characteristics offered by the 4.3 μm, 15 μm, and 0.5 cm absorption bands. As a consequence, the Nimbus-6 HIRS (High resolution Infra-Red Sounder) experiment was designed to accommodate channels in both the 4.3 μm and 15 μm regions and these were complimented by the 0.5 cm microwave wavelength O_2 channels of SCAMS (Scanning Microwave Spectrometer). The HIRS also was designed with passively cooled detectors to allow for complete cross-track scanning and the SCAMS also scanned but with lower spatial resolution. The HIRS experiment successfully demonstrated an improved sounding capability in the lower troposphere due to the inclusion of the 4.3 μm observations.

The operational implementation of these instruments was achieved on the TIROS-N/NOAA space craft in 1978 which carry the HIRS (High resolution Infra-Red Spectrometer) and the MSU (Microwave Sounding Unit). The weighting functions have been carefully selected to cover the depth of the atmosphere. Infrared soundings of 30 Km resolution horizontally are supplemented with microwave soundings of 150 Km resolution horizontally. Amalgamation of data from two overpasses readily reveals the thermal patterns across the US as observed by the microwave midtropospheric sensing of brightness temperatures. A TIROS-N derived 500-mb height analysis compares well with the standard forecast products. The complement of infrared and microwave instruments aboard each of the polar orbiting spacecraft provided a complete global coverage of vertical temperature and moisture profile data every 12 hours at 250 Km spacing.

Another very important tool for sounding data interpretation was developed during the 1970's, Man Computer Interactive Data Access System (McIDAS). The development of the man-machine interactive processing capability, for example the McIDAS system at the University of Wisconsin, has been shown to enable soundings with high quality and resolution to be obtained through manual editing and enhancement of the data. Utilizing a terminal consisting of digital, video and graphics display devices and cursors and typedeck consoles for communicating instructions to the processor, an operator is able to rapidly interact with the data processing. For example, the operator can display images of sounding radiance data to aid him in selecting important meteorological phenomena and regions of extensive cloudiness where manual intervention is needed to insure high quality sounding output. The operator can instruct the computer to zoom in on the meteorologically active area and produce soundings which the operator can subjectively edit and enhance through the addition of soundings at specific locations selected by the operator through cursor control. The operator can check the meteorological consistency of the satellite sounding data. For example, he can instruct the computer to compute 300 mb geopotential heights and from their horizontal gradients thermal winds. Through cursor positioning, a sounding which is obviously erroneous, in that it was responsible for an unrealistic thermal wind, can be rapidly eliminated. The McIDAS application to satellite sounding data has also led to rapid improvements in the algorithms used to process the data since visual inspection of the results revealed deficiencies in the processing procedures.

For meteorological applications, two types of satellite orbits have

been employed. Thus far we have discussed instruments on the polar sun-synchronous orbit from which global observations can be collected every twelve hours. The other orbit, the geostationary orbit above the equator, has a period of 24 hours and thereby enables continuous surveillance of the weather. Polar orbits range from 600 to 1600 Km in altitude, whereas the geostationary altitude is 38000 Km.

Instantaneous hemispheric viewing was first accomplished with the Application Technology Satellites (ATS) which were launched into geostationary orbit starting in 1967 with ATS-1. These satellites carried the spin scan camera which enabled half hourly hemispheric visible viewing. Thus began the time domain observation of weather patterns. Geostationary IR imaging came soon thereafter, and the SMS and GOES spacecraft for the next ten years all carried a spin scan camera for visible and infrared images that the public has become familiar with.

With the launch of the VISSR (Visible Infrared Spin Scan Radiometer) Atmospheric Sounder (VAS) in September 1980, the era of geostationary sounding began. Time continuous 3-dimensional probing of the atmosphere is accomplished using 12 infrared spectral bands in an imaging or a sounding mode. A filter wheel in front of the detector package is used to achieve the spectral selection. The central wavelengths of the spectral bands lie between 3.9 and 15 μm. The VAS radiometer observes upwelling radiation in two windows (4.0 μm and 11 μm), three water vapour channels, and seven regions of the 4.3 μm and 15 μm CO_2 bands. Housed in the GOES satellite, VAS spins in a west to east direction at 100 rpm and achieves spatial coverage at resolutions of 1 Km in the visible and 7 or 14 Km in the infrared (depending upon the detector employed) by stepping a scan mirror in a north to south (or vice versa) direction.

Designed for multipurpose applications, the VAS can be operated in two different modes:

a) a multi-spectral imaging (MSI) mode, and
b) a dwell sounding (DS) mode.

Within each mode of operation there is a wide range of options regarding spatial resolution (7 Km or 14 Km), spectral channels, spatial coverage, and the time frequency of observation. The mode of operation is programmed into an onboard processor from the ground through 39 processor parameters.

The DS mode of operation permits multiple samples of the upwelling radiance from a given earth swath in a given spectral band to be sensed by leaving the filter position and mirror position fixed during multiple spins of the spacecraft. The DS mode of operation was designed to achieve the improved signal-to-noise ratios required to interpret the spectral radiance measurements in terms of vertical temperature and moisture structure. Spatial averaging of several 14 Km resolution observations may be employed to further improve the sounding radiance signal-to-noise ratio. Soundings over the North American region (20° to 55° N) can be achieved at half hour frequency.

The MSI mode of operation is intended to achieve relatively frequent (e.g. half hourly) full earth disc imagery of the atmosphere's water vapour, temperature, and cloud distribution as well as the earth's surface skin temperature variation. In order to achieve full disc coverage at half hourly intervals either:

(a) four spectral channels can be observed; the visible at 1 Km

resolution, the 11 μm window, at 7 Km resolution, and two others at 14 Km resolution or

(b) five spectral channels can be observed; the visible at 1 Km resolution and any four infrared spectral channels at 14 Km resolution.

The VAS is capable of vertically sounding the atmosphere from a geostationary altitude with the same accuracy as that achieved by infrared sounders on polar orbiting spacecraft. Initial results of the VAS vertical sounding capability have already demonstrated the novel capability of sensing the temporal variations in atmospheric temperature and moisture as well as the small scale horizontal features.

The advantage of continuous monitoring is well demonstrated in the case of 26 April 1982 over Alabama, US. The cloud picture shows no impending severe weather development over Alabama, but the VAS derived stability index (an empirical measure of thermodynamic stability of the atmosphere) indicates a high probability for tornadic activity if it registers above 60. The subsequent time of thunderstorms over southern Alabama spawned seven tornados in late afternoon at 21Z. VAS was able to depict the state of the atmosphere and then monitor changes in relevant atmospheric parameters.

Future developments in the satellite program will see different approaches to the existing problems; the need for higher vertical and horizontal resolution in the soundings and for microwave help in the area of clouds. The AMSU (Advanced Microwave Sounding Unit) with 20 microwave channels is scheduled for polar orbiting launch in the early 1990's and the HIS (High resolution Interferometer Sounder) is slated for geostationary 3-axis stabilized platform performance in the same time frame.

LECTURE 2

REMOTE SENSING OF RADIATION

Radiation is defined as a process whereby energy is transferred across space without the necessity of a material medium (in contrast with conduction, convection, or advection). The observation of a target by a device separated from it by some distance is the act of remote sensing (ears are remote sensors via sensing acoustic waves). Remote sensing with satellites for meteorological research has been restricted to passive detection of radiation emanating from the earth-atmosphere system.

BASIC UNITS

All forms of electromagnetic radiation travel in a vacuum at the same velocity, which is approximately 3×10^{10} cm/sec and is denoted by the letter c. Electromagnetic radiation is propogated as waves. For many applications it is sufficient to consider the waves as being a continuous train of sinusoidal shapes.

If radiation is of only one colour it is said to be monochromatic. The colour of any particular kind of radiation is designated by its frequency, which is the number of waves passing a given point in one second, and is represented by the letter f(Hz). The length of a single wave (i.e., the distance between two successive maxima) is called the wavelength and is denoted by λ(cm).

If for monochromatic radiation one were to count the number of waves passing a fixed point in one second, and then multiply that number by the length of each wave, that would be the distance the wave train travelled in one second. But that distance is given by the velocity of light c. Hence,

$$c = f\lambda = 3 \times 10^{10} \text{ cm/sec}$$

or

$$f = c/\lambda \text{ (cycles/sec)}$$

Since the frequency f of a wave is equal to the number of wavelengths in a distance of 3×10^{10} cm, it is usually a large number. It is much more convenient (especially in the infrared region of the spectrum) to speak of the number of waves in one centimeter and call the new unit the wavenumber designated $\nu(\text{cm}^{-1})$, that is,

$$\nu = 1/\lambda \ (\text{cm}^{-1}).$$

However, wavenumber becomes a relatively small unit in the microwave region; therefore, we use frequency in gigahertz units in that region. Similarly, because wavelength units in centimeters are generally small, we use micrometers (μm) for most of the spectrum and for the very short wavelength region we use Angstrom units (Å). Conversion of wavelength units is as follows:

$$1\text{Å} = 10^{-10} \text{ m} = 10^{-8} \text{ cm} = 10^{-4} \ \mu\text{m},$$

and

$$1\mu\text{m} = 10^{-6} \text{ m} = 10^{-4} \text{ cm} = 10^{4} \text{ Å}.$$

Note that a micrometer sometimes is called a micron and is denoted μ. Conversion of frequency units is as follows:

$$1 \text{ cm}^{-1} = 3 \times 10^{10} \text{ Hz} = 30 \text{ GHz},$$

and

$$1 \text{ GHz} = 10^{9} \text{ Hz} = 1/30 \text{ cm}^{-1}.$$

Table 1 summarizes the regions and units of the electromagnetic spectrum.

DEFINITIONS OF RADIATION

The rate of energy transfer by electromagnetic radiation is called the radiant flux, which has units of energy per unit time: joules per second or watts. For example the radiant flux from the sun is about 3.90×10^{26} W.

By dividing the radiant flux by the area through which it passes, we obtain the irradiance which is expressed in units of watts per square meter and denoted by the symbol E. The irradiance of electromagnetic radiation passing through the outermost limits of the visible disk of the sun (which has an approximate radius of 7×10^{8} m) is given by

$$\frac{3.90 \times 10^{26}}{4\pi(7 \times 10^{8})^{2}} = 6.34 \times 10^{7} \text{ W m}^{-2}$$

In discussing the theory of radiative transfer, we will have occasion to speak of the radiation having wavelengths within a particular infinitesimal wavelength interval of the electromagnetic spectrum. The irradiance per unit wavelength interval at wavelength λ is called the monochromatic irradiance E_λ, which has the units of watts per square meter per micrometer. With this definition, the irradiance is readily seen to be

$$E = \int_{0}^{\infty} E_\lambda \, d\lambda$$

In general, the irradiance upon an element of surface area may consist of contributions which come from an infinity of different directions. It is sometimes necessary to identify the part of the irradiance that is coming from directions within some specified infinitesimal arc of solid angle $d\Omega$. For this purpose it is useful to define the radiance L, which is the irradiance per unit solid angle, expressed in watts per square meter per steradian. This quantity is often also referred to as intensity and denoted by the letter I (or B when referring to the Planck function).

In order to express quantitatively the relationship between irradiance and radiance, it is necessary to define the zenith angle θ, which is the angle between the direction of the radiation and the normal to the surface in question. The component of the radiance normal to the surface is then given by $L \cos \theta$. The irradiance represents the combined effects of the normal component of the radiation coming from the whole hemisphere; that is,

$$E = \int_{\Omega} L \cos \theta \, d\Omega$$

where in spherical coordinates

$$d\Omega = \sin \theta \, d\theta \, d\phi.$$

Figure 1 illustrates the radiance geometry.

For isotropic radiation it can be readily shown that

$$E = \pi L.$$

Table 1: Regions and units of the electromagnetic spectrum.

	WAVELENGTH (λ)			FREQUENCY (f) (cycles/sec)		WAVENUMBER (ν)
	cm	μm (microns)	Å	Hz	GHz	cm^{-1}
NEAR ULTRAVIOLET (UV)	10^{-5}	0.1	1000	3×10^{15}		
VISIBLE	4×10^{-5}	0.4	4000	7.5×10^{14}		
NEAR INFRARED (IR)	7.5×10^{-5}	0.75	7500	4×10^{14}		13,333
FAR INFRARED (IR)	2×10^{-3}	20	200,000	1.5×10^{13}		500
MICROWAVE (MW)	0.1	10^{4}		3×10^{11}	300	10
	10	10^{6}		3×10^{9}	3	0.1

HISTORICAL DEVELOPMENT OF PLANCK'S RADIATION LAW

It had long been observed that the surface of all bodies at a temperature greater than absolute zero ($0^{o}K$) emits energy, in the form of thermal radiation. These electromagnetic waves were throught to be due to the motion of electric charges near the surface of the radiating body.

The study of radiation focussed on the properties of a hypothetical black body, which is characterized by

a) complete absorption of all incident radiation (hence the term black), and

b) maximum possible emission in all wavelengths in all directions.

In other words, it is the perfector absorber and emitter of all radiation.

Many attempts, both empirical and theoretical in approach, were made in the years up to and about 1900 to understand the black body spectrum. In 1879, Stefan had empirically found that the irradiance of a black body was related to temperature by the law

$$E = \sigma T^{4}$$

where $$\sigma = 5.67 \times 10^{-8} \text{ W m}^{-2} \text{ deg}^{-4}.$$

In 1884, Boltzmann produced a theoretical derivation of this equation.

Earliest accurate measurements of monochromatic irradiance are credited to Lummer and Pringsheim in 1899. They observed the now well known emission spectra for black bodies at several different temperatures (shown in Figure 2).

Thermodynamical reasoning, while not giving a complete answer, did predict two characteristic features of the radiation. Wien in 1893 was able to show that the monochromatic radiance was related to temperature and wavelength by

$$I_{\lambda} = \frac{f(\lambda T)}{\lambda^{5}},$$

where the form of the single function $f(\lambda T)$ was not evaluated. Also the peak emission wavelength of a black body was shown to be inversely proportional to temperature, so that

$$\lambda_{max} = \frac{\text{constant}}{T}.$$

In this derivation, he considered a cylindrical cavity with reflecting walls, one of which is a moveable piston, filled with radiation at a temperature T. Radiation was known to exert a pressure proportional to its energy density. Taking this system through a Carnot cycle, a relation between the work done by the radiation (expressed in terms of monochromatic radiance) and temperature was obtained.

To evaluate the function $f(\lambda T)$ some of the detailed properties of a black body must be taken into account. In 1900 Rayleigh and Jeans attempted to evaluate $f(\lambda T)$ by considering a cubical cavity containing electromagnetic standing waves with nodes at the metallic surfaces and the energy of these waves obeying the Boltzmann probability distribution. Assuming a continuum of energy states, the average total energy of this system can be expressed as

$$\bar{\varepsilon} = \frac{\int_0^\infty \varepsilon\, e^{-\varepsilon/kT}\, dt}{\int_0^\infty e^{-\varepsilon/kT}\, dt} = kT$$

where the Boltzmann constant

$$k = 1.281 \times 10^{-23} \text{ J deg}^{-1}.$$

This leads to $f(\lambda T) = 2ck\lambda T$ which is in agreement with experiment only for long wavelengths. At short wavelengths the monochromatic radiance becomes infinite (often referred to as the ultraviolet catastrophe). The form of $f(\lambda T)$ obtained by Rayleigh and Jeans was a necessary consequence of the theories of classical physics, yet it failed!

The discrepancy between experiment and theory was resolved by Planck in 1901, but at the expense of some of the concepts known to classical physics. Assuming that electromagnetic harmonic oscillations can only exist in quanta of hf (h is a constant, f is frequency) and that oscillators emit energy only when changing from one to another of their quantized energy states, then the average total energy of this system is expressed as

$$\bar{\varepsilon} = \frac{\sum_{n=0}^{\infty} nhf\, e^{-nhf/kT}}{\sum_{n=0}^{\infty} e^{-nhf/kT}},$$

or

$$\bar{\varepsilon} = \frac{hf}{e^{hf/kT} - 1}.$$

This yields the proper form of $f(\lambda T)$,

$$f(\lambda T) = \frac{2hc^2}{(e^{hc/\lambda kT} - 1)}$$

and predicts the observed results if the Planck constant

$$h = 6.63 \times 10^{-34} \text{ J.s}.$$

And the Planck law for radiation intensity (or monochromatic radiance) can be expressed as

$$B(\lambda,T) = \frac{c_1}{\lambda^5 (e^{c_2/\lambda T} - 1)}$$

where $c_1 = 2hc^2 = 1.191066 \times 10^{-8} \text{ W/(m}^2\text{.ster.cm}^{-4}\text{)}$

$$c_2 = \frac{hc}{k} = 1.438833 \text{ }^{\circ}\text{K.cm}$$

and $B(\lambda,T)$ has units of $W/(m^2.ster.cm)$.

Written in terms of wavenumber rather than wavelength,

$$B(\nu,T) = \frac{c_1 \nu^3}{e^{c_2 \nu/T} - 1},$$

and $B(\nu,T)$ has units of $W/(m^2.ster.cm^{-1})$.

Thus in the course of his successful attempt at resolving certain discrepancies between the observed energy spectrum of thermal radiation and the predictions of the classical theory, Planck was led to the idea that a system executing simple harmonic oscillations only can have energies which are integral multiples of a certain finite amount of energy (1901). A closely related idea was later applied by Einstein in explaining the photoelectric effect (1905), and by Bohr in a theory which predicted with great accuracy many of the complex features of atomic spectra (1913). The work of these three physicists, plus subsequent developments by de Broglie, Schroedinger, and Heisenberg (ca. 1925), constitutes what is known as the quantum theory. This theory and the theory of relativity together comprise the two most significant features of modern physics.

RELATED DERIVATIONS

1. Weins Displacement Law

The peak of Planck function curves shifts to shorter wavelengths with an increase in temperature. The wavelength λ_{max} for which the Planck function peaks at a given temperature T can be found from Planck's law by differentiating it with respect to λ and equating the result to zero. This yields the nonlinear equation

$$x = 5(1-e^{-x}),$$

where $x = c_2/(\lambda_{max}T)$, whose solution is $x = 4.965114$, that is,

$$\lambda_{max} = \frac{.2897}{T} \text{ (cm)}$$

which is Wien's displacement law. This law indicates that the wavelength of maximum Planck radiance varies inversely with temperature.

The radiative temperature of the surface of the sun is 5780 K. Multiplying the Wien Equation by 10^4 to change it to μm units and applying the sun's surface temperature, one finds the maximum Planck radiance to be at 0.50 μm, which is near the centre of the visible region of the spectrum. Since the sun radiates nearly as a black body, we can say that the solar energy reaching the earth is a maximum in the visible region.

On the other hand, the earth's atmospheric temperature averaged vertically is around 255 K; therefore, the maximum emitted energy of the earth's atmosphere occurs roughly at 11 μm, that is, well into the infrared region. In fact, if the black body curves (Planck functions) for temperatures of 255 K and 5780 K are plotted next to each other, the two curves are almost entirely separate. Thus, the spectral distribution of the incoming solar radiation is quite different from that of the outgoing terrestrial radiation. See Figure 3.

Wien's displacement law derives its name from the fact that as the temperature increases, the point of maximum intensity of the black body curve is displaced toward the shorter wavelengths. Since the wavelength of the maximum value determines the colour perceived while observing the complete spectrum, we have an explanation for the transition in colour of a heated iron bar from red to a white glow with increased heat. As the temperature is raised the longer wavelength

red light becomes visible first. Then higher temperatures make additional wavelengths visible. Finally, when the temperature is sufficiently high, the radiation consists of a mixture of all the visible wavelengths and, hence, appears white hot. For similar reasons the filament of an incandescent lamp must be heated to thousands of degrees K in order to be an efficient emitter of visible light, while infrared lamps operate at lower temperatures.

2. Rayleigh-Jeans Radiation Law

In the microwave region of the electromagnetic spectrum, when $\lambda \geq 0.5$ cm and T is at terrestrial temperatures, the exponent in the Planck function is small, and hence one can make the approximation

$$e^{c_2/\lambda T} = 1 + c_2/\lambda T ,$$

which yields the following asymptotic expansion:

$$B(\lambda,T) = \frac{c_1}{c_2} \frac{T}{\lambda^4} .$$

Similarly,

$$B(\nu,T) = \frac{c_1 \nu^2 T}{c_2}$$

for sufficiently small ν. These formulas represent the Rayleigh-Jeans law of radiation and the spectral region $\lambda \geq 0.5$ cm is called the Rayleigh-Jeans region in atmospheric physics. Note that in the Rayleigh-Jeans region the Planck function is linear to T.

3. Wien's Radiation Law

In the near infrared region and beyond into the visible and ultraviolet regions, i.e., $\lambda \leq 10^{-3}$ cm, and when T is at terrestrial temperatures, the exponent in the Planck function is large and, hence

$$e^{c_2/\lambda T}$$

is large relative to 1.0. Consequently, the constant 1.0 can be ignored in the denominator to yield another asymptotic expansion for the Planck function, namely,

$$B(\lambda,T) = \frac{c_1}{\lambda^5} e^{-c_2/\lambda T}$$

or

$$B(\nu,T) = c_1 \nu^3 e^{-c_2 \nu/T}$$

for sufficiently large ν. These are two forms of Wien's law of radiation. The spectral region $\lambda \leq 10^{-3}$ cm is called the Wien region when dealing with atmospheric temperatures. In the Wien region the Planck function is highly nonlinear in temperature.

Figure 4 shows the regions of validity of the Wien and Rayleigh-Jeans laws. The amount of departure of the solid lines from the dashed line is an indication of the error introduced when substituting the asymptotic values for the true Planck values.

4. Stefan-Boltzmann Law

The black body irradiance is obtained by integrating the Planck function over all wavelengths and angles,

$$E = \int_o^\infty E_\lambda \, d\lambda = \pi \int_o^\infty \frac{c_1 \, d\lambda}{\lambda^5 \left| e^{c_2/\lambda T} - 1 \right|}$$

Let $x = c_2/\lambda T$ then

$$E = \frac{\pi \, c_1 T^4}{c_2^4} \int_o^\infty \frac{x^3 \, dx}{(e^x - 1)}$$

$$= \frac{\pi^5 c_1}{15 \, c_2^4} T^4$$

$$= \sigma T^4$$

5. Radiance Temperature

Ultimately one is interested in the temperature that corresponds to a particular Planck function value B_λ. This temperature is determined by inverting the Planck function,

$$T = \frac{c_2}{\lambda \ell n\left(\frac{c_1}{\lambda^5 B_\lambda} + 1\right)} = \frac{c_2 \nu}{\ell n\left(\frac{c_1 \nu^3}{B_\nu} + 1\right)}$$

The temperature derived is called brightness temperature because of its historical connection with radio astronomy; however, the preferred usage is radiance temperature or equivalent black body temperature.

In the Rayleigh-Jeans region, one can write

$$T = \left(\frac{c_2}{c_1}\right) \lambda^4 B_\lambda = \left(\frac{c_2}{c_1}\right) \frac{B_\nu}{\nu^2} \, ,$$

where $c_2/c_1 = 1.208021 \times 10^5$. On the other hand in the Wien region

$$T = \frac{c_2}{\lambda \ell n(c_1/\lambda^5 B_\lambda)} = \frac{c_2 \nu}{\ell n(c_1 \nu^3 / B_\nu)} \, .$$

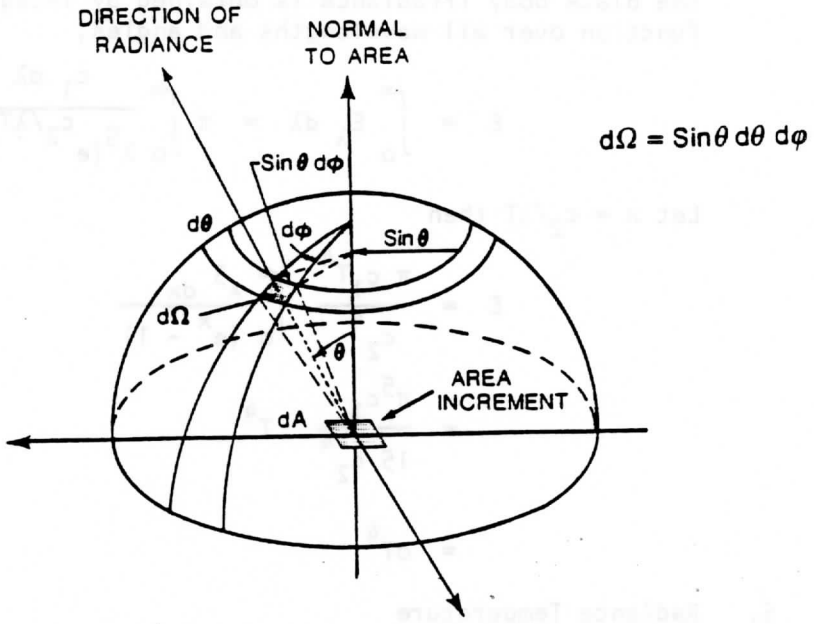

FIGURE 1: The Radiance Geometry

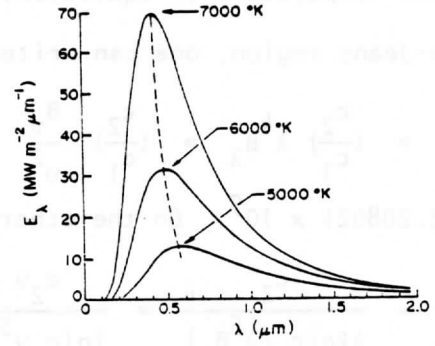

FIGURE 2: Emission Spectra for Black Bodies with the Indicated Temperatures

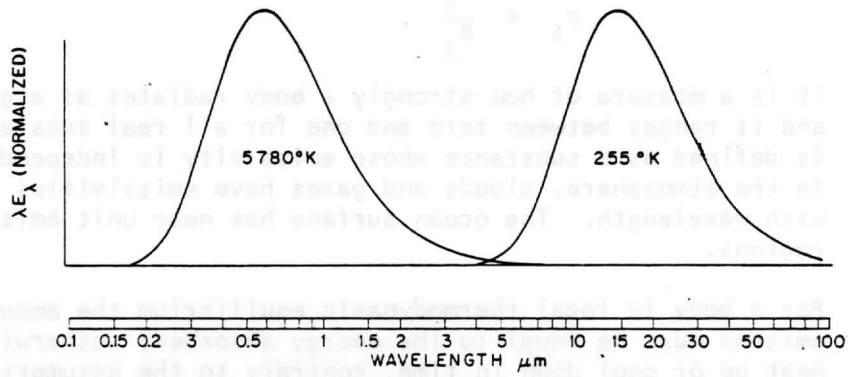

FIGURE 3: Normalized blackbody spectra representative of the sun (left) and earth (right), plotted on a logarithmic wavelength scale. The ordinate is multiplied by wavelength in order to make area under the curves proportional to irradiance.

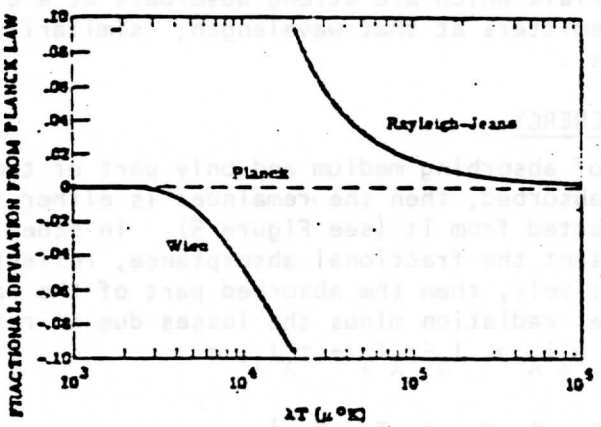

FIGURE 4: Deviations of Wien and Rayleigh-Jeans expressions from Planck's law.

LECTURE 3

ABSORPTION AND EMISSION

As we noted earlier, black body radiation represents the upper limit to the amount of radiation that a real substance may emit at a given temperature. At any given wavelength λ, emissivity is defined as the ratio of the actual emitted radiance, R_λ, to that from an ideal black body, B_λ,

$$\varepsilon_\lambda = \frac{R_\lambda}{B_\lambda} .$$

It is a measure of how strongly a body radiates at a given wavelength, and it ranges between zero and one for all real substances. A gray body is defined as a substance whose emissivity is independent of wavelength. In the atmosphere, clouds and gases have emissivities that vary rapidly with wavelength. The ocean surface has near unit emissivity in the visible regions.

For a body in local thermodynamic equilibrium the amount of thermal energy emitted must be equal to the energy absorbed; otherwise the body would heat up or cool down in time, contrary to the assumption of equilibrium. In an absorbing and emitting medium in which I_λ is the incident spectral radiance, the emitted spectral radiance R_λ is given by

$$R_\lambda = \varepsilon_\lambda B_\lambda = a_\lambda I_\lambda ,$$

where a_λ represents the absorptance at a given wavelength. If the source of radiation is in thermal equilibrium with the absorbing medium

$$I_\lambda = B_\lambda$$

so that $$\varepsilon_\lambda = a_\lambda .$$

This is often referred to as Kirchoffs Law. In qualitative terms it states that materials which are strong absorbers at a given wavelength are also strong emitters at that wavelength; similarily weak absorbers are weak emitters.

CONSERVATION OF ENERGY

Consider a slab of absorbing medium and only part of the total incident radiation I is absorbed, then the remainder is either transmitted through the slab or reflected from it (see Figure 5). In other words, if a_λ, r_λ, and τ_λ represent the fractional absorptance, reflectance, and transmittance, respectively, then the absorbed part of the radiation must be equal to the total radiation minus the losses due to reflections away from the slab. Hence $a_\lambda I_\lambda = I_\lambda - r_\lambda I_\lambda - \tau_\lambda I_\lambda$, or

$$a_\lambda + r_\lambda + \tau_\lambda = 1$$

which says that the processes of absorption, reflection, and transmission account for all the incident radiation in any particular situation and is known as the conservation of energy. Since for a black body $a_\lambda = 1$, it

follows that $r_\lambda = o$ and $\tau_\lambda = 0$ for black body radiation. Also, in any window region, if $\tau_\lambda = 1$, then $a_\lambda = 0$ and $r_\lambda = 0$.

Monochromatic radiation incident upon any opaque surface, $\tau_\lambda = 0$, is either absorbed or reflected, so that

$$a_\lambda + r_\lambda = 1$$

At any wavelength, strong reflectors are weak absorbers (for example, snow at visible wavelengths), and weak reflectors are strong absorbers (for example, asphalt at visible wavelengths). The reflectances for selected surfaces for the wavelegnths of solar radiation are listed in Table 2.

From Kirchoffs Law we can also write

$$\varepsilon_\lambda + r_\lambda + \tau_\lambda = 1$$

which says that emission, reflection, and transmission account for all the incident radiation for media in thermodynamics equilibrium.

PLANETARY ALBEDO

Planetary albedo is defined as the fraction of the total incident solar radiation, S, that is reflected back into space. Radiation balance then requires that the absorbed solar irradiance is given by

$$E = (1 - A)\, S/4.$$

The factor of one fourth arises because the cross sectional area of the earth disc to solar radiation (πr^2) is one fourth the earth radiating surface ($4\pi r^2$). Thus if the earth albedo is 30%, then $E = 241\ Wm^{-2}$.

SELECTIVE ABSORPTION AND EMISSION

The atmosphere of the earth exhibits absorptance which varies drastically with wavelength. In the visible part of the spectrum the absorptance is small while in the infrared it is large. This has a profound effect on the equilibrium temperature at the surface of the earth. The following problem illustrates this point. Assume that the earth behaves like a black body and that the atmosphere has a absorptivity a_S for incoming solar radiation and a_L for outgoing longwave radiation. Let Y_a be the irradiance emitted by the atmosphere (both upwards and downwards); Y_s the irradiance emitted from the earths surface; and E the solar irradiance absorbed by the earth-atmosphere system. Then at the surface, radiative equilibrium require

$$(1-a_S)E - Y_s + Y_a = 0\ ,$$

and at the top of the atmosphere

$$E - (1-a_L)Y_s - Y_a = 0\ .$$

Solving yields

$$Y_s = \frac{(2-a_S)}{(2-a_L)}\ E\ ,$$

and since $a_L > a_S$ the irradiance and hence the radiative equilibrium temperature at the earth surface is increased by the presence of the atmosphere. Typically $a_L = .8$ and $a_S = .1$ and $E = 241\ Wm^{-2}$ so the black body temper-

ature at the surface is 277°K, in contrast to the 255°K it would be if the atmospheric absorptance was independent of wavelength ($a_S = a_L$).

Whenever a gas that is a weak absorber in the visible and a strong absorber in the infrared is a constituent of a planetary atmosphere, it contributes toward raising the surface temperature of the planet. The warming results from the fact that incoming radiation can penetrate to the ground with relatively little absorption, while much of the outgoing longwave radiation is 'trapped' by the atmosphere and emitted back to the ground. In order to satisfy the radiation balance the surface must compensate by emitting more radiation than it would in the absence of such an atmosphere. To emit more it must radiate at a higher temperature.

The trapping of the longwave radiation also can explain the gradual decrease of effective black body temperature of atmospheric layers as altitude increases. Expanding on the previous example, let the atmosphere be represented by two layers and let us compute the vertical profile of radiative equilibrium temperature. For simplicity in our multilayer atmosphere, let $a_S = 0$ and $a_L = .5$.

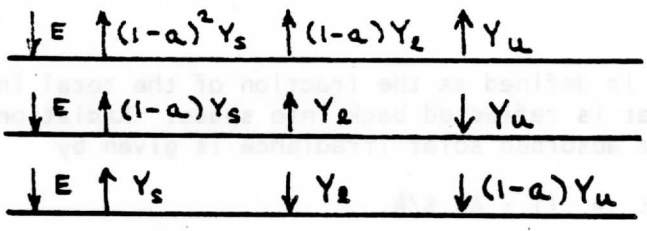

Radiative equilibrium at each surface requires

$$E = .25\,Y_s + .5Y_l + Y_u ,$$

$$E = .5\,Y_s + Y_l - Y_u ,$$

$$E = Y_s - Y_l - .5Y_u .$$

Solving yields $Y_s = 1.6E$, $Y_l = .5E$ and $Y_u = .33E$. The radiative equilibrium temperatures are readily computed.

$$T_s = \left[\frac{1.6E}{\sigma}\right]^{\frac{1}{4}} = 290^{\circ}K$$

$$T_l = \left[\frac{.5E}{.5\sigma}\right]^{\frac{1}{4}} = 255^{\circ}K$$

$$T_u = \left[\frac{.33E}{.5\sigma}\right]^{\frac{1}{4}} = 231^{\circ}K$$

And thus a crude temperature profile emerges for this simple two layer model of the atmosphere.

ABSORPTION (EMISSION) LINE FORMATION

The Planck explanation of the continuous spectra of the black body was founded in the idea of quantization of available energy levels. Planck successfully explained the nature of radiation from heated solid objects of

which the cavity black body radiator formed the prototype. Such radiation generates continuous spectra and is contrary to line spectra. However, when properly extended, the theory of quantization also lead to the understanding of the line spectra of the atom. Let us investigate the development of the Bohr atomic model briefly.

In 1913 Bohr postulated that a) the angular momentum of the electrons in their circular orbits about the nucleus were quantized,

$$mvr = nh/2\pi$$

where m is the electron mass, v the velocity, r the radius, n the quantum number, and h Planck's constant, and b) the atoms radiate (absorb) only when the electron makes a transition from one energy state to another state of lower (higher) energy

$$E_{n_2} - E_{n_1} = hf .$$

The mechanical stability of the electron in a circular orbit about a proton is given by the Coulomb force offset by the centrifugal force

$$\frac{e^2}{r^2} = \frac{mv^2}{r}$$

where e is the electron charge. The total energy of the electron n^{th} state

$$E_n = \frac{1}{2} mv^2 - \frac{e^2}{r}$$

$$= \frac{2\pi^2 me^4}{h^2} \frac{1}{n^2} .$$

Therefore the frequency of the emission (absorption) lines in the hydrogen spectrum is given by

$$f = \frac{2^2 me^4}{h^3} \left(\frac{1}{n_2^2} - \frac{1}{n_1^2} \right)$$

$$= K \left(\frac{1}{n_2^2} - \frac{1}{n_1^2} \right)$$

where $K = 3.28 \times 10^{15}$ Hz.

Monochromatic emission is practically never observed. Energy levels during energy transitions are normally changed slightly due to external influences on atoms and molecules, and due to the loss of energy in emission. As a consequence, radiation emitted during repeated energy transitions is nonmonochromatic, and spectral lines of finite widths are observed. The broadening of spectral lines is caused by (1) the damping of vibrations of oscillators resulting from the loss of energy in emission (the broadening of lines in this case is considered to be normal), (2) the perturbations due to reciprocal collisions between the absorbing molecules, and between the absorbing and nonabsorbing molecules, and (3) the Doppler effect resulting from the difference in thermal velocities of atoms and molecules. The broadening of lines due to the loss of energy in emission (natural

broadening) is practically negligible as compared with that caused by collisions and the Doppler effect. In the upper atmosphere, we find a combination of collision broadening and Doppler broadening, whereas in the lower atmosphere, below about 40 km, the collision broadening prevails because of the pressure effect.

In general, spectral lines are assumed to be symmetric about the central wavelength λ_o which corresponds to a maximum absorbing power. In the case of a symmetric line, well separated from neighbouring lines of the absorption spectrum. the line shape may be fitted by the Lorentz form

$$K_\lambda = \frac{K_o \alpha^2}{(\lambda - \lambda_o)^2 + \alpha^2}$$

where K is a measure of the absorbing power and α is the half width of the line. The half width is the displacement from the line center to the wavelength where $K_\lambda = K_o/2$. In such an individual spectral line, the absorbing power approaches zero asymptotically at increasing distance in the line wings from the center. More generally, however, the absorbing power does not become zero between lines because of the overlapping effects of many lines.

THE SOLAR SPECTRUM

The distribution of electromagnetic radiation emitted by the sun as a function of the wavelength incident on the top of the atmosphere is called the solar spectrum. The solar constant S is a quantity denoting the amount of total solar energy reaching the top of the atmosphere. It is defined as the flux of solar energy (energy per time) across a surface of unit area normal to the solar beam at the mean distance between the sun and earth. The solar spectrum and solar constant have been the topics of extensive investigations for a long period of time. Abbot undertook a long series of ground-based measurements, resulting in a value of about 1350 Wm^{-2} for the solar constant. Subsequent to Abbot's work and prior to more recent measurements carried out from high-altitude platforms, solar constant values of 1396 and 1380 Wm^{-2} proposed by Johnson and Nicolet, respectively, were widely accepted. The Earth Radiation Budget Experiment (ERBE) has been monitoring the sun's radiation since July 1985. The solar constant measurements from Nimbus 7 indicate a value of 1372 Wm^{-2} with generally less than a 0.1% variation. There are some significant short term fluctuations due to decreases associated with the development of sunspots.

The standard solar spectrum in terms of the spectral irradiance is shown in the top solid curve of Figure 6. Also shown in this diagram is the spectral solar irradiance reaching the sea level in a clear atmosphere. The shaded areas represent the amount of absorption by various gases, primarily H_2O, CO_2, O_3, and O_2. Absorption and scattering of solar radiation in clear atmospheres will be discussed later. If one matches the solar spectral irradiance curve with theoretical black body values, we find that a temperature of about 6000 K fits the observed curve closely in the visible and infrared wavelengths. Most of the electromagnetic energy reaching the earth originates from the sun's surface - the photosphere. Of the electromagnetic energy emitted from the sun, approximately 50% lies in wavelengths longer than the visible region, about 40% in the visible region (0.4-0.7 μm), and about 10% in wavelengths shorter than the visible.

COMPOSITION OF THE EARTH'S ATMOSPHERE

To describe the interaction of the earth's atmosphere with solar radiation, the atmosphere's composition must be undertstood. The atmosphere is composed of a group of nearly permanent gases and a group of gases with variable concentration. In addition, the atmosphere also contains various solid and liquid particles such as aerosols, water drops, and ice crystals, which are highly variable in space and time.

Table 3 lists the chemical formula and volume ratio for the concentrations of the permanent and variable gases in the earth's atmosphere. It is apparent from this table that nitrogen, oxygen, and argon account for more than 99.99% of the permanent gases. These gases have virtually constant volume ratios up to an altitude of about 60 km in the atmosphere. It should be noted that although carbon dioxide is listed here as a permanent constituent, its concentration varies as a result of the combustion of fossil fuels, absorption and release by the ocean, and photosynthesis. Water vapour concentration varies greatly both in space and time depending upon the atmospheric condition. Its variation is extremely important in the radiative absorption and emission processes. Ozone concentration also changes with respect to time and space, and it occurs principally in altitudes from about 15 to about 30 km, where it is both produced and destroyed by photochemical reactions. Most of the ultraviolet radiation is absorbed by ozone, preventing this harmful radiation from reaching the earth's surface.

ATMOSPHERIC ABSORPTION AND EMISSION OF SOLAR RADIATION

The absorption and emission of solar radiation in the atmosphere is accomplished by molecular storing of the electromagnetic radiation energy. Molecules can store energy in various ways. Any moving particle has kinetic energy as a result of its motion in space. This is known as translational energy. The averaged translational kinetic energy of a single molecule in the X, Y and Z directions is found to be equal to KT/2, where K is the Boltzmann constant and T is the absolute temperature. The molecule which is composed of atoms can rotate, or revolve, about an axis through its center of gravity and, therefore, has rotational energy. The atoms of the molecule are bounded by certain forces in which the individual atoms can vibrate about their equilibrium positions relative to one another. The molecule therefore will have vibrational energy. These three molecular energy types are based on a rather mechanical model of the molecule that ignores the detailed structure of the molecule in terms of nuclei and electrons. It is possible, however, for the energy of a molecule to change due to a change in the energy state of the electrons of which it is composed. Thus, the molecule has electronic energy. The last three energy types are quantized and take discrete values only. As we have pointed out absorption and emission of radiation takes place when the atoms or molecules undergo transitions from one energy state to another. In general, these transitions are governed by selection rules. Atoms can exhibit line spectra associated with electronic energy. Molecules, however, can have two additional types of energy which lead to complex band systems.

Solar radiation is mainly absorbed in the atmosphere by O_2, O_3, N_2, CO_2, H_2O, O, and N, although NO, N_2O, CO, and CH_4, which occur in very small quantities, also exhibit absorption spectra. Absorption spectra due to electronic transitions of molecular and atomic oxygen and nitrogen, and ozone occur chiefly in the ultraviolet (UV) region, while those due to the

vibrational and rotational transitions of triatomic molecules such as H_2O, O_3, and CO_2 lie in the infrared region. There is very little absorption in the visible region of the solar spectrum.

ATMOSPHERIC ABSORPTION AND EMISSION OF THERMAL RADIATION

Just as the sun emits electromagnetic radiation covering all frequencies, so does the earth. However, the global mean temperature of the earth-atmosphere system is only about 250°K. This temperature is obviously much lower than that of the sun's photosphere. As a consequence, we find from Planck's law and Wien's displacement law discussed earlier that the intensity of the Planck function is less and the wavelength for the intensity peak of the earth's radiation field is longer. We call the energy emitted from the earth-atmosphere system thermal infrared (or terrestrial) radiation. We plot the spectral distribution of radiance emitted by a black body source at various temperatures in the terrestrial range in terms of wavenumber. In Figure 7 the radiance emitted by the earth atmosphere system transmitted to space is shown. The earth radiance to space measured by the Infrared Interferometer Spectrometer Instrument (IRIS) on board Nimbus IV is also shown. The envelope of the emission spectrum is very close to the spectrum emitted from a black body with a temperature of about 300 K, which is about the temperature of the surface. Clearly, certain portions of the infrared radiation are trapped by various gases in the atmosphere.

Among these gases, carbon dioxide, water vapor, and ozone are the most important absorbers. Some minor constituents, such as carbon monoxide, nitrous oxide, methane, and nitric oxide, which are not shown are relatively insignificant absorbers insofar as the heat budget of the earth-atmosphere is concerned. Carbon dioxide absorbs infrared radiation significantly in the 15 μm band from about 600 to 800 cm^{-1}. This spectral region also corresponds to the maximum intensity of the Planck function in the wave number domain. Water vapour absorbs thermal infrared in the 6.3 μm band from about 1200 to 2000 cm^{-1} and in the rotational band (< 500 cm^{-1}). Except for ozone, which has an absorption band in the 9.6 μm region, the atmosphere is relatively transparent from 800 to 1200 cm^{-1}. This region is referred to as the atmospheric window. In addition to the 15 μm band, carbon dioxide also has an absorption band in the shorter wavelength of the 4.3 μm region. The distribution of carbon dioxide is fairly uniform over the global space, although there has been observational evidence indicating a continuous global increase over the past century owing to the increase of the combustion of the fossil fuels. This leads to the question of the earth's climate and possible climatic changes due to the increasing carbon dioxide concentration. Unlike carbon dioxide, however, water vapour and ozone are highly variable both with respect to time and the geographical location. These variations are vital to the radiation budget of the earth-atmosphere system and to long-term climatic changes.

In a clear atmosphere without clouds and aerosols, a large portion (about 50%) of solar energy transmits through the atmosphere and is absorbed by the earth's surface. Energy emitted from the earth, on the contrary, is absorbed largely by carbon dioxide, water vapour, and ozone in the atmosphere as evident in Figure 7b. Trapping of thermal infrared radiation by atmospheric gases is typical of the atmosphere and is therefore called the atmospheric effect.

Solar radiation is also called short-wave radiation because solar energy is concentrated in shorter wavelengths with its peak at about 0.5 μm. Thermal infrared radiation from the earth's atmosphere is referred to as long-wave radiation because its maximum energy is in the longer wavelength at about 10 μm. The solar and infrared spectra are separated into two spectral ranges above and below about 4 μm, and the overlap between them is relatively insignificant. This distinction makes it possible to treat the two types of radiative transfer and source functions separately and thereby simplify the complexity of the transfer problem.

Table 2

Reflectance (in percent) of various surfaces in the spectral range of solar radiation[a]

Bare soil	10–25
Sand, desert	25–40
Grass	15–25
Forest	10–20
Snow (clean, dry)	75–95
Snow (wet and or dirty)	25–75
Sea surface (sun >25° above horizon)	<10
Sea surface (low sun angle)	10–70

Table 3

The Composition of the Atmosphere[a]

Permanent constituents		Variable constituents	
Constituent	% by volume	Constituent	% by volume
Nitrogen (N_2)	78.084	Water vapor (H_2O)	0–0.04
Oxygen (O_2)	20.948	Ozone (O_3)	$0–12 \times 10^{-4}$
Argon (Ar)	0.934	Sulfur dioxide (SO_2)[b]	0.001×10^{-4}
Carbon dioxide (CO_2)	0.033	Nitrogen dioxide (NO_2)[b]	0.001×10^{-4}
Neon (Ne)	18.18×10^{-4}	Ammonia (NH_3)[b]	0.004×10^{-4}
Helium (He)	5.24×10^{-4}	Nitric oxide (NO)[b]	0.0005×10^{-4}
Krypton (Kr)	1.14×10^{-4}	Hydrogen sulfide (H_2S)[b]	0.00005×10^{-4}
Xenon (Xe)	0.089×10^{-4}	Nitric acid vapor (HNO_3)	Trace
Hydrogen (H_2)	0.5×10^{-4}		
Methane (CH_4)	1.5×10^{-4}		
Nitrous oxide (N_2O)[b]	0.27×10^{-4}		
Carbon monoxide (CO)[b]	0.19×10^{-4}		

[a] After the U.S. Standard Atmosphere, 1976.
[b] Concentration near the earth's surface.

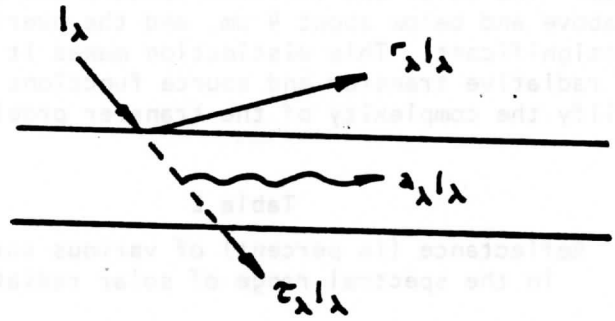

FIGURE 5: A schematic representation of reflectance, absorptance, and transmittance for a slab of material.

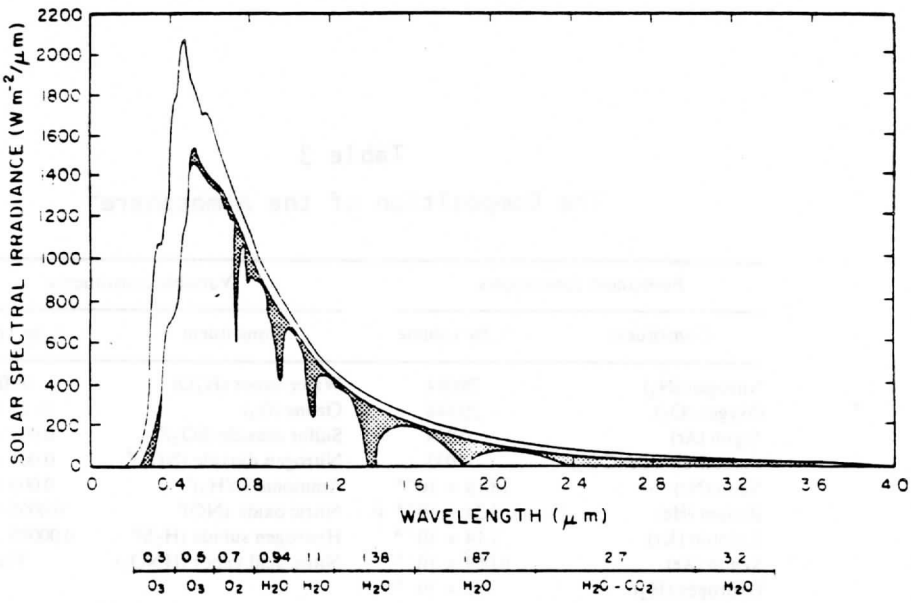

FIGURE 6: Spectral irradiance distribution curves related to the sun; (1) the observed solar irradiance at the top of the atmosphere (after Thekaekara, 1976), and (2) solar irradiance observed at sea level. The shaded areas represent absorption due to various gases in a clear atmosphere.

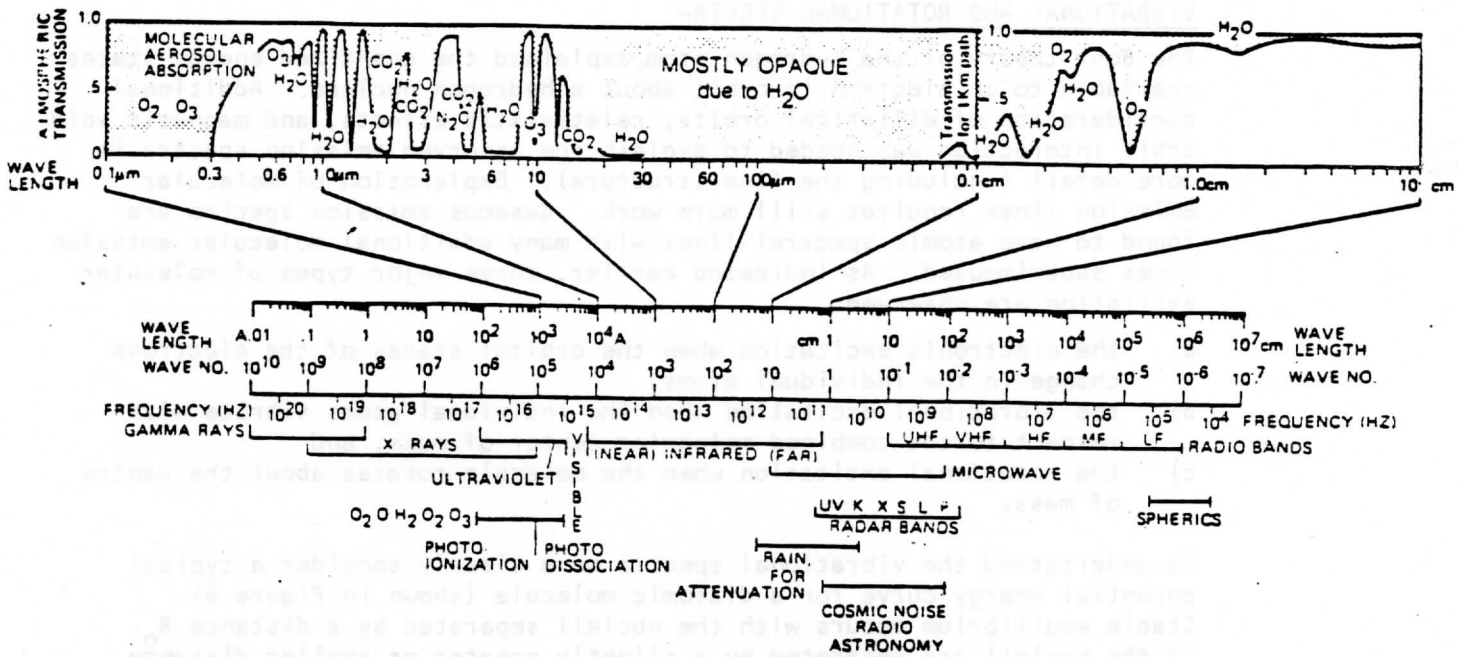

FIGURE 7a: Atmospheric Transmission Characteristics showing the Major Absorption Bands.

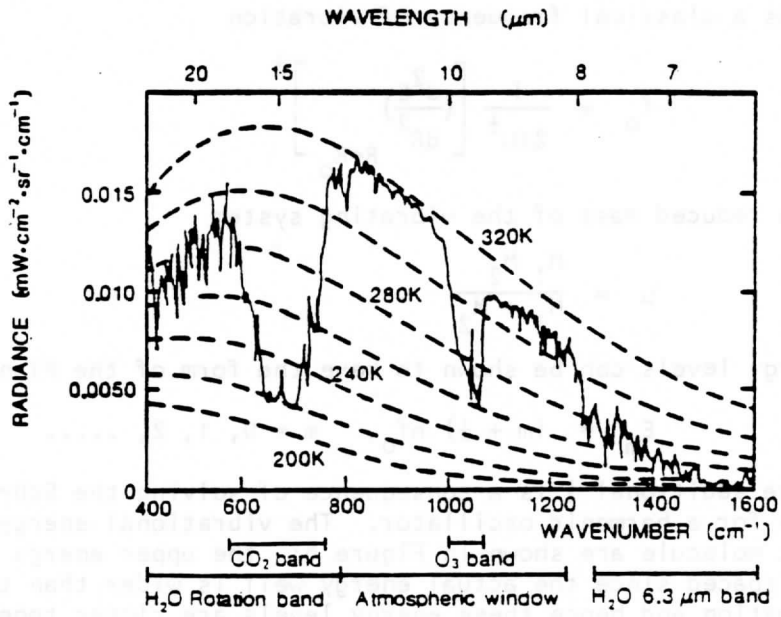

FIGURE 7b: Infrared portion of the Earth Atmosphere emitted radiation showing the Planck emission and the line spectra.

LECTURE 4

VIBRATIONAL AND ROTATIONAL SPECTRA

The Bohr theory of the hydrogen atom explained the quantized energy states available to an electron in orbit about a hydrogen nucleus. Additional consideration of elliptical orbits, relativistic effects, and magnetic spin orbit interaction was needed to explain the observed emission spectra in more detail (including the fine structure). Explanation of molecular emission lines requires still more work. Gaseous emission spectra are found to have atomic spectral lines with many additional molecular emission lines superimposed. As indicated earlier, three major types of molecular excitation are observed:

a) the electronic excitation when the orbital states of the electrons change in the individual atoms,
b) the vibrational excitation when the individual atoms vibrate with respect to the combined molecular center of mass, and
c) the rotational excitation when the molecule rotates about the centre of mass.

To undertstand the vibrational spectra more clearly consider a typical potential energy curve for a diatomic molecule (shown in Figure 8). Stable equilibrium occurs with the nucleii separated by a distance R_o. If the nucleii are separated by a slightly greater or smaller distance R the energy is raised and a spring like restoring force is effected. This restoring force can be represented by

$$F = -\left(\frac{d^2E}{dR^2}\right)_{R=R_o} (R - R_o)$$

which has a classical frequency of vibration

$$f_o = \frac{1}{2\pi\mu^{\frac{1}{2}}}\left[\left(\frac{d^2E}{dR^2}\right)_{R=R_o}\right]^{\frac{1}{2}}$$

with the reduced mass of the vibrating system

$$\mu = \frac{M_1 M_2}{M_1 + M_2} .$$

The energy levels can be shown to have the form of the Planck postulate

$$E_m = (m + \tfrac{1}{2})\, hf_o, \quad m = 0, 1, 2, \ldots..$$

where the additional $\frac{1}{2}$ is a consequence of solving the Schrodinger wave equation for a harmonic oscillator. The vibrational energy levels of a diatomic molecule are shown in Figure 8; the upper energy levels are not equally spaced since the actual energy well is wider than the parabolic approximation and hence these energy levels are closer together than the lower levels.

The rotational spectra appears as fine structure of the combined electronic

and vibrational lines. The kinetic energy of rotation of the nucleii about their common center of mass is readily solved with the Schrodinger equation and the following energy levels emerge :

$$E_J = \frac{h^2}{8\pi^2 \mu R_o^2} J(J+1) .$$

These rotational energies are very small, and therefore lines of the pure rotation spectrum are in the far infrared or microwave regions of the spectrum.

The total energy of a molecule is given by

$$E = E_{electronic} + E_{vibration} + E_{rotation} .$$

The typical separation between the lowest state and the first excited state is about 2 to 10 eV for electronic energies, about .2 to 2eV for vibration energies and about 10^{-5} to 10^{-3} eV for rotation energies. Note that 1 eV = 1.6×10^{-19}J which corresponds to emission at a wavelength of 1.24 μm. Figure 9 illustrates this schematically.

Each transition involving a change in electron energy produces a whole series of emission or absorption lines, since many combinations of changes in vibration and rotation energy are possible. If such a system of lines is observed under low resolution conditions, it appears to be a band with practically a continuous distribution of frequencies. With higher resolution the individual lines can be resolved and the energy differences measured. In this way the energies of the vibrational states and of the rotational states can be measured. It is apparent that in the higher vibration states the average internuclear distance R is larger because of the asymmetry of the binding energy curve. This fact produces a higher moment of inertia μR^2 when the vibrational quantum number is large and a correspondingly smaller separation in the rotational energy levels. Thus precision measurement of the rotational levels as a function of vibrational quantum number permits the study of the asymmetry of the binding energy curve; it is this asymmetry that is responsible for the thermal expansion of molecules.

ATMOSPHERIC ABSORPTION BANDS IN THE INFRARED SPECTRUM

Inspection of high-resolution spectroscopic data reveals that there are thousands of absorption lines within each absorption band. The fine structure of molecular absorption bands for the 320-380 cm^{-1} is due to water vapour, and for the 680-740 cm^{-1} region it is due to carbon dioxide. The optically active gases of the atmosphere, carbon dioxide, water vapour, and ozone are all triatomic molecules. Figure 10 shows the absorption spectra for H_2O and CO_2. Spectroscopic evidence indicates that the three atoms of CO_2 form a symmetrical straight-line array having the carbon atom in the middle flanked by oxygen atoms in either side. Because of linear symmetry it cannot have a static electric dipole moment. Figure 11 shows the three normal modes of vibration of such a configuration. The symmetrical motion v_1 should not give rise to an electric dipole moment and therefore should not be optically active. The v_1 vibration mode has been identified in the Raman spectrum near 7.5 μm. In the v_2 vibration mode, the dipole moment is perpendicular to the axis of the molecule. The 15 μm band represents this particular vibration. The band is referred to as a fundamental because it is caused by a transition from the ground state to the first excited vibrational state. Another fundamental corresponding to the v_3 vibration mode is the 4.3 μm band, which appears at the short-wave edge of the blackbody curve of atmospheric temperatures.

The water molecule forms an isosceles triangle which is obtuse. Figure 11b shows the three normal modes of vibration for such a structure. The 6.3 μm band has been identified as the v_2 fundamental. The two fundamentals, v_1 and v_3, are found close together in a band near 2.7 μm i.e. on the short-wave side of the infrared spectral region.

The band covering the region from 800 to 400 cm^{-1} shown in Figure 7b represents the purely rotational spectrum of water vapour. The water molecule forms an asymmetrical top with respect to rotation, and the line structure of the spectrum does not have the simplicity of a symmetrical rotator such as found in the CO_2 molecule. Close inspection shows that the absorption lines have no clear-cut regularity. The fine structure of the 6.3 μm band is essentially similar to that of the pure rotational band.

In the region between the two water vapour bands, i.e., between about 8 and 12 μm, the so-called atmospheric window, absorption is continuous and is primarily due to water vapour species. Absorption by carbon dioxide is typically a small part of the total in this region. The overlap of water vapour with ozone in this region is insignificant in the computations of cooling rates since water vapour is important mainly in the lower atmosphere, while cooling due to ozone takes place primarily in the stratosphere and higher.

The ozone molecule is of the triatomic nonlinear type (Figure 11b) with a relatively strong rotation spectrum. The three fundamental vibrational bands v_1, v_2, and v_3 occur at wavelengths of 9.066, 14.27, and 9.597 μm, respectively. The very strong v_3 and moderately strong v_1 fundamentals combine to make the well-known 9.6 m band of ozone. The v_2 fundamental is well masked by the 15 μm band of CO_2. The strong band of about 4.7 μm produced by the overtone and combination frequencies of O_3 vibrations is in a weak portion of the Planckian energy distribution for the atmosphere. Note that the absorption bands of O_3 in the UV part of the solar spectrum are due to electronic transitions in the ozone molecule.

BEERS LAW AND SCHWARZCHILDS EQUATION

In the absence of scattering, the absorption of parallel beam radiation as it passes downward through a horizontal layer of gas of infinitesimal thickness dz is proportional to the number of molecules per unit area that are absorbing radiation along the path. This relationship can be expressed in the form

$$da_\lambda \equiv -\frac{dI_\lambda}{I_\lambda} = -k_\lambda \rho \sec\phi \, dz$$

where ρ is the density of the gas and ϕ is the zenith angle. Here absorbed monochromatic radiance is expressed as an incremental amount of depletion of the incident beam. dI_λ and dz are both negative quantities, so da_λ is positive. The product $\rho \sec\phi \, dz$ is the mass within the volume swept out by a unit cross-sectional area of the incident beam as it passes through the layer, as pictured in Figure 12. The absorption coefficient k_λ is a measure of the fraction of the gas molecules per unit wavelength interval that are absorbing radiation at the wavelength in question. k_λ is a function of composition, temperature, and pressure of the gas within the layer. It has units of square meters per kilogram, which makes the product $k_\lambda \rho \, dz$ dimensionless. Integrating from z up to the top of the atmosphere yields

$$\ln I_{\lambda\infty} - \ln I_\lambda = \sec\phi \int_z^\infty k_\lambda \rho \, dz.$$

Taking the antilog of both sides and assuming K_λ is independent of height,

$$I_\lambda = I_{\lambda\infty} \exp(-K_\lambda u)$$

where

$$u = \sec\phi \int_z^\infty \rho dz .$$

This relation, often referred to as Beer's Law, states that radiance decreases monotonically with increasing path length through the layer. The quantity u is called the path length. $K_\lambda u$ is a measure of the cumulative depletion that the beam of radiation has experienced as a result of its passage through the layer and is often called the optical depth σ_λ. The transmittance of the layer of gas lying above the level z is given by

$$\tau_\lambda \equiv I_\lambda / I_{\lambda\infty} = e^{-k_\lambda u} .$$

and it follows that, in the absence of scattering, the absorptance

$$a_\lambda = 1 - \tau_\lambda = 1 - e^{-k_\lambda u} .$$

approaches unity exponentially with increasing optical depth. At wavelengths close to the center of absorption lines, k_λ is large so that a very short (density weighted) path length is sufficient to absorb virtually all the incident radiation. At wavelengths away from absorption lines, a path length many orders of magnitude longer may be required to produce any noticeable absorption.

Indirect calculation of the spectrum of solar radiation incident on the top of the atmosphere, on the basis of ground-based measurements, provides an interesting example of the application of Beer's law. Such calculations were made quite successfully many years before direct measurements of undepleted solar radiation were available from satellites. Writing

$$\ln I_\lambda = \ln I_{\lambda\infty} - \sec\phi \int_z^\infty k_\lambda \rho \, dz$$

Over the course of a single day E is measured at frequent intervals at a ground station. During this period the numerical value of the integral in the above expression changes very little in comparison to the large changes in solar zenith angle. Thus, to a good approximation, the above expression assumes the form

$$\ln I_\lambda = A - BZ$$

where $Z = \sec\phi$ and A and B are constants; that is to say, when the individual data points for I_λ are plotted on a logarithmic scale as a function of $\sec\phi$, they tend to fall along a straight line. Since the path length is directly proportional to Z, it is possible to deduce the monochromatic radiance upon the top of the atmosphere simply by extending the straight line that makes the best fit to the data points back to Z = 0 (that is, zero path length through the atmosphere).

At the wavelengths of solar radiation, atmospheric emission is negligible, and only absorption needs to be considered. However, at the wavelengths of terrestrial radiation, absorption and emission are equally important and must be considered simultaneously. The absorption of terrestrial radiation along an upward path through the atmosphere is described with the sign reversed by the relation

$$-dL_\lambda^{abs} = L_\lambda k_\lambda \rho \sec \phi \, dz ,$$

The emission of radiation from a gas can be treated in much the same manner as the absorption. Making use of Kirchoff's law it is possible to write an analogous expression for the emission,

$$dL_\lambda^{em} = B_\lambda \, d\varepsilon_\lambda = B_\lambda \, da_\lambda = B_\lambda \, k_\lambda \rho \sec \phi \, dz$$

where B_λ is the black body monochromatic radiance specified by Planck's law. Now we subtract the absorption from the emission to obtain the net contribution of the layer to the monochromatic radiance of the radiation passing upward through it:

$$dL_\lambda = - k_\lambda (L_\lambda - B_\lambda) \rho \sec \phi \, dz$$

This expression, known as Schwarzchild's equation, is the basis for computations of the transfer of infrared radiation. For an isothermal gas, with constant k, this may be integrated to obtain

$$(L_\lambda - B_\lambda) = (L_{\lambda o} - B_\lambda) \exp (- k_\lambda u)$$

where $L_{\lambda o}$ is the radiance incident on the layer from below. This expression shows that L_λ should exponentially approach B_λ as the optical thickness of the layer increases. For a layer of infinite optical thickness the emission from the top is B_λ regardless of the value of $L_{\lambda o}$; that is to say, such a layer behaves as a black body.

It is often useful to transform the height variable z to pressure p through the hydrostatic equation and the definition of mixing ratio $q = \rho/\rho_a$ where ρ and ρ_a are the density of gas and air respectively,

$$g \rho \, dz = - q \, dp .$$

Thus the optical depth becomes

$$u(p) = \sec \phi \int_o^p q \, g^{-1} \, dp$$

and the monochromatic transmittance (the probability that a photon of wavelength λ leaving pressure level p will reach the top of the atmosphere) is given by

$$\tau_\lambda (p) = \exp \left[- \sec \phi \int_o^p k_\lambda \, g^{-1} \, q \, dp \right] .$$

ATMOSPHERIC SCATTERING

Scattering is a physical process by which a particle in the path of an electromagnetic wave continuously abstracts energy from the incident wave and reradiates that energy in all directions. Therefore, the particle may be thought of as a point source of the scattered energy. In the atmosphere, the particles responsible for scattering cover the sizes from gas molecules ($\sim 10^{-8}$ cm) to large raindrops and hail particles ($\sim$1 cm). The relative intensity of the scattering pattern depends strongly on the ratio of particle size to wavelength of the incident wave. If scattering is isotropic, the scattering pattern is symmetric about the direction of the incident wave. A small anisotropic particle tends to scatter light equally into the forward and rear directions. When the particle becomes larger, the scattered energy is increasingly concentrated in the forward directions with greater complexities. Distribution of the scattered energy involving spherical and certain symmetrical particles may be quantitatively determined by means of

the electromagnetic wave theory. When particles are much smaller than the incident wavelength, the scattering is called Rayleigh scattering. For particles whose sizes are comparable to or larger than the wavelength, the scattering is customarily referred to as Mie scattering.

Rayleigh scattering indicates that the intensity scattered by air molecules in a specific direction is inversely proportional to the fourth power of the wavelength. A large portion of solar energy lies between the blue to red portion of the visible spectrum. Blue light ($\lambda \simeq 0.425$ μm) has a shorter wavelength than red light ($\lambda \simeq 0.650$ μm). Consequently, blue light scatters about 5.5 more than red light. It is apparent that the λ^{-4} law causes more of the blue light to be scattered than the red, the green, and the yellow, and so the sky, when viewed away from the sun's disk, appears blue. Moreover, since the molecular density decreases drastically with height, it is anticipated that the sky should gradually darken to become completely black in outer space in directions away from the sun. And the sun itself should appear whiter and brighter with increasing height. As the sun approaches the horizon (at sunset or sunrise), sunlight travels through more air molecules, and therefore more and more blue light and light with shorter wavelengths are scattered out of the beam of light, and the luminous sun shows a deeper red colour than at the zenith.

Larger particles in the atmosphere such as aerosols, cloud droplets, and ice crystals also scatter sunlight and produce many fascinating optical phenomena. However, their single scattering properties are less wavelength-selective and depend largely upon the particle size. As a result of this, clouds in the atmosphere generally appear white instead of blue. In a cloudy atmosphere, the sky appears blue diluted with white scattered light, resulting in a less pure blue sky than would have been expected from pure Rayleigh scattering. Scattering by a spherical particle of arbitrary size has been treated exactly by Mie in 1908 by means of solving the electromagnetic wave equation derived from the fundamental Maxwell equations.

It is possible to formulate an expression analogous to absorption for ds_λ, the fraction of parallel beam radiation that is scattered when passing downward through a layer of infinitessimal thickness: namely,

$$ds_\lambda \equiv dI_\lambda / I_\lambda = K A \sec \phi \, dz$$

where K is a dimensionless coefficient, and A is the cross-sectional area that the particles in a unit volume present to the beam of incident radiation. If all the particles which the beam encounters in its passage through the differential layer were projected onto a plane perpendicular to the incident beam, the product A sec ϕ dz would represent the fractional area occupied by the particles. Thus, K plays the role of a scattering area coefficient which measures the ratio of the effective scattering cross section of the particles to their geometric cross section. In the idealized case of scattering by spherical particles of uniform radius r, the scattering area coefficient K can be prescribed on the basis of theory. It is convenient to express K as a function of a dimensionless size parameter $\alpha = 2\pi r/\lambda$, which is a measure of the size of the particles in comparison to the wavelength of the incident radiation. Figure 13a shows a plot of α as a function of r and λ. The scattering area coefficient K depends not only upon the size parameter but also upon the index of refraction of the particles responsible for the scattering. Figure 13b shows K as a function of α for two widely differing refractive indices. When $\alpha << 1$ we have Rayleigh scattering ($K \backsim \alpha^4$), and between .1 and 50 we are in the Mie regime. For $\alpha > 50$ the

angular distribution of scattered radiation can be described by the principles of geometric optics. The scattering of visible radiation by cloud droplets, raindrops, and ice particles falls within this regime and produces a number of distinctive optical phenomena such as rainbows, halos, and so forth.

It should be noted that the scattering of terrestrial radiation in the atmosphere is of secondary importance compared to absorption and emission of terrestrial radiation.

THE MEAN GLOBAL ENERGY BALANCE

Figure 14 summarizes the annual mean global energy balance for the earth atmosphere system and indicates some of the atmospheric processes that come into play. Of the 100 units of incident solar radiation, 19 are absorbed during passage through the atmosphere: 16 in cloud-free air and 3 in clouds. A total of 30 units are reflected back to space: 20 from clouds, 6 from cloud-free air, and 4 from the earth's surface. The remaining 51 units are absorbed at the earth's surface. The earth disposes of this energy by a combination of infrared radiation and sensible and latent heat flux. The net infrared emission, which represents the upward emission from the earth's surface, minus the downward emission from the atmosphere, amounts to 21 units, 15 of which are absorbed in passing through the atmosphere and 6 of which reach space. The remaining 30 units are transferred from the earth's surface to the atmosphere by a combination of latent and sensible heat flux.

From the viewpoint of the atmosphere alone, there is a net loss of 49 units of infrared radiation (70 units emitted to space from the top of the atmosphere minus 21 units of net upward flux from the earth's surface) which exceeds, by 30 units, the energy gained as a result of the absorption of solar radiation. This deficit is balanced by an influx of 90 units of latent and sensible heat from the earth's surface. Thus, in the global average, the atmosphere experiences a net radiative cooling which is balanced by the latent heat of condensation that is released in regions of precipitation, and by the conduction of sensible heat from the underlying surface. Were it not for the fluxes of latent and sensible heat, the earth's surface would have to be considerably hotter (on the order of 340°K as compared with the observed value of 288°K) in order to emit enough infrared radiation to satisfy the balance requirements for thermal equilibrium.

THE FIRST SATELLITE EXPERIMENT TO MEASURE THE NET RADIATION

The radiation budget of net radiation, N, of the entire earth-atmosphere system is the difference between the absorbed solar radiation and the outgoing longwave radiation;

$$N = (1 - A)\frac{S}{4} - R_{LW}$$

where A is the fraction of incoming solar energy reflected back to space (the planetary albedo), S is the incoming solar irradiance and R_{LW} is the outgoing longwave irradiance. The radiation budget equation can be written for a specific location of the earth at a given instant of time by replacing the planetary mean incoming solar radiation term (S/4) with the term S cos ϕ, where ϕ is the solar zenith angle at the location and time of interest. In this case A is no longer the planetary albedo but instead the bi-directional reflectance of the earth-atmosphere for that specific location and time.

The first meteorological satellite experiment flew prior to TIROS-I on the Explorer VII satellite in 1959. The experiment was devised by Suomi and Parent to provide this most basic meteorological measurement, the balance between the radiation input to the atmosphere from the sun and the radiation exiting from the atmosphere as a result of reflection and emission processes. The spatial distribution of the radiation imbalances between incoming and outgoing radiation (the net radiation) is the primary driving force of atmospheric circulation. The solar input had already been measured from ground based and balloon borne platforms. Suomi's experiment was the first to measure the energy loss to space.

Suomi's radiometer consisted of two heat sensing detectors, one painted black to absorb radiation at all wavelengths and the other painted white to reflect the shortwave sun's energy and thereby absorb only earth emitted radiation. Thus, Suomi was able to differentiate between the energy leaving the earth's atmosphere due to reflected sunlight (provided by the difference between the radiation sensed by the black and white sensors) and that emitted by the earth and atmosphere (the radiation measured by the white sensor).

In a short time after exposure to various radiative components involving the direct solar flux, solar flux reflected by the earth and atmosphere (short-wave), and thermal infrared flux emitted by the earth and atmosphere (long-wave), each sensor achieves radiative equilibrium. It is assumed that the absorptivity of the black sensor a_b is the same for short-wave and long-wave radiation. However, the absorptivity of the white sensor for short-wave and long-wave radiation are given by a_w^s and a_w^l, respectively. Let the temperatures measured by the black sensors and white sensors be T_b and T_w, respectively. On the basis of the Stefan-Boltsmann and Kirchhoff laws, radiative equilibrium equations for both sensors may be expressed by

$$4\pi r^2 \, a_b \, \sigma T_b^4 = \pi r^2 \, a_b \, (F_0 + F_S + F_{IR}) \, ,$$

and

$$4\pi r^2 \, a_w^l \, \sigma T_w^4 = \pi r^2 \left[a_w^s \, (F_0 + F_S) + a_w^l \, F_{IR} \right]$$

These two equations show that the emitted energy per unit time is equal to the absorbed energy per unit time, where $4\pi r^2$ and πr^2 represent the emission and absorption areas, respectively, for the two sperheical sensors each with radius r. The flux densities of the reflected short-wave, long-wave radiation, and direct solar are denoted by F_S, F_{IR}, and F_0 respectively.

Upon solving the sum of the short-wave flux densities and the long-wave flux density, we obtain

$$F_0 + F_S = \left[4\sigma \, a_w^l / (a_w^l - a_w^s) \right] (T_b^4 - T_w^4) \, ,$$

and

$$F_{IR} = \left[4\sigma / (a_w^l - a_w^s) \right] (a_w^l \, T_b^4 - a_w^s \, T_w^4) \, .$$

The direct solar flux density F_0 can be evaluated from the solar constant, which is specified prior to the experiment.

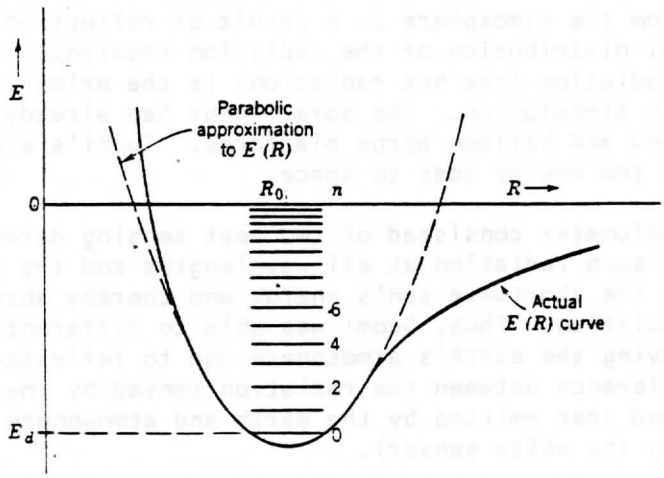

FIGURE 8: Vibrational energy levels of a diatomic molecule.

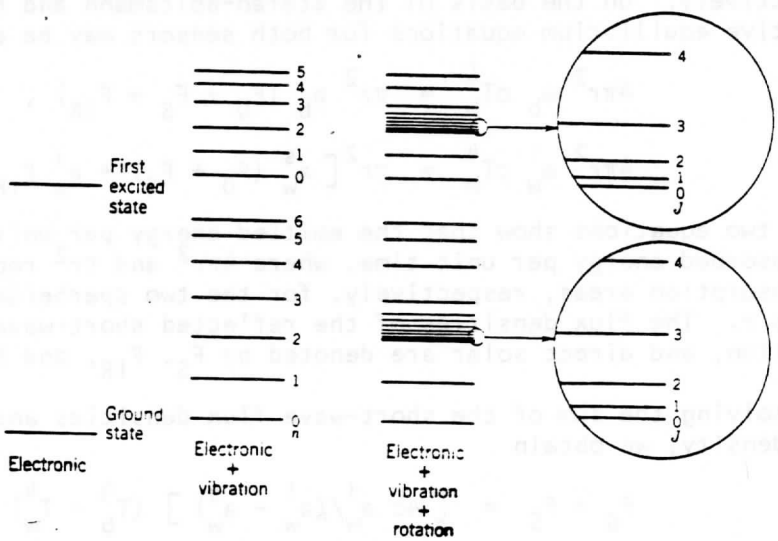

FIGURE 9: The energy levels of a diatomic molecule are sketched in the column at the right. Every level of electronic + vibration energy has the rotation fine structure, but this structure is illustrated only for the n = 2 states.

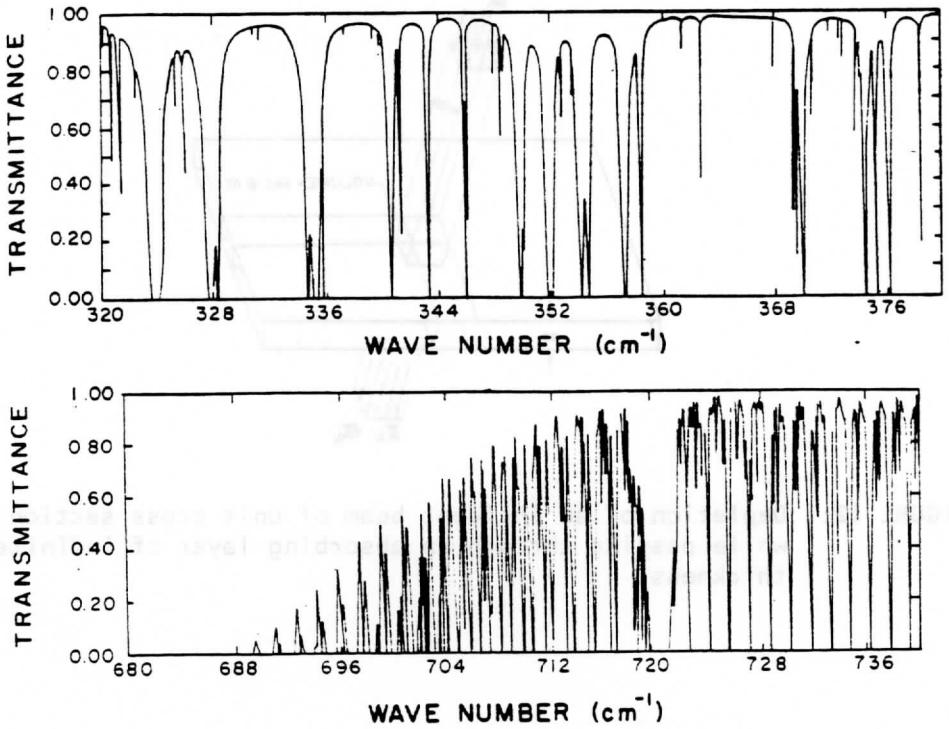

FIGURE 10: Absorption spectrum of the water vapour rotational band and 15 μm carbon dioxide band at high resolution.

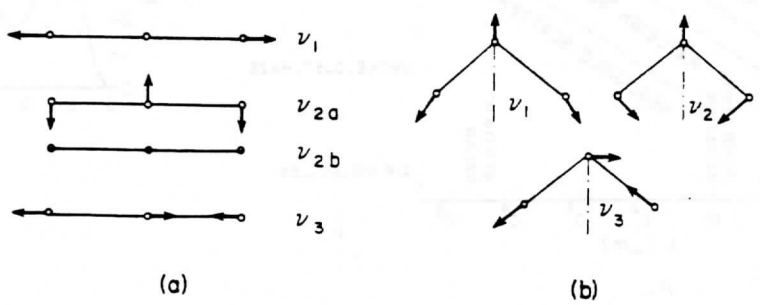

FIGURE 11: Normal modes of a linear (a) and triangle (b) molecules.

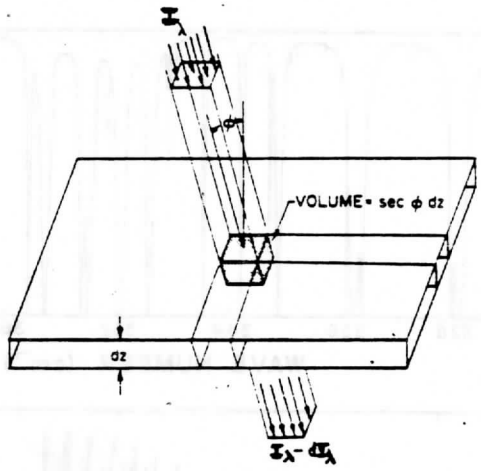

FIGURE 12: Depletion of an incident beam of unit cross section while passing through an absorbing layer of infinitesimal thickness.

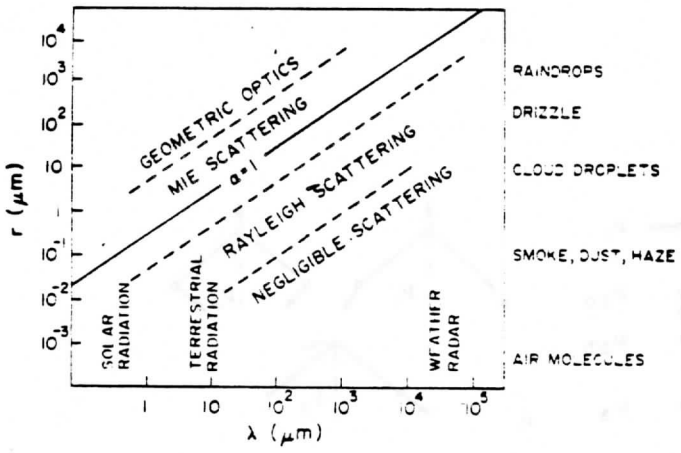

A.

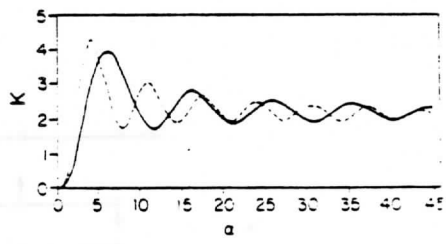

B.

FIGURE 13: a) Size parameter α as a function of incident radiation and particle radius.

b) Scattering area coefficient K as a function of size parameter for refractiveindices of 1.330 (solid curve) and 14.86 (dashed curve).

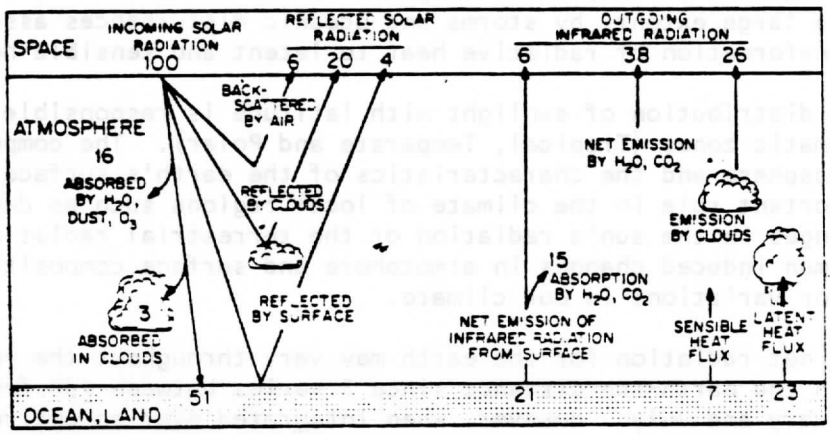

FIGURE 14: The annual mean global energy balance for the earth-atmosphere system. (Numbers are given as percentages of the globally averaged solar irradiance incidence upon the top of the atmosphere.)

LECTURE 5

THE RADIATION BUDGET

The circulation of the earth's atmosphere and oceans can be envisioned to be powered by a heat engine. The shortwave radiation from the sun provides the fuel supply while the infrared radiation heat loss to space from the earth's surface and atmosphere is the exhaust. The engine is throttled, to a large extent, by storms and oceanic disturbances associated with the transformation of radiative heat to latent and sensible heat.

The distribution of sunlight with latitude is responsible for our major climatic zones (Tropical, Temperate and Polar). The composition of the atmosphere and the characteristics of the earth's surface also play an important role in the climate of local regions such as deserts. Small changes in the sun's radiation or the terrestrial radiation due to natural or man induced changes in atmosphere and surface composition might lead to major variations in our climate.

The net radiation for the earth may vary throughout the year in accordance with the earth-sun distance since S varies between $\pm 3\%$ from its mean between January and July. However, when integrated over an entire year, the net radiation must be near zero, otherwise long-term climatic changes would occur. On the planetary and regional scales, clouds play the major role in upsetting the normal state of radiation balance. The importance of clouds in the radiation balance is demonstrated in Figure 15. It shows the relation between the longwave radiation to space as a function of cloud amount and height for a standard atmospheric temperature and moisture condition. Also shown is the absorbed solar radiation as a function of cloud amount. The longwave radiation to space decreases with increasing cloud cover and cloud height because cloud temperatures are considerably lower than the earth's surface and they decrease with cloud elevation. However, clouds are also good reflectors of solar radiation and consequently the global albedo increases and the absorbed solar energy decreases with increasing cloud cover since clouds generally have higher albedoes than the earth's surface.

Figure 16a displays the globally averaged monthly mean values of various radiation budget parameters from July 1975 through December 1976. The annual cycles seem to repeat, as the values observed during July 1976 through December 1976 are nearly the same as those observed one year earlier. The albedo and longwave radiation cycles are nearly 180^{o} (six months) out of phase, possibly the result of two phenomena. The variation of the longwave radiation with time is the first consideration. In the Northern Hemisphere the heating and cooling rates correspond to that expected for land surfaces, so outgoing longwave radiation reaches a maximum in July and a minimum in December. In the Southern Hemisphere it is dominated by sea surfaces, so only a weak cycle is observed because the seasonal variation of sea-surface temperature is negligible. Therefore, the variation of the globally averaged longwave radiation with time is dominated by that in the Noerthern Hemisphere. During the months when the longwave radiation is at a minimum, snow and ice cover and thus albedo in the Noerthern Hemisphere are close to maximum. When the longwave radiation is at a maximum, the snow and ice cover are greatly reduced. A second consideration of equal importance is the annual cycle of cloudiness. There tends to be more cloudiness in the Northern Hemisphere winter than in the Southern Hemisphere winter. This tends to increase the albedo and decrease the longwave radiation. The opposite effect occurs around June when the cloudiness is least. It is uncertain at this time which of the two effects discussed above is the dominant cause

of the variations of the longwave radiation and albedo.

As shown in Figure 16b, the variation with time in the absorbed solar radiation (incoming minus reflected solar radiation) appears to be principally dependent upon the variation of the incoming solar radiation. The annual variation of the incoming solar radiation about its mean value is $\pm$ 11.4 w m^{-2}, while the variation of the reflected energy about its mean value is only about $\pm$ 7.6 w m^{-2}, both nearly in phase with each other. If the earth were in a perfectly circular orbit around the sun so that there were no variations in the incoming radiation due to variations in the earth-sun distance, then the variation in absorbed solar radiation would be dominated by variation in the reflected evergy. This would cause the phase of the absorbed solar radiation to be shifted about 180° from that observed. Minima and maxima, respectively, of the reflected radiation. Since the net radiation is the difference of the absorbed solar radiation and the outgoing longwave radiation, which are nearly 180° out of phase with each other, the variation in the net radiation has an amplitude exceeding that of the absorbed and outgoing components and nearly the same phase as the absorbed solar radiation.

DERIVATION OF THE RADIATIVE TRANSFER EQUATION (RTE)

Radiative transfer serves as a mechanism for exchanging energy between the atmosphere and the underlying surface and between different layers of the atmosphere. Infrared radiation emitted by the atmosphere and intercepted by satellites is the basis for remote sensing of the atmospheric temperature structure.

The radiance leaving the earth-atmosphere system which can be sensed by a satellite borne radiometer is the sum of radiation emissions from the surface and each atmospheric level that are transmitted to the top of the atmosphere. Considering the earth's surface to be a blackbody emitter (emissivity equal to unity), the upwelling radiance intensity, I_λ, for a cloudless atmosphere is given by the expression

$$I_\lambda = B_\lambda(T(p_s))\tau_\lambda(p_s) + \sum_p \varepsilon_\lambda(\Delta p)B_\lambda(T(p))\tau_\lambda(p)$$

where the first term is the surface contribution and the second term is the atmospheric contribution to the radiance to space. Using Kirchoff's law, the emissivity of an infinitessimal layer of the atmosphere at pressure p is equal to the absorptance (one minus the transmittance of the layer). Consequently,

$$\varepsilon_\lambda(\Delta p)\tau_\lambda(p) = [1 - \tau_\lambda(\Delta p)]\tau_\lambda(p)$$

Since the transmittance is an exponential function of depth of the absorbing constituent,

$$\tau_\lambda(\Delta p)\tau_\lambda(p) = \exp\left[-\sec\phi \int_p^{p+\Delta p} K_\lambda\, q\, g^{-1}\, dp\right]$$

$$\exp\left[-\sec\phi \int_o^{p} K_\lambda\, q\, g^{-1}\, dp\right] = \tau_\lambda(p + \Delta p) .$$

Therefore

$$\varepsilon_\lambda(\Delta p)\tau_\lambda(p) = \tau_\lambda(p) - \tau_\lambda(p + \Delta p) = -\Delta\tau_\lambda(p) .$$

So we can write

$$I_\lambda = B_\lambda (T(p_s))\tau_\lambda(p_s) - \sum_p B_\lambda (T(p))\Delta\tau_\lambda(p) .$$

which when written in integral form reads

$$I_\lambda = B_\lambda(T(p_s))\tau_\lambda(p_s) + \int_{p_s}^{o} B_\lambda(T(p)) \frac{d\tau_\lambda(p)}{dp} dp .$$

The first term is the spectral radiance emitted by the surface and attenuated by the atmosphere, often called the Boundary Term and the second term is the spectral radiance emitted to space by the atmosphere.

Another approach to the derivation of the RTE is to start from Schwarzchilds equation written in pressure coordinates

$$dI_\lambda = (I_\lambda - B_\lambda) K_\lambda g^{-1} q \sec\phi \, dp .$$

This is a first order linear differential equation, and to solve it we multiply by the integrating factor

$$\tau_\lambda = \exp\left[- \sec\phi \int_o^p g^{-1} q K_\lambda \, dp\right]$$

which has the differential

$$d\tau_\lambda = - \tau_\lambda \sec\phi \, g^{-1} q K_\lambda \, dp .$$

Thus

$$\tau_\lambda dI_\lambda = - (I_\lambda - B_\lambda) d\tau_\lambda$$

or

$$d(\tau_\lambda I_\lambda) = B_\lambda d\tau .$$

Integrating from p_s to o, we have

$$I_\lambda(o)\tau_\lambda(o) - I_\lambda(p_s)\tau_\lambda(p_s) = \int_{p_s}^{o} B_\lambda(T(p)) \frac{d\tau_\lambda(p)}{dp} dp .$$

The spectral radiance detected by the satellite is given by $I_\lambda(o)$, $\tau_\lambda(o)$ is 1 by definition, and the surface of the earth is treated as a black body so $I_\lambda(p_s)$ is given by $B_\lambda(T(p_s))$. Therefore

$$I_\lambda = B_\lambda(T(p_s))\tau_\lambda(p_s) + \int_{p_s}^{o} B_\lambda(T(p)) \frac{d\tau_\lambda(p)}{dp} dp$$

as before.

Writing this in terms of height

$$I_\lambda = B_\lambda(T(o))\tau_\lambda(o) + \int_o^\infty B_\lambda(T(z)) \frac{d\tau_\lambda}{dz} dz .$$

$d\tau_\lambda/dz$ is often called the weighting function which, when multiplied by the Planck function, yields the upwelling radiance contribution from a given altitude z. An alternate form of the weighting function is $d\tau_\lambda/d\ln_p$.

To investigate the RTE further consider the atmospheric contribution to the radiance to space of an infinitessimal layer of the atmosphere at height z,

$$dI_\lambda(z) = B_\lambda(T(z))d\tau_\lambda(z) .$$

Assume a well mixed isothermal atmosphere where the density must drop off exponentially with height

$$\rho = \rho_o \exp(-\gamma z) ,$$

and assume K_λ is independent of height, so that the optical depth can be written for normal incidence

$$\sigma_\lambda = \int_z^\infty K_\lambda \rho dz = \gamma^{-1} K_\lambda \rho_o \exp(-\gamma z)$$

and the derivative with respect to height

$$\frac{d\sigma_\lambda}{dz} = -K_\lambda \rho_o \exp(-\gamma z) = -\gamma \sigma_\lambda .$$

Therefore we may obtain an expression for the detected radiance per unit thickness of the layer as a function of optical depth

$$\frac{dI_\lambda(z)}{dz} = B_\lambda(T_{const}) \frac{d\tau_\lambda(z)}{dz} = B_\lambda(T_{const})\, \gamma \sigma_\lambda \exp(-\sigma_\lambda) .$$

The level which is emitting the most detected radiance is given by

$$\frac{d}{dz}\left(\frac{dI_\lambda(z)}{dz}\right) = 0$$

or where $\sigma_\lambda = 1$. Most of the monochromatic radiance impinging upon the satellite is emitted by layers near the level of unit optical depth. Much of the radiation emanating from deeper layers is absorbed on its way up through the atmosphere, while far above the level of unit optical depth there is not enough mass to emit very much radiation. The assumption of an isothermal atmosphere with a constant absorption coefficient was helpful in simplifying the mathematics in the above derivation. However it turns out that for realistic vertical profiles of T and K_λ the above result is still at least qualitatively valid j that is, most of the satellite detected radiation emanates from that portion of the atmosphere for which the optical depth is of order unity.

The fundamental principle of atmospheric sounding from orbiting meteorological satellites utilizing the thermal infrared emission is based on the solution of the radiative transfer equation. In this equation, the upwelling radiance arises from the product of the Planck function, the spectral transmittance, and the weighting function. The Planck function consists of temperature information, while the transmittance is associated with the absorption coefficient and density profile of the relevant absorbing gases. Obviously, the observed radiance contains the temperature and gaseous profiles of the atmosphere, and therefore, the information content of the observed radiance from satellites must be physically related to the temperature field and absorbing gaseous concentration.

The mixing ratio of CO_2 is fairly uniform as a function of time and space in the atmosphere. Moreover, the detailed absorption characteristics of CO_2 in the infrared region are well understood and its absorption parameters, i.e. half width, line strength, and line position, are known rather accurately. Consequently, the spectral transmittance and weighting functions for a given level may be calculated once the spectral interval and the instrumental response function have been given. To see the atmospheric temperature profile information we rewrite the RTE so that

$$I_\lambda - B_\lambda(T(p_s))\tau_\lambda(p_s) = \int_{p_s}^{o} B_\lambda(T(p)) \frac{d\tau_\lambda(p)}{dp} dp .$$

It is apparent that measurements of the upwelling radiance in the CO_2 absorption band contain the information of temperature values in the interval $(p_s,0)$, once the surface temperature has been determined. However, the information content of the temperature is under the integral operator which leads to an ill-conditioned mathematical problem. We will discuss in detail this problem and a number of methods for the recovery of the temperature profile from a set of radiance observations in the CO_2 band.

Finally, to understand the information content of gaseous profile from the solution of the radiative transfer equation, we perform integration by parts on the integral term to yield

$$I_\lambda - B_\lambda(T(p_s)) = \int_{p_s}^{o} \tau_\lambda(p) \frac{dB_\lambda(p)}{dp} dp .$$

Now, if measurements are made in the H_2O or O_3 spectral regions, and if temperature values are known, the transmittance profile may be inferred just as the temperature profile may be recovered when the spectral transmittance is given relating the gaseous concentration profile to the spectral transmittance, we see that the density values are hidden in the exponent of an integral which is further complicated by the spectral integration over the response function. Because of these complications, retrieval of the gaseous density profile is made very difficult, and no clear-cut mathematical analyses may be followed in the inverse of the density values. Therefore, we focus our attention on the temperature inversion problem.

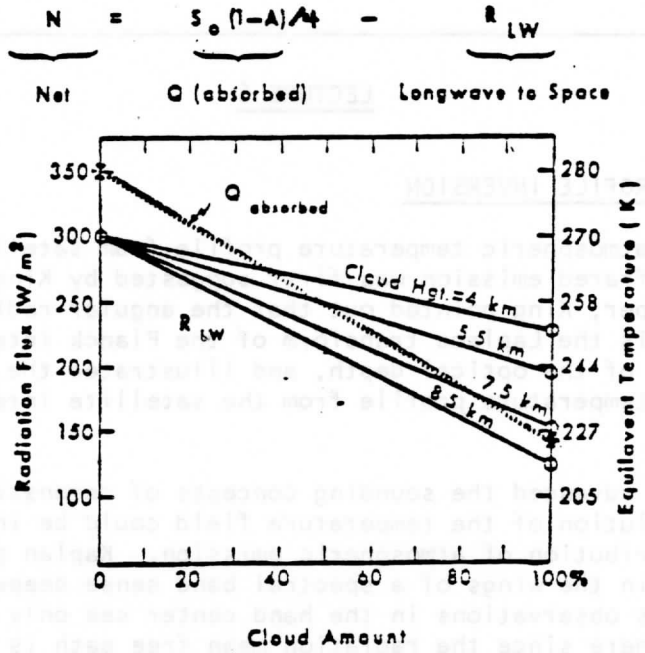

FIGURE 15: Longwave Radiation in Space and Absorbed Solar Radiation as a Function of Cloud Amount.

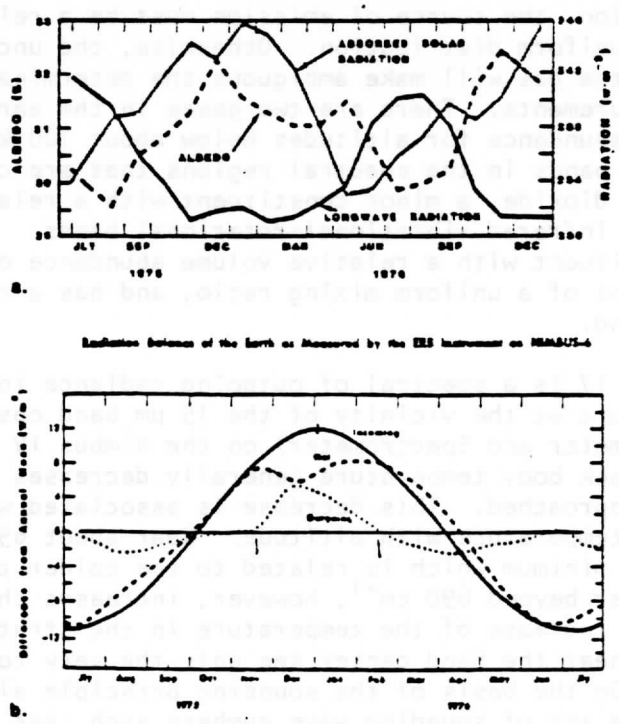

FIGURE 16 a: Globally averaged monthly mean values of radiation budget parameters;

b: variation in time of net, incoming, and outgoing Solar radiation.

LECTURE 6

TEMPERATURE PROFILE INVERSION

Inference of atmospheric temperature profile from satellite observations of thermal infrared emission was first suggested by King (1956). In his pioneering paper, King pointed out that the angular radiance (intensity) distribution is the Laplace transform of the Planck intensity distribution as a function of the optical depth, and illustrated the feasibility of deriving the temperature profile from the satellite intensity scan measurements.

Kaplan (1959) advanced the sounding concepts of demonstrating that vertical resolution of the temperature field could be inferred from the spectral distribution of atmospheric emission. Kaplan pointed out that observations in the wings of a spectral band sense deeper into the atmosphere, whereas observations in the hand center see only the very top layer of the atmosphere since the radiation mean free path is small. Thus, by properly selecting a set of different sounding wave numbers, the observed radiances could be used to make an interpretation leading to the vertical temperature distribution in the atmosphere.

Wark (1961) proposed a satellite vertical sounding program to measure atmospheric temperature profiles. Polar orbiting sounders were first flown in 1969 and a geostationary sounder was launched in 1980.

In order for atmospheric temperatures to be determined by measurements of thermal emission, the source of emission must be a relatively abundant gas of known and uniform distribution. Otherwise, the uncertainty in the abundance of the gas will make ambiguous the determination of temperature from the measurements. There are two gases in the earth-atmosphere which have uniform abundance for altitudes below about 100 km, and which also show emission bands in the spectral regions that are convenient for measurement. Carbon dioxide, a minor constituent with a relative volume abundance of 0.003, has infrared vibrational-rotational bands. In addition, oxygen, a major constituent with a relative volume abundance of 0.21, also satisfies the requirement of a uniform mixing ratio, and has a microwave spin-rotational band.

Shown in Fig. 17 is a spectral of outgoing radiance in terms of the black body temperature at the vicinity of the 15 μm band observed by IRIS (Infrared Interferometer and Spectrometer) on the Nimbus IV satellite. The equivalent black body temperature generally decreases as the center of the band is approached. This decrease is associated with the decrease of tropospheric temperature with altitude. Near about 690 cm^{-1}, the temperature shows a minimum which is related to the colder tropopause. Decreasing the wave number beyond 690 cm^{-1}, however, increases the temperature. This is due to the increase of the temperature in the stratosphere, since the observations near the band center see only the very top layers of the atmosphere. On the basis of the sounding principle already discussed, we could select a set of sounding wave numbers such that a temperature profile in the troposphere and lower stratosphere could be largely covered. The arrows in Fig. 17 indicate an example of such a selection.

There is no unique solution for the detailed vertical profile of temperature or an absorbing constituent because; (i) the contribution to the earth-atmosphere outgoing radiances arise from relatively deep layers of the atmosphere, (ii) the contribution to the radiances observed within various spectral channels overlap considerably such that the observations contained in a set of spectral radiances are not vertically independent of each other, and (iii) measurements of outgoing radiance possess errors. As a consequence, there are a large number of analytical approaches to the profile retrieval problem. The approaches differ both in the numerical procedure for solving the set of spectrally independent radiative transfer equations (e.g., matrix inversion versus interation) and in the type of ancillary data used to constrain the solution to insure that a meteorologically meaningful result is achieved (e.g., the use of atmospheric covariance statistics as opposed to the use of an apriori estimate of the profile structure). There are some excellent papers in the literature which review the retrieval theory which has been developed over the past few decades (Fleming and Smith, 1971; Fritz et al., 1972; Rodgers, 1976; and Twomey, 1977). The next pages will present the mathematical basis for some of the procedures which have been utilized in the operational retrieval of atmospheric profiles from satellite measurements and will include some example problems that are solved by using these procedures.

TRANSMITTANCE DETERMINATIONS

Before proceeding to the retrieval problem, a few comments about the determination of transmittance are important.

So far we have expressed the upwelling radiance at a monochromatic wavelength. However for a practical instrument whose spectral channels have a finite spectral bandwidth, all quantities given in RTE are integrated over length being weighted by the spectral response of the instrument. The measured radiance over an interval (λ_1,λ_2) is given by

$$I_{\bar{\lambda}} = \int_{\lambda_1}^{\lambda_2} \phi(\bar{\lambda},\lambda)\ I_\lambda\ d\lambda \Big/ \int_{\lambda_1}^{\lambda_2} \phi(\bar{\lambda},\lambda)\ d\lambda$$

where ϕ and $\bar{\lambda}$ denote the instrumental response (or slit) function and mean wavelength of the band width, respectively. However, since B varies slowly with λ while τ varies rapidly and without correlation to B within the narrow spectral channels of the sounding spectrometer, it is sufficient to perform the spectral integrations of B and τ independently and treat the results as if they are monochromatic values for the effective wavelength $\bar{\lambda}$.

For simplicity of discussion, we shall let the response function $\phi(\bar{\lambda},\lambda) = 1$ so that the spectral transmittance may be expressed by

$$\tau_{\bar{\lambda}}(p) = \int_{\Delta\lambda} \frac{d\lambda}{\Delta\lambda} \exp\left[-\frac{q}{g} \int_o^p k_\lambda(p')\ dp'\right]$$

Here we note that the mixing ratio q is a constant, and $\Delta\lambda = \lambda_1 - \lambda_2$. In the lower atmosphere, collision broadening dominates the absorption process and the shape of the absorption lines is governed by the Lorentz profile

$$k_\lambda = \frac{S}{\pi} \frac{\alpha}{(\lambda - \lambda_o)^2 + \alpha^2}\ .$$

The half width α is primarily proportional to the pressure (and to a lesser degree the temperature), while the line strength S also depends on the temperature. Hence, the spectral transmittance may be explicitly written as

$$\tau_{\bar{\lambda}}(p) = \int_{\Delta\lambda} \frac{d\lambda}{\Delta\lambda} \exp\left[-\frac{g}{g}\int_o^p \frac{S(p')}{\pi} \frac{\alpha(p')dp'}{(\lambda - \lambda_o)^2 + \alpha^2(p')}\right].$$

The temperature dependence of the absorption coefficient introduces some difficulties in the sounding of the temperature profile. Nevertheless, the dependence of the transmittance on the temperature may be taken into account in the temperature inversion process by building a set of transmittances for a number of standard atmospheric profiles from which a search could be made to give the best transmittances for a given temperature profile.

The computation of transmittances through an inhomogeneous atmosphere is rather involved, especially when the demands on accuracy are high in infrared sounding applications. Thus, accurate transmittance profiles are normally derived by means of line-by-line calculations, which involve the direct integration of monochromatic transmittance over the wave number spectral inteval, weighted by an appropriate response function if so desired. Since the monochromatic transmittance is a rapidly varying function of wave number, numerical quadrature used for the integration must be carefully devised, and the required computational effort is generally enormous.

All of the earlier satellite experiments for the sounding of atmospheric temperatures of meteorological purposes have utilized the 15 μm CO_2 band. The 15 μm CO_2 band consists of a number of individual bands which contribute significantly to the absorption. The most important of these is the v_2 fundamental vibrational rotational band. In addition, there are several weak bands caused by the vibrational transitions between excited states, and by molecules containing less abundant isotopes.

For temperature profile retrievals the transmittance is assumed to be determined.

FREDHOLM FORM OF RTE AND THE DIRECT LINEAR INVERSION METHOD

Upon knowing the radiances from a set of wavelengths and the associated transmittances, the fundamental problem encountered is, how to solve for the function $B_\lambda(T(p))$. We note that because there is a multiplicity of wavelength at which the observations are made, the Planck function differs from the equation to another depending on the wavelength. Thus, it becomes vitally important for the direct inversion problem to eliminate the wavelength dependence in this function. In the vicinity of the 15 μm CO_2 band, it is sufficient to approximate the Planck function in a linear form as

$$B_\lambda(T(p)) = c_\lambda B_{\lambda_o}(T(p)) + d_\lambda$$

where λ_o denotes a fixed reference wavelength and c_λ and d_λ are empirically derived constants. Assuming without loss of generality that $\tau_\lambda(p_s) = 0$, we obtain

$$r_\lambda = \int_{p_s}^{o} t(p)W_\lambda(p)\, dp,$$

where we have let

$$r_\lambda = \frac{I_\lambda - d_\lambda}{c_\lambda},$$

$$t(p) = B_{\lambda_o}(T(p)),$$

$$W_\lambda(p) = \frac{\partial \tau_\lambda(p)}{\partial p}.$$

This is the well-known Fredholm equation of the first kind. $W_\lambda(p)$, the weighting function, is the kernel, and $t(p)$, the temperature profile, is the function to be recovered from a set of radiances r_λ, $\lambda = 1,2,\ldots,M$, where M is the total number of wavelengths chosen.

The solution of this equation is clearly an ill-posed problem, since the unknown profile is a continuous function of pressure, and there are only a finite number of observations. It is convenient to express $t(p)$ as a linear function of L variables in the form

$$t(p) = \sum_{j=1}^{L} t_j f_j(p),$$

where t_j are unknown coefficients, and $f_j(p)$ are the known representation functions which could be orthogonal functions, such as polynomials or Fourier series. It follows that

$$r_\lambda = \sum_{j=1}^{L} t_j \int_{p_s}^{o} f_j(p) W_\lambda(p)\, dp, \quad \lambda = 1,2,\ldots,M.$$

Upon defining the known values in the form

$$H_{\lambda j} = \int_{p_s}^{o} f_j(p) W_\lambda(p)\, dp,$$

we obtain

$$r_\lambda = \sum_{j=1}^{L} H_{\lambda j} t_j, \quad \lambda = 1,2,\ldots,M.$$

Generally, in order to find $t_j (j = 1,\ldots,L)$, one needs to have the $r_\lambda (\lambda = 1,\ldots,M)$ and also $M \geq L$. In matrix form, radiances are then related to temperature

$$r = Ht$$

We can write a solution

$$t = H^{-1} r = (H^t H)^{-1} H^t r,$$

where H^t represents the matrix transpose. To find the solution t, one requires the inverse of a symmetric and square matrix.

It has been pointed out by many studies that the solution derived is unstable because the equation is underconstrained. Furthermore, the instability of this solution may also be traced to the following sources of error: (i) the errors arising from the numerical quadrature used for the calculation of $H_{\lambda j}$; (ii) the approximation to the Planck function; and (iii) the numerical round-off errors. In addition, sounding radiometers possess inherent instrumental noise, and thus the observed radiances generate errors prob-

ably in a random fashion. All of these errors make the direct inversion from the solution of transfer equation difficult. We now discuss a number of methods which can be utilized to stabilize the solution, and for certain instances give reasonable results.

ITERATION SOLUTION BY CHAHINE RELAXATION METHOD

The difficulty in reconstructing the temperature profile from the radiance is due to the fact that the Fredholm equation with fixed limits may not always have a solution for an arbitrary function. Since the radiances are obtained from measurements which are only approximate, the reduction of this problem to a linear system is mathematically improper, and a nonlinear approach to the solution of the full radiative transfer equations appears to become necessary.

The basic radiance equation is

$$I_\lambda = B_\lambda(T_s)\tau_\lambda(p_s) + \int_{p_s}^{o} B_\lambda(T(p)) \frac{\partial \tau_\lambda(p)}{\partial \ln p} d \ln p, \quad \lambda = 1,2,\ldots,M,$$

where λ denotes the different spectral channels and the weighting function is expressed in logarithmic scale. Since the weighting function reaches a strong maximum at different pressure levels for different spectral channels, the actual upwelling radiance observed by the satellite, R_λ, can be approximated through the use of the mean value theorem, by

$$R_\lambda = B_\lambda(T_s)\tau_\lambda(p_s) + B_\lambda(T(p_\lambda)) \left[\frac{\partial \tau_\lambda(p)}{\partial \ln p} \right]_{p_\lambda} \Delta_\lambda \ln p ,$$

where p_λ denotes the pressure level at which the maximum weighting function is located, and $\Delta_\lambda \ln p$ is the difference of the pressure at the λth level and is defined as the effective width of the weighting functions. Let the guessed temperature at p_λ level be $T'(p_\lambda)$. Thus, the guessed upwelling radiance I_λ is given by

$$I_\lambda = B_\lambda(T_s)\tau_\lambda(p_s) + B_\lambda(T'(p_\lambda)) \left[\frac{\partial \tau_\lambda(p)}{\partial \ln p} \right]_{p_\lambda} \Delta_\lambda \ln p ,$$

where the transmittance and the surface temperature are assumed to be known.

Upon dividing and noting that the dependence of the Planck function on temperature variations is much stronger than that of the weighting function, we obtain

$$\frac{R_\lambda - B_\lambda(T_s)\tau_\lambda(p_s)}{I_\lambda - B_\lambda(T_s)\tau_\lambda(p_s)} \approx \frac{B_\lambda(T(p_\lambda))}{B_\lambda(T'(p_\lambda))}$$

When the surface contribution to the upwelling radiance is negligible or dominant, the equation may be approximated by

$$\frac{R_\lambda}{I_\lambda} \approx \frac{B\ (T(p_\lambda))}{B_\lambda(T'(p_\lambda))}$$

or in iteration form

$$\frac{R_\lambda}{I_\lambda^{old}} = \frac{B_\lambda(T^{new}(p_\lambda))}{B_\lambda(T^{old}(p_\lambda))} .$$

This is the relaxation equation developed by Chahine (1970).

Since most of the upwelling radiance at the strong absorption bands arises from the upper parts of the region, whereas the radiance from the less attenuating bands comes from progressively lower levels, it is possible to select a set of wave numbers to recover the atmospheric temperature at different pressure levels. The size of a set of sounding wave numbers is defined by the degree of the vertical resolution required and is obviously limited by the capacity of the sounding instrument.

Assuming now that the upwelling radiance is measured at a discrete set of M spectral channels, and that the composition of carbon dioxide and the level of the weighting function peaks p_λ are all known, the following iteration procedures are utilized to recover the temperature profile $T^{(n)}(p_\lambda)$ at level p_λ, where n is the order of iterations:

(a) Make an initial guess for $T^{(n)}(p_\lambda)$, n = 0

(b) Substitute $T^{(n)}(p_\lambda)$ into the RTE and use an accurate quadrature formula to evaluate the expected upwelling radiance $I_\lambda^{(n)}$ for each sounding channel.

(c) Compare the computed radiance values $I_\lambda^{(n)}$ with the measured data R_λ. If the residuals

$$\Delta_\lambda^{(n)} = [R_\lambda - I_\lambda^{(n)}]/R_\lambda$$

are less than a preset small value (say, 10^{-4}) for each sounding channel, then $T^{(n)}(p_\lambda)$ is a solution.

(d) If the residuals are greater than the preset criterion, we apply the relaxation equation M times to generate a new guess for the temperature values

$$T^{(n+1)}(p_\lambda)$$

at the selected λ pressure levels. Note that

$$T^{(n+1)}(p_\lambda) = B^{-1}\left[B(T^{(n)}(p_\lambda)) \frac{R_\lambda}{I_\lambda^{(n)}} \right] .$$

In this calculation, each sounding channel acts at one specific pressure level p_λ to relax

$$T^{(n)}(p_\lambda) \quad \text{to} \quad T^{(n+1)}(p_\lambda) .$$

(e) Carry out the interpolation between the temperature value at each given level p_λ to obtain the desirable profile (it is sufficient to use linear interpolation).

(f) Finally, with this new temperature profile, go back to step (b) and repeat until the residuals are less than the preset criterion.

EXAMPLE PROBLEM USING RELAXATION METHOD

Consider a three channel radiometer with spectral bands centered at 14.8, 14.1, and 13.4 μm. These spectral bands have weighting functions that peak at 50, 400, and 900 mb respectively. The transmittance is summarized in the following table.

Pressure (mb)	Transmittance 676.7	708.7	746.7 (cm^{-1})
60	.86	.96	.98
150	.05	.65	.87
600	.00	.09	.61
1000	.00	.00	.21

The surface temperature is known to be 280°K. The radiometer senses the radiances R_i for each spectral band i to be 45.2, 56.5, and 77.8 $mW/(m^2 \cdot ster \cdot cm^{-1})$ respectively.

(a) Guess $T^{(o)}(50) = T^{(o)}(400) = T^{(o)}(900) = 260^{o}K$.

(b) Compute the radiance values for this guess profile by writing

$$I_i^{(o)} = B_i(1000)\tau_i(1000) + B_i(900)(\tau_i(600) - \tau_i(1000)) + B_i(400)(\tau_i(150) - \tau_i(600)) + B_i(50)(\tau_i(10) - \tau_i(150)),$$

yielding 76.9, 82.3, and 85.2 $mW/(m^2 \cdot ster \cdot cm^{-1})$ respectively.

(c) Convergence has not been reached.

(d) Iterate to a new profile using the relaxation equation

$$T^{(1)}(p_i) = B_i^{-1}\left[B(T^{(o)}(p_i))\frac{R_i}{I_i^{(o)}}\right]$$

yielding 228, 238, and 244°K respectively.

(e) Disregard interpolation of temperature to other pressure levels in this example and go back to (b).

(b') 45.7, 55.3, 71.6 $mW/(m^2 \cdot ster \cdot cm^{-1})$
(c') no convergence
(d') 228, 239, 259°K

(b'') 45.3, 56.4, 74.4 $mW/(m^2 \cdot ster \cdot cm^{-1})$
(c'') no convergence
(d'') 228, 239, 262°K

(b''') 45.2, 56.7, 75.9
(c''') no convergence
(d''') 228, 239, 264°K

(b'''') 45.2, 56.8, 76.7
(c'''') convergence within 1 $mW/(m^2 \cdot ster \cdot cm^{-1})$

Thus the temperature retrieval yields T(50) = 228°K, T(400) = 239°K, and T(900) = 264°K.

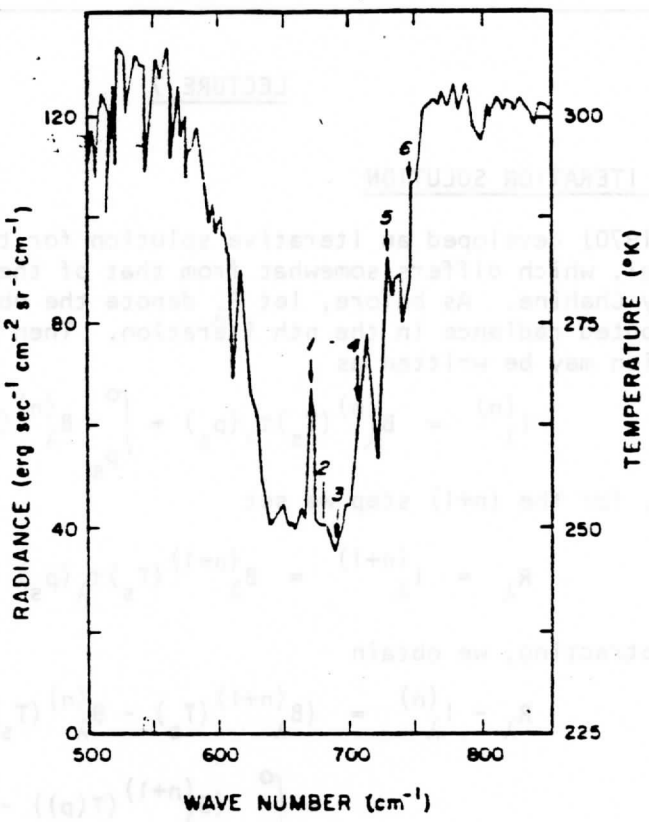

FIGURE 17. Outgoing radiance in terms of black body temperature in the vicinity of 15 μm CO_2 band observed by the IRIS on Nimbus IV. The arrows denote the spectral regions sampled by the VTPR instrument.

LECTURE 7

SMITH'S ITERATION SOLUTION

Smith (1970) developed an iterative solution for the temperature profile retrieval, which differs somewhat from that of the relaxation method introduced by Chahine. As before, let R_λ denote the observed radiance and $I_\lambda^{(n)}$ the computed radiance in the nth iteration. Then the upwelling radiance expression may be written as

$$I_\lambda^{(n)} = B_\lambda^{(n)}(T_s)\tau_\lambda(p_s) + \int_{p_s}^{o} B_\lambda^{(n)}(T(p)) \frac{\partial \tau_\lambda(p)}{\partial \ln p} d \ln p .$$

Further, for the (n+1) step we set

$$R_\lambda = I_\lambda^{(n+1)} = B_\lambda^{(n+1)}(T_s)\tau_\lambda(p_s) + \int_{p_s}^{o} B_\lambda^{(n+1)}(T(p)) \frac{\partial \tau_\lambda(p)}{\partial \ln p} d \ln p$$

Upon subtracting, we obtain

$$R_\lambda - I_\lambda^{(n)} = (B_\lambda^{(n+1)}(T_s) - B_\lambda^{(n)}(T_s))\tau_\lambda(p_s) + \int_{p_s}^{o} \{B_\lambda^{(n+1)}(T(p)) - B_\lambda^{(n)}(T(p))\} \frac{\partial \tau_\lambda(p)}{\partial \ln p} d \ln p$$

An assumption is made at this point that for each sounding wavelength the Planck function difference for the sensed atmospheric layer is independent of the pressure coordinate. Thus,

$$R_\lambda - I_\lambda^{(n)} = B_\lambda^{(n+1)}(T(p)) - B_\lambda^{(n)}(T(p)).$$

That is,

$$B_\lambda^{(n+1)}(T(p)) = B_\lambda^{(n)}(T(p)) + (R_\lambda - I_\lambda^{(n)}) .$$

This is the iteration equation developed by Smith. Moreover, for each wavelength we have

$$T_\lambda^{(n+1)}(p) = B_\lambda^{-1}\left[B_\lambda(T^{(n+1)}(p)) \right] .$$

Since the temperature inversion problem now depends on the sounding wavelength λ the best approximation of the true temperature at any level p would be given by a weighted mean of independent estimates so that

$$T_\lambda^{(n+1)}(p) = \sum_{\lambda=1}^{M} T_\lambda^{(n+1)}(p) W_\lambda(p) / \sum_{\lambda=1}^{M} W_\lambda(p) ,$$

where the proper weights should be approximately

$$W_\lambda(p) = \begin{cases} d\tau_\lambda(p), & p < p_s \\ \tau_\lambda(p), & p = p_s \end{cases} .$$

It should be noted that the numerical technique presented above makes no assumption about the analytical form of the profile imposed by the number of radiance observations available. The following iteration schemes for the temperature retrieval may now be employed:

(a) Make an initial guess for $T^{(n)}(p)$, $n = 0$.

(b) Compute $B_\lambda^{(n)}(T(p))$ and $I_\lambda^{(n)}$.

(c) Compute $B_\lambda^{(n+1)}(T(p))$ and $T_\lambda^{(n+1)}(p)$ for the desired levels.

(d) Make a new estimate of $T^{(n+1)}(p)$ using the proper weights.

(e) Compare the computed radiance values $I_\lambda^{(n)}$ with the measured data R_λ. If the residuals

$$\Delta^{(n)} = |R_\lambda - I_\lambda^{(n)}|/R_\lambda$$

are less than a preset small value, then $T^{(n+1)}(p)$ would be the solution. If not, repeat steps (b)-(d) until convergence is achieved.

EXAMPLE PROBLEM USING SMITH'S ITERATION

Using the data from the three channel radiometer discussed in the previous example involving the Relaxation Method, we proceed as before.

(a) Guess $T^{(o)}(50) = T^{(o)}(400) = T^{(o)}(900) = 260^oK$.

(b) Compute the estimated radiance values as before yielding 76.9, 82.3, 85.2 mW/(m^2.ster.cm^{-1}) for $I_i^{(o)}$.

(c) For each spectral band i, calculate a new profile from

$$T_i^{(1)}(p_j) = B_i^{-1}\{B(T^{(o)}(p_j)) + (R_i - I_i^{(o)})\}$$

where j runs over all desired pressure levels. This yields

233, 233, 233^{o}K for $T_1^{(1)}$,

239, 239, 239^{o}K for $T_2^{(1)}$,

and 254, 254, 254^{o}K for $T_3^{(1)}$.

(d) The next iteration profile will be given by the weighted mean

$$T^{(1)}(p_j) = \sum_{i=1}^{3} T_i^{(1)}(p_j)\Delta\tau_i(p_j) / \sum_{i=1}^{3} \Delta\tau_i(p_j)$$

which yields 237, 243, 251^{o}K.

(e) No convergence yet, using the arbitrary criterion that $|R_i - I_i| < 1$ mW/(m^2.ster.cm^{-1}).

(b') 52.9, 60.8, 72.5 mW/(m^2.ster.cm^{-1}) are $I_i^{(1)}$.

(c') $T_1^{(2)}$ is 229, 236, 245^{o}K

$T_2^{(2)}$ is 232, 239, 248^{o}K

$T_3^{(2)}$ is 242, 248, 256^{o}K

(d') $T^{(2)}$ is 231, 241, 254°K

(e') No convergence yet.

(b'') 48.2, 58.4, 72.8 mW/(m^2.ster.cm^{-1}) are $I_i^{(2)}$

(c'') $T_1^{(3)}$ is 228, 239, 252°K

$T_2^{(3)}$ is 229, 240, 253°K

$T_3^{(3)}$ is 236, 246, 258°K

(d'') $T^{(3)}$ is 229, 241, 257°K

(e'') No convergence yet.

(b''') 46.5, 58.2, 74.1 mW/(m^2.ster.cm^{-1}) are $I_i^{(3)}$

(c''') $T_1^{(4)}$ is 228, 240, 256°K

$T_2^{(4)}$ is 227, 240, 256°K

$T_o^{(4)}$ is 233, 245, 260°K

(d''') $T^{(4)}$ is 228, 241, 259°K

(e''') Convergence in next iteration.

(b'''') 45.7, 58.1, 75.1 mW/(m^2.ster.cm^{-1}) are $I_i^{(4)}$ which are within 1 mW/(cm^2.ster.cm^{-1}) of $I_i^{(3)}$.

(c'''') $T_1^{(5)}$ 228, 241, 259°K

$T_2^{(5)}$ 226, 240, 258°K

$T_o^{(5)}$ 231, 244, 261°K

(d'''') $T^{(5)}$ is 228, 241, 261°K

Thus the temperature retrieval yields T(50) = 228°K, T(400) = 241°K, and T(900) = 261°K. This result compares reasonably well with the earlier result obtained by the relaxation method.

COMPARISON OF THE CHAHINE AND SMITH NUMERICAL ITERATION SOLUTIONS

Figure 18 illustrates a retrieval exercise using both Chahine's and Smith's methods. The same transmittances were used and the true temperature profile is shown in the figure. A climatological profile was used as an initial guess, and the surface temperature was fixed at 279.5°K. The observed radiances utilized were obtained by direct computations for six VTPR channels at 669.0, 676.7, 694.7, 708.7, 723.6, and 746.7 cm^{-1} using a forward difference scheme. Numerical procedures already outlined were followed, and a linear interpolation with respect to ln p was used in the relaxation method to get the new profile. With the residual set at 1%, the

relaxation method converged after six iterations, and results are given by the solid line with black dots. Since the top level at which the temperature was calculated was about 20 mb, extrapolation to the level of 1 mb was used. Recovered results using Smith's method are displayed by the dashed line. No interpolation is necessary since this method gives temperature values at desirable levels. It took five iterations to converge the solution to within 1%. Both methods do not adequately recover the temperature at upper levels due to the fact that the highest weighting function peak is at about 30 mb. It should be noted that the retrieval exercise presented here does not account for random errors and therefore, it is a hypothetical one.

The major problems with the Chahine method are:

(a) the profile is not usually well represented by a series of line segments between pressure levels where the weighting functions peak, particularly for a small number of channels (levels), and

(b) the iteration and hence the solution can become unstable since one is attempting to extract M distinct pieces of information from M non-independent observations.

While the Smith method does avoid the problems of the Chahine method (no interpolation is required for a temperature at any pressure level and the solution is stable in the averaging scheme because the random error propatating from R_λ to $T(p)$ is suppressed to the average value of the errors in all channels, which will be near zero), it does have the main disadvantage that the averaging process can prevent obtaining a solution that satisfies the observations to within their measurement error levels. There is no guarantee that the solution converges to one which satisfies the radiances by this criterion.

LINEARIZATION OF RTE

So far we have presented two numerical iteration methods for solving the temperature profile from the RTE. Several other techniques remain to be discussed. Most of these techniques require linearization of the RTE in which the dependence of Planck radiance on temperature is linearized, often with a first order Taylor expansion about a mean condition. Defining the mean temperature profile condition as $\bar{T}(p)$, then

$$B_\lambda(T) = B_\lambda(\bar{T}) + \left.\frac{\partial B_\lambda(T)}{\partial T}\right|_{T=\bar{T}} (T - \bar{T})$$

so the RTE can be written

$$\bar{I}_\lambda + \left.\frac{\partial B_\lambda(T)}{\partial T}\right|_{T=\bar{T}_{b_\lambda}} (T_{b_\lambda} - \bar{T}_{b_\lambda}) = B_\lambda(T_s)\tau_\lambda(p_s) + \int_{p_s}^{o} \{B_\lambda(\bar{T}) + \left.\frac{\partial B_\lambda(T)}{\partial T}\right|_{T=\bar{T}} (T - \bar{T})\} \frac{\partial \tau_\lambda(p)}{\partial \ln p} \, d \ln p$$

where T_{b_λ} represents the brightness temperature for spectral band λ. Reducing to simplest form

$$(\Delta T_{b_\lambda}) = \int_{p_s}^{o} (\Delta T) \left(\frac{\partial B_\lambda(T)}{\partial T} \bigg|_{T=\bar{T}} \Big/ \frac{\partial B_\lambda(T)}{\partial T} \bigg|_{T=\bar{T}_{b_\lambda}} \right) \frac{\partial \tau_\lambda(p)}{\partial \ln p} \, d \ln p$$

where Δ denotes temperature difference from the mean condition. This linear form of the RTE can then be written in numerical quadrature form

$$(\Delta T_b)_\lambda = \sum_{j=1}^{N} W_{\lambda j} \, (\Delta T)_j \qquad \lambda = 1,\ldots,M$$

where W_λ is the obvious weighting factor, M is the number of spectral bands, and N is the number of levels at which a temperature determination is desired.

EXAMPLE PROBLEM SOLVING LINEAR RTE DIRECTLY

The linear form of the RTE can be solved directly (often with rather poor results). For the example problem presented earlier, we have that T_b equals 223, 232, and 258°K for the spectral bands respectively. As before take $\bar{T}(1000) = 280^oK$ and assume a mean temperature profile condition $\bar{T}(900) = \bar{T}(400) = \bar{T}(50) = 260^oK$. Therefore $\bar{T}_b$ equals 250, 258, and 263°K respectively. We set up the matrix solution by writing

$$\Delta T_{b_i} = \Delta T_{900} \left[\frac{\partial B_i}{\partial T} \bigg|_{T_{900}} \Big/ \frac{\partial B_i}{\partial T} \bigg|_{T_{b_i}} \right] (\tau_i(600) - \tau_i(1000))$$

$$+ \Delta T_{400} \left[\frac{\partial B_i}{\partial T} \bigg|_{T_{400}} \Big/ \frac{\partial B_i}{\partial T} \bigg|_{T_{b_i}} \right] (\tau_i(150) - \tau_i(600))$$

$$+ \Delta T_{50} \left[\frac{\partial B_i}{\partial T} \bigg|_{T_{50}} \Big/ \frac{\partial B_i}{\partial T} \bigg|_{T_{b_i}} \right] (\tau_i(10) - \tau_i(150)) \quad ,$$

which gives

$$-27 = \Delta T_{900}(.89/.77)(.00) + \Delta T_{400}(.89/.77)(.05) + \Delta T_{50}(.89/.77)(.81)$$

$$-26 = \Delta T_{900}(.86/.83)(.09) + \Delta T_{400}(.86/.83)(.56) + \Delta T_{50}(.86/.83)(.31)$$

$$-5 = \Delta T_{900}(.81/.85)(.40) + \Delta T_{400}(.81/.85)(.26) + \Delta T_{50}(.81/.85)(.11) \; .$$

Solving we find that $\Delta T_{900} = 15$, $\Delta T_{400} = -33$, and $\Delta T_{50} = -25$ so that the temperature profile solution is $T(900) = 275^oK$, $T(400) = 227^oK$, and $T(50) = 235^oK$.

Obviously this example was ill conditioned since Taylor expansion of differences larger than 10°K is foolhardy. However this does demonstrate how to set up a direct solution, which should be representative of the mean temperature condition used in the expansion is close to the actual temperature profile.

Typically the direct solution is unstable because there are the unknown observation errors and W is nearly singular due to strong overlapping of the weighting functions. Since W is ill-conditioned with respect to matrix

inversion, the elements of the inverse matrix are greatly inflated, which in turn greatly amplifies the experimental error of the observations. This renders the solution virtually useless. The ill-conditioned solution results since one does not have N independent pieces of information about T from M radiation observations. The solution is further complicated because M is usually much smaller than the number of temperature points, N, needed to represent the temperature profile.

SOLUTION BY USE OF BASIS FUNCTIONS

For the remainder of our discussion of the RTE we will assume linear form and also drop the difference rotation, so T represents ΔT. As pointed out earlier it is often advantageous to expand the temperature profile for the N pressure levels

$$T(p_j) = \sum_{K=1}^{L} a_k f_k (p_j) \qquad j = 1,.....,N$$

where L is the number of basis functions (less than M the number of spectral bands) and $f_k (p_j)$ are some type of basis functions (polynomials, weighting functions, or empirical orthogonal functions); then a tractable form of the RTE is possible.

An empirically optional approximation is achieved by defining $f_k (p_j)$ as empirical orthogonal functions (EOF) which are the eigenvectors of a statistical covariance matrix T^tT. When the eigenvector and associated eigenvalues of (T^tT) are determined and the N eigenvalues are ordered from largest to smallest, the associated eigenvectors will be ordered according to the amount of variance they explain in the empirical sample of soundings used to determine T^tT. The EOF's are optimal basis functions in that the first EOF $f_1(p_j)$ is the best single predictor of T(p) that can be found in a mean squared error sense to describe the values used to form T^tT. The second EOF is the best prediction of the variance unexplained by $f_1(p_j)$, and so on. Wark and Fleming (1966) first used the EOF approximation in the linear RTE to obtain

$$T_{b_\lambda} = \sum_{k=1}^{L} a_k \left[\sum_{j=1}^{N} W_{\lambda_j} f_{kj} \right]$$

$$T_{b_\lambda} = \sum_{k=1}^{L} a_k H_{\lambda k}$$

or in matrix notation $T_b = Ha$.

The least square solution for a yields

$$a = (H^tH)^{-1} H^t T_b$$

In practice the empirical function series is truncated either on the basis of the smallness of the eigenvalues (thus the smallness of explained variance) of higher order eigenvectors or on the basis of numerical instabilities which result when L approaches M.

If $L \leq M$ and L is small (e.g., ≤ 5), a stable solution can usually be obtained by the direct inverse

$$a = H^{-1} t_b \quad .$$

The matrix H in this case is much less singular (better conditioned with respect to matrix inversion) than is W. This is because the basis vector f_k is smooth and acts as a constraint on the solution thereby stabilizing it. However, in practice, best results are obtained by choosing an optimum L<M or by conditioning the H matrix prior to its inversion.

LEAST SQUARES REGRESSION

The least squares regression solution was used for the operational production of soundings from the very first sounding spectrometer data by Smith (1970). The form of the direct inverse solution, where T_b are observations which include the measurement error (i.e., $T_b = T_b + \varepsilon$), is found to be

$$T = W^{-1}T_b \quad \text{or} \quad T = T_bA$$

where A is a matrix of solution coefficients. One can define A as that matrix which gives the best least squares solution for T in a statistical ensemble of simultaneously observed radiances and temperature profiles. Extending to an entire sample of K soundings, where K>>M and N, the matrices have dimensions of K x N and K x M, respectively. Therefore

$$T_b{}^tT = T_b{}^tT_bA$$

and

$$A = (T_b{}^tT_b)^{-1}\ T_b{}^tT$$

where the superscript t indicates matrix transposition.

The advantages of the regression method over other methods are :

(a) if one uses real radiance and radiosonde data comparisons to form the statistical sample, one does not require knowledge of the weighting functions or the observation errors,

(b) the instrument need not be calibrated in an absolute sense, and

(c) the regression is numerically stable.

Some shortcomings of the regression method are :

(a) it disregards the physical properties of the RTE in that the solution is linear whereas in fact the exact solution is non-linear because the weighting function W and consequently the s-lution coefficients A are functions of temperature,

(b) the solution uses the same operator matrix for a range of radiances depending upon how the sample is stratified, and thus the solution coefficients are not situation dependent, and

(c) radiosonde data is required, so that the satellite sounding is dependent on more than just surface data.

STATISTICAL REGULARIZATION

To make explicit use of the physics of the RTE in the statistical method, one can express the brightness temperatures for the statistical ensemble of profiles as

$$T_b = TW + E \ ,$$

where E is a matrix of the unknown observational errors. Solving as before yields

$$A = (S^t T^t TW + E^t E)^{-1} W^t T^t T \ ,$$

where covariances between observation error and temperature ($E^t T$) are assumed to be zero since they are uncorrelated. Defining the covariance matrices

$$S_T = \frac{1}{K-1} (T^t T) \quad \text{and} \quad S_E \equiv \frac{1}{K-1} (E^t E)$$

then

$$A = (W^t S_T W + S_E)^{-1} W^t S_T \ .$$

The solution for the temperature profile is

$$T = T_b (W^t S_T W + S_E)^{-1} W^t S_T \ .$$

This solution was developed independently by Strand and Westwater (1968), Rodgers (1968), and Turchin and Nozik (1969).

The objections raised about the regression method do not apply to this statistical regularization solution; namely,

(a) W is included and its temperature dependence can be taken into account through iteration,

(b) the solution coefficients are reestablished for each new temperature profile retrieval, and

(c) there is no need for coincident radiosonde and satellite observations so that one can use a historical sample to define S_T.

The advantages of the regression method are, however, the disadvantages of the statistical regularization method; namely,

(a) the weighting functions must be known with higher precision, and

(b) the instrument must be calibrated accurately in an absolute sense.

As with regression, the statistical regularization solution is stable because S_T and S_E are strongly diagonal matrices which makes the matrix

$$(S^t S_T W + S_E)$$

well conditioned for inversion.

MINIMUM INFORMATION SOLUTION

Twomey (1963) developed a temperature profile solution to the radiances which represents a minimal perturbation of a guess condition, for example, a forecast profile. In this case T represents deviations of the actual profile from the guess and T_b represents the deviation of the observed brightness temperatures from those which would have arisen from the guess profile condition. S_T is then a covariance matrix of the errors in the guess profile, which is unknown. Assume that the errors in the guess are uncorrelated from level to level such that

$$S_T = \sigma_T^2 I$$

where I is the identity matrix and σ_T^2 is the expected variance of the errors in the guess. If one also assumes that the measurement errors are random, then

$$S_E = \sigma_E^2 I \quad .$$

Simplifying the earlier expression yields

$$T = T_b (W^t W + \gamma I)^{-1} W^t$$

where

$$\gamma = \sigma_\varepsilon^2 / \sigma_t^2 \quad (\approx 10^{-3}) \quad .$$

The solution given is the Tikhonov (1963) method of regularization.

The solution is generally called the Minimum Information Solution since it requires only an estimate of the expected error of the guess profile. One complication of this solution is that γ is unknown. However, one can guess at γ (e.g., 10^{-3}) and iterate it until the solution converges,

$$\frac{1}{M} \sum_{i=1}^{M} (T_{bi} - \hat{T}_{bi})^2 \leq \sigma_\varepsilon^2 \quad .$$

The minimum information solution was used for processing sounding data by the SIRS-B and VTPR instruments.

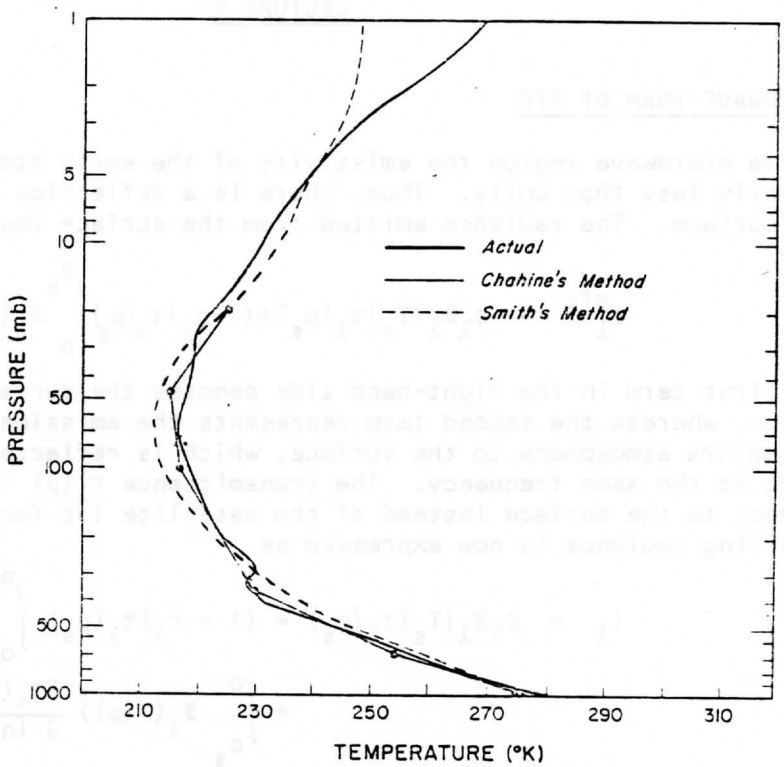

FIGURE 18: Temperature retrieval using Chahines relaxation and Smith's iterative methods for VTPR channels.

LECTURE 8

MICROWAVE FORM OF RTE

In the microwave region the emissivity of the earth atmosphere system is normally less than unity. Thus, there is a reflection contribution from the surface. The radiance emitted from the surface would therefore be given by

$$I_\lambda^{sfc} = \varepsilon_\lambda B_\lambda(T_s)\tau_\lambda(p_s) + (1-\varepsilon_\lambda)\tau_\lambda(p_s)\int_o^{p_s} B_\lambda(T(p)) \frac{\partial \tau'_\lambda(p)}{\partial \ln p} d \ln p$$

The first term in the right-hand side denotes the surface emission contribution, whereas the second term represents the emission contribution from the entire atmosphere to the surface, which is reflected back to the atmosphere at the same frequency. The transmittance $\tau'_\lambda(p)$ is now expressed with respect to the surface instead of the satellite (as for $\tau_\lambda(p)$). Thus the upwelling radiance is now expressed as

$$I_\lambda = \varepsilon_\lambda B_\lambda(T_s)\tau_\lambda(p_s) + (1 - \varepsilon_\lambda)\tau_\lambda(p_s) \int_o^{p_s} B_\lambda(T(p)) \frac{\partial \tau'_\lambda(p)}{\partial \ln p} d \ln p + \int_{p_s}^{o} B_\lambda(T(p)) \frac{\partial \tau_\lambda(p)}{\partial \ln p} d \ln p$$

In the wavelength domain, the Planck function is given by

$$B_\lambda(T) = c_1 / |\lambda^5 (e^{c_2/\lambda T} - 1)| \ .$$

In the microwave region $c_2/\lambda T << 1$, the Planck function may be approximated by

$$B_\lambda(T) \approx \frac{c_1}{c_2} \frac{T}{\lambda^4} \ ;$$

the Planck radiance is linearly proportional to the temperature. Analogous to the above approximation, we may define an equivalent brightness temperature T_b such that

$$I_\lambda = \frac{c_1}{c_2} \frac{T_b}{\lambda^4} \ .$$

Thus the solution of microwave radiative transfer may now be written in terms of temperature

$$T_{b_\lambda} = \varepsilon_\lambda T_s \ \tau_\lambda(p_s) + (1 - \varepsilon_\lambda)\tau_\lambda(p_s) \int_o^{p_s} T(p) \frac{\partial \tau'_\lambda(p)}{\partial \ln p} d \ln p + \int_{p_s}^{o} T(p) \frac{\partial \tau_\lambda(p)}{\partial \ln p} d \ln p \ .$$

The transmittance to the surface can be expressed in terms of transmittance to the top of the atmosphere by remembering

$$\tau'_\lambda(p) = \exp\left[-\frac{1}{g} \int_p^{p_s} k_\lambda(p)\ g(p)\ dp\right]$$

$$= \exp\left[-\int_o^{p_s} + \int_o^{p}\right]$$

$$= \tau_\lambda(p_s)/\tau_\lambda(p)$$

So

$$\frac{\partial \tau'_\lambda(p)}{\partial \ln p} = -\frac{\tau_\lambda(p_s)}{(\tau_\lambda(p))^2}\,\frac{\partial \tau_\lambda(p)}{\partial \ln p}\,.$$

And thus to achieve a form similar to that of the infrared RTE, we write

$$T_{b_\lambda} = \varepsilon_\lambda T_s\, \tau_\lambda(p_s) + \int_{p_s}^{o} T(p)\, F_\lambda(p)\, \frac{\partial \tau_\lambda(p)}{\partial \ln p}\, d \ln p$$

where

$$F_\lambda(p) = \left\{1 + (1 - \varepsilon_\lambda)\left[\frac{\tau_\lambda(p_s)}{\tau_\lambda(p)}\right]^2\right\}.$$

A special problem area in the use of microwave for atmospheric sounding from a satellite platform is surface emissivity. In the microwave spectrum, emissivity values of the earth's surface vary over a considerable range, from about 0.4 to 1.0. The emissivity of the sea surface typically ranges between 0.4 and 0.5, depending upon such variables as salinity, sea ice, surface roughness, and sea foam. In addition, there is a frequency, dependence with higher frequencies displaying higher emissivity values. Over land, the emissivity depends on the moisture content of the soil. Wetting of a soil surface results in a rapid decrease in emissivity. The emissivity of dry soil is on the order of 0.95 to 0.97, while for wet bare soil it is about 0.80 to 0.90, depending on the frequency. The surface emissivity appearing in the first term has a significant effect on the brightness temperature value.

The basic concept of inferrring atmospheric temperatures from satellite observations of thermal microwave emission in the oxygen spectrum was developed by Meeks and Lilley (1963) in whose work the microwave weighting functions were first calculated. The prime advantage of microwave over infrared temperature sounders is that the longer wavelength microwaves are much less influenced by clouds and precipitation. Consequently, microwave wounders can be effectively utilized to infer atmospheric temperatures in all-weather conditions. We will not pursue microwave retrievals in this course, except to say that the techniques are similar to those for infrared retrieval.

RTE IN CLOUDY CONDITIONS

Thus far we have considered the RTE in a clear sky condition. When we introduce clouds into the radiation field of the atmosphere the problem becomes more complex. The following notes indicate some of the fundamental problems concerning clouds.

If we assume that the fractional cloud cover within the field of view of the satellite radiometer is represented by η and the cloud top pressure by p_o, then the spectral radiance measured by the satellite radiometer at the top of the atmosphere is given by

$$I_\lambda = \eta\, I_\lambda^{cd} + (1 - \eta) I_\lambda^{c}$$

where cd denotes cloud and c denotes clear. As before we can write for the clear radiance

$$I_\lambda^{c} = B_\lambda(T_s)\tau_\lambda(p_s) + \int_{p_s}^{o} B_\lambda(T(p))\, d\tau_\lambda \ .$$

The cloud radiance is represented by

$$I_\lambda^{cd} = (1 - \varepsilon_\lambda)B_\lambda(T_s)\tau_\lambda(p_s) + (1 - \varepsilon_\lambda)\int_{p_s}^{p_c} B_\lambda(T(p))\, d\tau_\lambda$$

$$+ \varepsilon_\lambda B_\lambda(T(p_c))\tau_\lambda(p_c) + \int_{p_c}^{o} B_\lambda(T(p))\, d\tau_\lambda$$

where ε_λ represents the emittance of the cloud. The first two terms are contributions from below the cloud, the third term is the cloud contribution, and the fourth term is the contribution from above the cloud. After some rearranging these expressions can be combined to yield

$$I_\lambda - I_\lambda^{c} = \eta(I_\lambda^{cd} - I_\lambda^{c})$$

$$= \eta\varepsilon_\lambda \left| B_\lambda(T(p_c))\tau_\lambda(p_c) - B_\lambda(T_s)\tau_\lambda(p_s) - \int_{p_s}^{p_c} B_\lambda(T(p))\, d\tau_\lambda \right| .$$

A simpler form is available by using integration by parts, so

$$I_\lambda - I_\lambda^{c} = \eta\varepsilon_\lambda \int_{p_s}^{p_c} \tau(p)\, \frac{dB_\lambda}{dp}\, dp \ .$$

The techniques for dealing with clouds generally fall into three different categories;

a) Searching for cloudless fields-of-view,

b) Specifying cloud top pressure and sounding down to cloud level as in the cloudless case, and

c) Employing adjacent fields-of-view to determine the clear sky signal from partly cloudy observations.

The last approach utilizes multiple fields of view in the following way. For a given wavelength λ, the radiance from two spatially independent but geographically close fields of view is written

$$I_{\lambda,1} = \eta_1\, I_{\lambda,1}^{cd} + (1 - \eta_1)\, I_{\lambda,1}^{c} \ ,$$

$$I_{\lambda,2} = \eta_2\, I_{\lambda,2}^{cd} + (1 - \eta_2)\, I_{\lambda,2}^{c} \ .$$

If the clouds are at a uniform altitude, and the clear air radiance is the same from the two fields of view

$$I_\lambda^{cd} = I_{\lambda,1}^{cd} = I_{\lambda,2}^{cd} ,$$

and

$$I_\lambda^{c} = I_{\lambda,1}^{c} = I_{\lambda,2}^{c} ,$$

then

$$\frac{\eta_1 (I_\lambda^{cd} - I_\lambda^{c})}{\eta_2 (I_\lambda^{cd} - I_\lambda^{c})} = \frac{\eta_1}{\eta_2} = \eta^* = \frac{I_{\lambda,1} - I_\lambda^{c}}{I_{\lambda,2} - I_\lambda^{c}}$$

η^* is the ratio of the cloud amounts for the two geographically independent fields of view of the sounding radiometer. Therefore the clear air radiance from an area possessing broken clouds at a uniform altitude is given by

$$I_\lambda^{c} = \frac{I_{\lambda,1} - \eta^* I_{\lambda,2}}{1 - \eta^*}$$

where η^* still needs to be determined. Given an independent measurement of the surface temperature, T_s, and measurements $I_{w,1}$ and $I_{w,2}$ in a spectral window channel, then η^* can be determined by

$$\eta^* = \frac{I_{w,1} - B_w(T_s)}{I_{w,2} - B_w(T_s)}$$

and I_λ^{c} for the different spectral channels can be solved. Another approach to determining η^* is to use simultaneous microwave observations and regression relations between a lower tropospheric microwave sounding brightness temperature and the associated infrared brightness temperatures observed for cloud free conditions. So if

$$I_{mw} = \sum_\lambda a_\lambda I_\lambda^{c} ,$$

then

$$I_{mw} = \sum_\lambda a_\lambda \frac{I_{\lambda,1} - \eta^* I_{\lambda,2}}{1 - \eta^*}$$

and

$$\eta^* = \frac{I_{mw} - \sum_\lambda a_\lambda I_{\lambda,1}}{I_{mw} - \sum_\lambda a_\lambda I_{\lambda,2}}$$

The partly cloudy η^* solution has been the basis of the design of the operational infrared sounders (VTPR, ITPR, HIRS, and VAS). The technique is largely credited to Smith.

SURFACE TEMPERATURE DETERMINATION

Much of what has been presented so far has assumed a knowledge of the surface temperature. In this section we shall discuss techniques to determine surface temperature.

In the infrared, the emissivity of the earth's sea and land surface is near unity. As a result, in the absence of cloud or atmospheric attenuation, the brightness temperature observed with a space-borne window radiometer is

equal to surface skin temperature. However, cloud and water vapour absorption usually prohibit direct interpretation of the window channel data so that algorithms need to be applied to the data to alleviate the influence of clouds and water vapour absorption. The algorithms and instrumental approach have evolved from the use of a single window channel on a polar orbiting satellite to the use of multi-spectral radiometer observations from both polar orbiting and geostationary satellites.

The earliest single channel approach involved a statistical histogram of brightness temperatures to separate cloud free observations from cloud contaminated observations for the purpose of obtaining sea surface temperature measurements. The following assumptions are implicit in the technique.

a) Sea surface temperature is slowly varying in space, so cloud free IR window measurements over the sea should be very repetitive, and sea surface brightness temperature values will have a high frequency of occurrence.

b) Cloud contamination will produce lower than sea surface brightness temperature values and the cloud brightness temperatures will be highly variable over an area due to variations in cloud amount, opacity, and altitude.

A typical histogram situation is shown in Figure 19. Part (a) shows the typical normal distribution obtained when all measurements are cloud free, no SST gradient exists, and 1°C class intervals are used. Part (b), on the other hand, illustrates the situation when more than half of the samples are cloud contaminated. Since the cloud-contaminated radiance temperatures are lower than the cloud free temperatures, they populate the left hand side of the histogram, but also distribute themselves normally. Only the warm side of the normal density curve formed by cloud free observations can be distinguished from the combined data in the histogram. Since the mean of the normal (Gaussian) density function (probability function) formed from clear observations is the most likely value of the SST, several schemes have been developed to infer the mean of a Gaussian probability function from knowledge of the standard deviation σ of the density function and knowledge of the geometry of one side of the distribution.

The slope method assumes that the brightness temperature frequency distribution is a normal function of the form

$$f(T) = f_s \exp\left[-(T - T_s)^2/2\sigma^2\right]$$

where f is the frequency of occurrence, $f_s = f(T_s)$ is unknown, the standard deviation σ is assumed to be known from the characteristics of the measuring instrument, and the mean temperature T_s is the quantity to be determined. Since the standard deviation of a normal probability density function occurs at the inflection points on the curve, then

$$T_s = T_{max} - \sigma$$

where T_{max} is the solution of

$$\frac{d^2 f}{dT^2} = 0 ,$$

and σ is determined from the equation,

$$\sigma = (\sigma_N^2 + \sigma_E^2)^{\frac{1}{2}} ,$$

where σ_N and σ_E are the standard deviations, respectively, of the instrument noise and the expected variance of the SST's.

The three point method also assumes a normal probability function, and solves for T_s by selecting three points (T_i, f_i), (T_j, f_j), and (T_k, f_k) on the warm side of the histogram as follows

$$f_i = f_s \exp\left[-(T_i - T_s)^2/2\sigma^2\right]$$

$$f_j = f_s \exp\left[-(T_j - T_s)^2/2\sigma^2\right]$$

$$f_k = f_s \exp\left[-(T_k - T_s)^2/2\sigma^2\right].$$

These three equations contain three unknowns f_s, σ, and T_s and can be solved by simple Gaussian elimination. Therefore

$$\ln(f_i/f_j) = -\left[(T_i^2 - T_j^2) - 2T_s (T_i - T_j)\right]/2\sigma^2,$$

$$\ln(f_i/f_k) = -\left[(T_i^2 - T_k^2) - 2T_s (T_i - T_k)\right]/2\sigma^2,$$

of, finally,

$$T_s = \frac{T_i^2 \ln (f_j/f_k) - T_j^2 \ln (f_i/f_k) + T_k^2 \ln (f_i/f_j)}{2\left[T_i \ln (f_j/f_k) - T_j \ln (f_i/f_k) + T_k \ln (f_i/f_j)\right]}.$$

Since a single calculation of T_s can be influenced by noise and by the combination of the three points being slightly non-Gaussian, repeated calculations of T_s are made from all possible unique combinations of three points on the warm side of the histogram. Thus, if there are n useful points on the warm side, then the combinations: $i = 1, \ldots, n-2$; $j = i+1, \ldots, n-1$; and $k = j+1, \ldots, n$; are used to construct a second histogram, called the mean estimate histogram from which the most frequently occurring estimate is taken as the correct one.

Another solution is through a least squares fit of the normal distribution probability function to three or more points on the warm end of the observed frequency distribution. It follows from before that

$$\ln (f(T)) = \ln (f_s) - \frac{T_s^2}{2\sigma^2} + \frac{T_s T}{\sigma^2} - \frac{T^2}{2\sigma^2}$$

which has the form

$$\ln (f(T)) = A_o + A_1 T + A_2 T^2 ,$$

where $T_s = -A_1/2A_2$,

and $\sigma = -\frac{1}{2}A_2$.

Thus, given three or more points (f_i, T_i) on the cloud free portion of the histogram, one can solve for T_s and σ using the least squares solution.

Several Multispectral methods have evolved to filter out clouds from the area of interest. During daytime visible and infrared window data can be combined as follows. Low reflectance measurements will result from thin cirrus cloud or cloud free conditions, the two being easily separable in

the infrared window measurements by the drastic difference in the emitting temperature of the high cold circus and the warm underlying surface. High reflectance measurements result from thick clouds at all levels, and the infrared window brightness temperature provides a good indication of the cloud level. Intermediate reflectance data are subject to ambiguous interpretations since they result from a mixture of cloud and surface contributions. Therefore, for the purpose of estimating the surface temperature from infrared brightness temperature data, cloud contamination of the temperature frequency distribution can be minimized by eliminating all data for which the corresponding visible channel reflectances are greater than the expected cloud free reflectance values

At night the difference between the brightness temperatures measured in the 3.7 - 4.0 μm and in the 10-11 μm window regions can be used to minimize the contamination of partial cloud or thin cloud within the instrument's field-of-view. Small or negative differences are observed only for the case where an opaque scene (such as thick cloud or the surface) fills the field-of-view of the sensor. The negative difference at night results for the extended cloud condition due to the lower emissivity of cloud at 3.7 μm than at 11 μm. Moderate to large differences result if a non-uniform scene (e.g., broken cloud) is observed. The different spectral response to a scene of non-uniform temperature is a result of Planck's law; the brightness temperature dependence on the warmer portion of the scene increasing with decreasing wavelength.

The surface temperature is available from these two infrared windows at night (when reflected sunlight does not interfere with the observations in the 3.7 - 4.0 μm region). The derivation goes as follows. Given a partly cloudy atmospheric olumn then η^* can be derived from each window channel viewing two adjacent fields of view as before

$$\eta^* = \frac{I_{w1,1} - B_{w1}(T_s)}{I_{w1,2} - B_{w1}(T_s)} = \frac{I_{w2,1} - B_{w2}(T_s)}{I_{w2,2} - B_{w2}(T_s)} .$$

T_s is that value that satisfies this equality. Also one can show that

$$B_{w1}(T_s) = A_o + A_1 B_{w2}(T_s)$$

where

$$A_o = \frac{I_{w1,1} I_{w2,2} - I_{w2,1} I_{w1,2}}{I_{w2,1} - I_{w2,2}}$$

and

$$A_1 = \frac{I_{w1,1} - I_{w1,2}}{I_{w2,1} - I_{w2,2}} .$$

Thus it follows that for constant cloud height and surface temperature conditions, the observed radiances for the two window channels will both vary linearly with cloud amount. As a consequence, cloud amount variations produces a linear variation of the radiance observed in one window channel relative to that radiance observed in another window channel. This linear relation can be used to determine the value of the window radiances for zero cloud amount (η=0). As shown in figure 20, zero cloud amount must be at the intersection of the observed linear relationship and the known Planck radiance relationship. The brightness temperature associated with this point

is the surface temperature. Another common point for the observed and Planck functions is for the case of complete overcast cloud ($\eta = 1$). The brightness temperature associated with this point is the cloud temperature. It follows that the constants of the observed linear relationship are the A_o and A_1 constants of the previous equation.

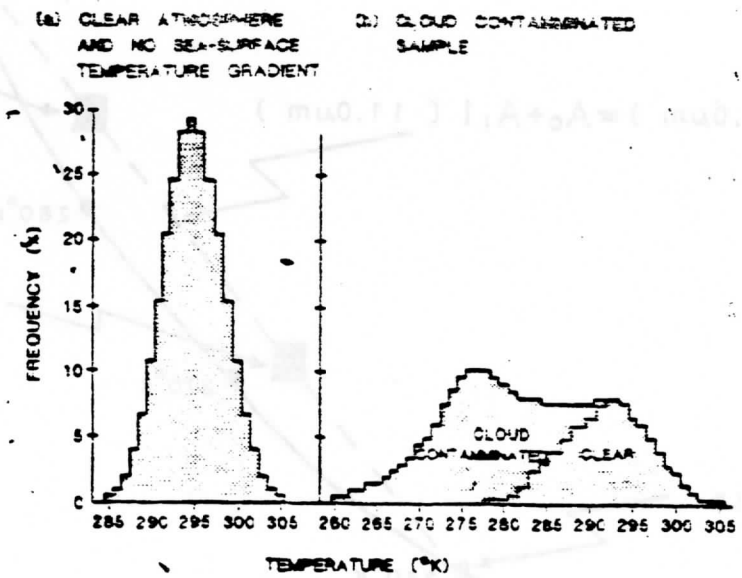

FIGURE 19: Histograms of brightness temperature in cloud free and cloud contaminated conditions.

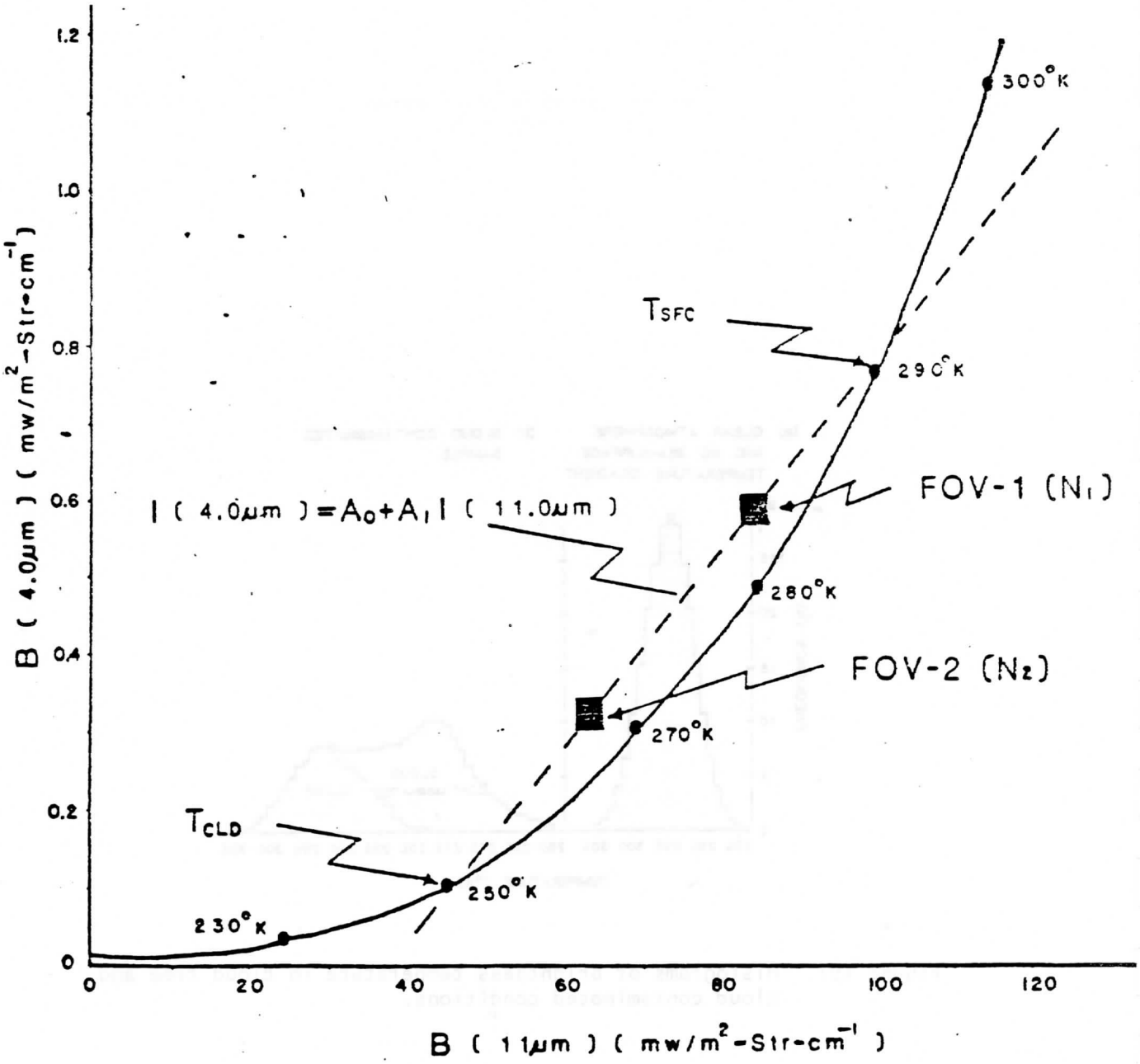

FIGURE 20: Ratio of the radiances for the two window channels; solid curve is the theoretical cloud free curve and dashed curve is the linear variation with cloud amount.

LECTURE 9

WATER VAPOR CORRECTION FOR SST DETERMINATIONS

As indicated earlier, the brightness temperature observed with a satellite radiometer can be equated to surface skin temperature after the effects of clouds have been alleviated and the atmospheric water vapor absorption has been taken into account. Having discussed cloud filtering techniques, we now address the problem of water vapor correction.

The surface temperature can be expressed in terms of the observed clear sky window channel brightness temperature, T_b, and a water vapor correction, ΔT;

$$T_S = T_b + \Delta T$$

The water vapor correction ranges from a few tenths of a degree Kelvin in very cold and dry atmospheres to nearly 10° Kelvin in very warm and moist atmospheres for 11 μm window observations. The corresponding corrections for the 3.7 μm window are about half as large. The water vapor correction is highly dependent on wavelength. To see why this is so consider that at 3.7 μm, the Planck radiance varies with temperature to approximately the thirteenth power whereas at 11 μm the Planck radiance varies with temperature to approximately the fourth power. Inserting

$$B_\lambda(T) \sim T^{n_\lambda} \quad ,$$

into the RTE we find that

$$T_{b\lambda} \sim \left[\tau_\lambda(p_s)\, T_S^{\,n_\lambda} + (1 - \tau_\lambda(p_s))\, T_a^{\,n_\lambda} \right]^{1/n_\lambda}$$

where $\tau_\lambda(p_s)$ is the atmospheric transmittance, T_S is the surface temperature, and T_a is the effective atmospheric temperature. Assuming representative values of 0.8, 300°K, and 270°K for τ_S, T_S, and T_a, respectively, one finds that at 3.7 μm where $n_\lambda = 13$, the brightness temperature observed is 296.5°K as opposed to a value of 294.5°K observed at 11 μm where $n_\lambda = 4$. Clearly for a non-isothermal condition and the same atmospheric transparency, the water vapor correction does depend on wavelength. Figure 21 illustrates the water vapor corrections derived for the Nimbus-2 3.7 μm channel and the 11 μm channel of the NOAA satellites. As can be seen, the correction for molecular absorption in the llmm region is about twice as large as that for the 3.7 μm region due to the Planck radiance dependence discussed above. Note also the dependence of the water vapor correction on viewing angle.

The water vapor correction is best evaluated by observing the area of interest in multiple infrared window channels. In the atmospheric window regions the absorption is weak, so that of W denotes the window channel wavelength.

$$\tau_W = e^{-K_W u} \sim 1 - K_W u$$

and

$$d\tau_W = - K_W du$$

What little absorption exists is due to water vapor, therefore u is a measure of precipitable water. The RTE can be written in the window region

$$I_W = B_{SW}(1-K_W u_S) + K_W \int_o^{u_S} B_W du$$

where S denotes surface. Defining an atmospheric mean Planck radiance

$$\bar{B}_W = \int_o^{u_S} B_W \, du \; / \int_o^{u_S} du$$

then

$$I_W = B_{SW}(1-K_W u_S) + K_W u_S \bar{B}_W .$$

Since B_{SW} is close to both i_W and $\bar{B}_W$, first order Taylor expansion about the surface temperature T_S allows us to linearize the RTE with respect to temperature, so

$$T_{bW} = T_S (1-K_W u_S) + K_W u_S \bar{T}_W ,$$

where $\bar{T}_W$ is the mean atmospheric temperature corresponding to $\bar{B}_W$. For two window channel wavelengths (11 and 12 μm) the following ratio can be determined.

$$\frac{T_S - T_{bW1}}{T_S - T_{bW2}} = \frac{K_{W1} u_S (T_S - \bar{T}_{W1})}{K_{W2} u_S (T_S - \bar{T}_{W2})} .$$

Assuming that the mean atmospheric temperature measured in the one window region is comparable to that measured in the other, $\bar{T}_{W1} \sim \bar{T}_{W2}$, we can simplify to

$$\frac{T_S - T_{bW1}}{T_S - T_{bW2}} = \frac{K_{W1}}{K_{W2}} ,$$

from which it follows that

$$T_S = T_{bW1} + \frac{K_{W1}}{K_{W2}-K_{W1}} [T_{bW1} - T_{bW2}] .$$

This is the split window channel expression for the water vapor correction to the SST. The term split window is used to denote two neighboring channels in a relatively transparent or window region of the spectrum; one channel for which the atmosphere is highly transparent and the other for which atmospheric water vapor partially absorbs the surface radiance to space. For three window channels (the 3.7, 11, and 12 μm) the analogous expression is

$$T_S = T_{bW1} + \frac{K_{W1}}{2(K_{W2}-K_{W1})} [T_{bW1}-T_{bW2}] + \frac{K_{W1}}{2(K_{W3}-K_{W1})} [T_{bW1}-T_{bW3}]$$

Figure 22 provides a graphical representation of the multispectral window channel water vapor correction algorithm. This linear extrapolation technique was first proposed by Anding and Kauth (1970) and initially tested by Prabhakara et al., (1974). Accuracies of 1.0-1.5°C absolute and 0.5-1.0°C relative have been routinely achieved in the last few years. Table 4 summarizes the coefficients applicable to the current satellite sounders.

The operational satellites currently in use for the SST determinations are the TIROS-N and GOES. The TIROS-N High resolution Infrared Sounder (HIRS) is well suited to measure surface temperatures since it detects radiation in the water vapor absorption bands and in the window channels. However,

observations from the TIROS-N series of satellites are not always timely (overpasses occur only four times per day over any given region) and the field of view of the HIRS radiometer is not always of high enough resolution (30 km square). On the other hand the GOES satellite visible Infrared Spin Scan Radiometer (VISSR) lacks the water vapor channel data to correct its window channel measurements, but it does offer half hourly images at 8 km resolution. Thus timely observations are available and the influence of clouds can often be alleviated by simply waiting for them to move out of the area of interest. Also a given geographical region is always observed from the same viewing angle with the VISSR so that relative variations of observed surface temperature variations rather than to variations in scan geometry. Zandlo et.al. (1982) presented a method for exploiting the capability of TIROS-N to specify the surface skin temperature and the ability of the GOES to monitor surface changes with fine horizontal and temporal resolution. The technique assumes that atmospheric absorption due to water vapor varies slowly in space and time relative to the space and time scales of the GOES observations. This allows a horizontally varying absorption correction field derived from six-hourly TIROS-N data to be used in obtaining quasi-continuous surface temperature features from the higher spatial and temporal resolution GOES data. Simultaneous TIROS-N (i.e., HIRS) and GOES (i.e., VISSR) data are used to specify a field of temperature differences between corrected TIROS-N window channel brightness temperatures. The resulting field of differences is then available to correct GOES derived temperature fields within up to 6 h (subject to synoptic changes in the atmospheric state).

When it becomes routinely available, the multispectral window radiometer data from the geostationary VISSR Atmospheric SOunder (VAS) will enable both precise water vapor correction and cloud filtering through quasi-continuous sampling with just one instrument.

TOTAL WATER VAPOR ESTIMATION

The split window method can be used to specify total water vapor concentration from clear sky 11 μm and 12 μm brightness temperature measurements. In the previous derivation, it was shown that for a window channel

$$u_S = \frac{T_{bW} - T_S}{K_W(\overline{T}_W - T_S)} \quad .$$

obviously the accuracy of the determination of the total water vapor concentration depends upon the contrast between the surface temperature, T_S, and the effective temperature of the atmosphere, $\overline{T}_W$. In an isothermal situation, the total precipitable water vapor concentration is indeterminate. The split window approximation allows us to write

$$T_S = \frac{K_{W2}T_{bW1} - K_{W1}T_{bW2}}{K_{W2} - K_{W1}} \quad ,$$

and if we express $\overline{T}_W$ as proportional to T_S

$$\overline{T}_W = \alpha_W T_S ,$$

then a solution for u_S follows;

$$u_S = \frac{T_{bW2} - T_{bW1}}{(\alpha_{W1} - 1)(K_{W2}T_{bW1} - K_{W1}T_{bW2})}$$

$$= \frac{T_{bW2} - T_{bW1}}{\beta_1 T_{bW1} - \beta_2 T_{bW2}} \quad .$$

The coefficients β_1 and β_2 can be evaluated in a linear regression analysis from prescribed temperature and water vapor profile conditions coincident with in-situ observations of u_s. The weakness of the method is due to the time and spatial variability of α_w and the insensitivity of a stable lower atmospheric state when $T_{bW1} \sim T_{bW2}$ to the total precipitable water vapor concentration.

WATER VAPOR PROFILE SOLUTION

The linear form of the RTE can be written in terms of the precipitable water vapor profile as

$$(\Delta T_b)_\lambda = \int_o^{u_s} (\Delta T)\, V_\lambda \, du$$

where

$$V_\lambda = \left[\frac{\partial B_\lambda(T)}{\partial T}\bigg|_{T=\overline{T}} \Big/ \frac{\partial B_\lambda(T)}{\lambda T}\bigg|_{T=\overline{T}_{b\lambda}} \right] \frac{\partial \tau_\lambda}{\partial u}$$

and $\overline{T}_{b\lambda}$ and $\overline{T}(p)$ represent a mean or initial profile condition.

One manner of solving for the water vapor profile from a set of spectrally independent water vapor radiance observations is to employ one of the linear direct temperature profile solutions discussed earlier. In this case, however, one solves for the function T(u) rather than T(p). Given T(p) from a prior solution of carbon dioxide and/or oxygen channel radiance observations, u(p) can be found by relating T(p) to T(u). The mixing ratio profile, q(p), can then be obtained by taking the vertical derivative of u(p), $q(p)=g\partial u/\partial p$ where g is gravity.

Rosenkranz et.al. (1982) have applied this technique to microwave measurements of water vapor emission. They used the regression solution for both the temperature verus pressure and temperature versus water vapor concentration profiles. The regression solutions have the form

$$T(p_j) = t_o(p_j) + \sum_{i=1}^{N} t_i(p_j) T_{bi}$$

and

$$T(u_k) = t_o(u_k) + \sum_{\ell=1}^{M} t_\ell(u_k) T_{b\ell}$$

where T_{bi} are the N brightness temperature observations of oxygen emission and $T_{b\ell}$ are the M brightness temperature observations of water vapour emission and $t_i(p_j)$ and $t_\ell(u_k)$ are the regression coefficients corresponding to each pressure and water vapor concentration level. u(p) is found from the intersections of the T(p) and T(u) profiles obtained by interpolation of the discrete values given by the regression solutions. An advantage of the linear regression retrievals is that they minimize the computer requirements for real-time data processing since the regression coefficient matrices are predetermined.

Various non-linear iterative retrieval methods for inferring water vapor profiles have been developed and applied to satellite water vapor spectral radiance observations. The formulation given below follows that given by Smith (1970). Integrating the linear RTE by parts one has

$$T_{b\lambda} - T_{b\lambda}^{(n)} = \int_o^{P_s} (\tau_\lambda(p) - \tau^{(n)}(p)) X_\lambda^{(n)}(p) \frac{dp}{p}$$

where

$$X_\lambda^{(n)} = \left[\left. \frac{\partial B_\lambda(T)}{\partial T} \right|_{T=\overline{T}} \Big/ \left. \frac{\partial B_\lambda(T)}{\partial T} \right|_{T=\overline{T}_{b\lambda}} \right] \frac{\partial T}{\partial \ell n p}$$

and the (n) superscript denotes the n^{th} estimate of the true profile. Expanding $\tau_\lambda(p)$ as a logarithmic function of the precipitable water vapor concentration u(p) yields

$$\tau_\lambda(p) - \tau_\lambda^{(n)}(p) = \frac{\partial \tau_\lambda(p)}{\partial \ell n\, u^{(n)}(p)} \ell n \frac{u(p)}{u^{(n)}(p)}.$$

Using the approximation

$$\frac{\partial \tau_\lambda(p)}{\partial \ell n\, u^{(n)}(p)} = \tau^{(n)}(p)\, \ell n \tau_\lambda^{(n)}(p)$$

which is valid for the exponential transmiss ion function, then

$$T_{b\lambda} - T_{b\lambda}^{(n)} = \int_o^{P_s} \ell n \frac{u(p)}{u^{(n)}(p)} Y_\lambda^{(n)}(p) \frac{dp}{p}$$

with

$$Y_\lambda^{(n)}(p) = \tau_\lambda^{(n)}(p)\, \ell n\, \tau_\lambda^{(n)}(p)\, X_\lambda^{(n)}.$$

Following the same strategy employed in Smith's generalized iterative temperature profile solution, we realize that from each water vapor channel brightness temperature an estimate of the ratio of the true precipitable water vapor profile with respect to the nth estimate can be calculated by

$$\left[\frac{u(p)}{u^{(n)}(p)} \right]_\lambda = \exp \left[\frac{T_{b\lambda} - T_{b\lambda}^{(n)}}{\int_o^{P_s} Y_\lambda^{(n)}(p) \frac{dp}{p}} \right].$$

As in the temperature profile solution, the best average estimate of the precipitable water vapor profile is based upon the weighted mean of all water vapor channel estimates using the weighting function $Y_\lambda^{(n)}(p)$.

It follows that the mixing ratio profile $q^{n+1}(p)$ can be estimated from $u^{(n+1)}(p_j)/u^{(n)}(p_j)$ as determined above and from $q^n(p_j)$ by using

$$q^{n+1}(p) = q^n(p) \left[\frac{u^{(n+1)}(p)}{u^{(n)}(p)} \right] + g\, u^{(n)}(p) \frac{\partial}{\partial p} \left[\frac{u^{(n+1)}(p)}{u^{(n)}(p)} \right].$$

The advantage of using this expression to compute q(p) is that the second term on the right hand side is small compared to the first term so that numerical errors produced by the vertical differentiation are small.

It should be noted that the relative humidity is an immediate by-product of the above derivation. Assuming that the relative humidity is constant within the radiating layer, one can write $\ell n(Rh/Rh^{(n)}) = \ell n(u/u^{(n)})$ and thus determine true Rh from the n^{th} estimate $Rh^{(n)}$.

TABLE 4. Surface skin temperature expressed as a linear combination of window brightness temperature observations, $T_S = A_o + \Sigma A_i T_{bi}$.

For the VISSR Atmospheric Sounder on GOES-5

A_o	A(3.9 μm)	A(11.2μm)	A(12.0μm)	RMS [a]
11.0	0.69	1.10	-0.83	0.5°C

For the AVHRR on TIROS-N

A_o	A(3.8μm)	A(11.0μm)	-	RMS [b]
1.58	1.55	-0.55		0.6°C

A_o	-	A(10.8μm)	A(12.0μm)	RMS [c]
-0.07		3.83	-2.83	0.2°C

[a] Bates and Smith

[b] McClain et al

[c] Barton

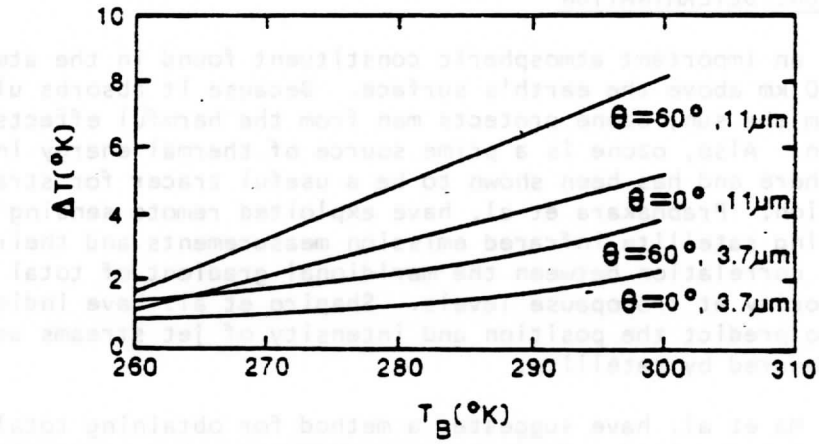

Figure 21. Nimbus 2 water vapor corrections for the 3.7 m channel and the 11 m channel for viewing angles of 0° and 60°.

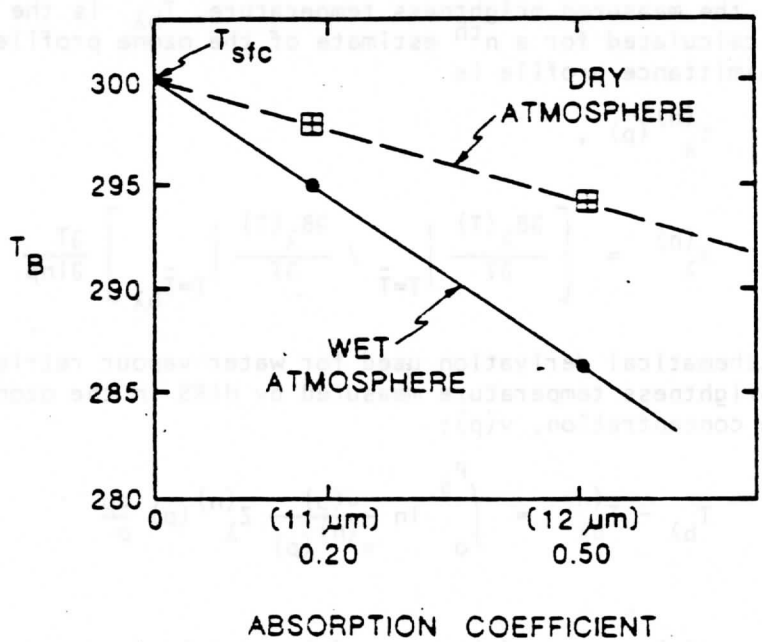

Figure 22. Graphical representation of the multispectral window channel water vapor correction algorithm.

LECTURE 10

TOTAL OZONE DETERMINATION

Ozone is an important atmospheric constituent found in the atmosphere between 10 and 50 km above the earth's surface. Because it absorbs ultraviolet rays from the sun, ozone protects man from the harmful effects of ultraviolet radiation. Also, ozone is a prime source of thermal energy in the low stratosphere and has been shown to be a useful tracer for stratospheric circulation. Prabhakara et al. have exploited remote sensing of the total ozone using satellite infrared emission measurements and their studies reveal a strong correlation between the meridional gradient of total ozone and the wind velocity at tropopause levels. Shapiro et al. have indicated a possibility to predict the position and intensity of jet streams using total ozone measured by satellite.

Recently Ma et al. have suggested a method for obtaining total ozone with high spatial resolution from the TIROS-N/NOAA series of satellites. The ozone concentration is mapped with the 9.6 μm ozone radiance observations by the High-resolution Infrared Radiation Sounder (HIRS). The meteorological inferences have a resolution of 75 km. Using the previously discussed algorithms when processing the data, the influence of clouds on the ozone determinations is alleviated.

Ozone concentration is related to radiance to space through the transmittance $\tau_\lambda(p)$. As shown in the water vapour profile solution, using a first order Taylor expansion of Planck function in terms of temperature and integrating the RTE by parts, yields the expression

$$T_{b\lambda} - T_{b\lambda}^{(n)} = \int_o^{P_s} \left[\tau_\lambda(p) - \tau_\lambda^{(n)}(p)\right] X_\lambda^{(n)}(p) \frac{dp}{p}$$

where $T_{b\lambda}$ is the measured brightness temperature, $T_{b\lambda}^{(n)}$ is the brightness temperature calculated for a n^{th} estimate of the ozone profile whose corresponding transmittance profile is

$$\tau_\lambda^{(n)}(p) ,$$

and

$$X_\lambda^{(n)} = \left[\frac{\partial B_\lambda(T)}{\partial T}\bigg|_{T=\bar{T}} \Big/ \frac{\partial B_\lambda(T)}{\partial T}\bigg|_{T=\bar{T}_{b\lambda}} \right] \frac{\partial T}{\partial \ln p}$$

Using the mathematical derivation used for water vapour retrieval, one can relate the brightness temperature measured by HIRS in the ozone 9.6 μm band to the ozone concentration, v(p);

$$T_{b\lambda} - T_{b\lambda}^{(n)} = \int_o^{P_s} \ln \frac{v(p)}{v^{(n)}(p)} Z_\lambda^{(n)}(p) \frac{dp}{p}$$

where

$$Z_\lambda^{(n)}(p) = \tau_\lambda^{(n)}(p) \ln \tau_\lambda^{(n)}(p) X_\lambda^{(n)} .$$

As suggested by Smiths generalized iterative solution, we assume that the correction to the ozone concentration $v(p) - v^{(n)}(p)$ is independent of p, so that

$$\left[\frac{v(p)}{v^{(n)}(p)}\right]_\lambda = \exp\left[\frac{T_{b\lambda} - T_{b\lambda}^{(n)}}{\int_o^{P_s} Z_\lambda^{(n)}(p)\,\frac{dp}{p}}\right] = \gamma_\lambda^n$$

Consequently, for every pressure level, one can use this iterative procedure to estimate the true ozone concentration profile

$$v^{(n+1)}(p_j) = v^{(n)}(p_j)\,\gamma_\lambda^n$$

Convergence is achieved as soon as the difference between the measured ozone brightness temperature and that calculated is less than the measurement noise level (approximately 0.2^oC). The first guess ozone profile is constructed using regression relations between the ozone concentration and the infrared brightness temperature observations of stratospheric carbon dioxide emission and the microwave brightness temperatures observations of stratospheric and tropospheric oxygen emission to space. Since ozone is a prime source of thermal energy in the low stratosphere and the upper troposphere, there is excellent correlation between the ozone concentration and the brightness temperatures observed in the HIRS carbon dioxide and MSU oxygen channels. Due to the fact that ozone and temperature sounding data yield good statistics only up to 10 mb (about 30 km), above 10 mb the ozone and temperature profiles are extrapolated using the lapse rate of USA standard ozone and temperature profiles between 10 mb and 0.1 mb (up to about 50 km). Above 50 km, the ozone contribution to the outgoing radiance is negligible.

The profile shape and the vertical position of the peak ozone mixing ratio corresponding to the ozone guess profile is crucial to obtaining a satisfactory retrieval since only one ozone channel radiance in the 9.6 μm band is used. This is because the true ozone profile is assumed to have the same shape as the first guess. Therefore to make the ozone guess profile sufficiently accurate in both shape and position of the ozone peak mixing ratio, adjustments to the vertical position and amplitude of the guess peak mixing ratio are made based on the difference between the observed brightness temperature and the calculated brightness temperature using the ozone guess profile.

Recent simulations and real data retrievals indicate that the total ozone concentration can be retrieved with an accuracy better than 5%. Figure 23 shows a scatter diagram of point comparisons of TOMS (Total Ozone Mapping Spectrometer) estimates of total ozone and HIRS physical total ozone retrievals for April 30, 1982.

CLOUD HEIGHT DETERMINATION

The determination of cloud heights is important for many meteorological applications, especially the estimation of the pressure-altitude of winds obtained by tracing clouds from time sequenced satellite images. Several methods for determining cloud heights using satellite data have been developed over the years. One method (Fritz and Winston, 1962) compares the infrared window channel brightness temperature with a vertical temperature profile in the area of interest to obtain the height of the cloud. This infrared window cloud height determination assumes that the cloud is opaque and fills the satellite instruments field-of-view, and thus it works fine for dense stratoforms of cloud. However, it is inaccurate for semi-transparent cirrus clouds and small-element cumulus clouds. A second method (Mosher, 1976, and Reynolds and Vonder Haar, 1977) improves the infrared window channel estimate of cloud top height by allowing for fractional cloud cover and by

estimating the cloud emissivity from visible reflectance data. Using a multiple scattering model, the visible brightness of the cloud is used to calculate the optical thickness, from which the infrared emissivity of the cloud can be computed. Although this bi-spectral method is an improvement over the first method, it is still inaccurate for semi-transparent cirrus clouds. A third method utilizes stereographic observations of clouds from two simultaneously scanning geosynchronous satellites (Hasler, 1981). These stereo height measurements depend only on straight forward geometrical relationships and offer more reliable values than the previously discussed infrared-based methods. However, the stereo method is limited to the overlap region of the two satellites and to times when simultaneous measurements can be orchestrated.

The CO_2 absorption methods enables one to assign a quantitative cloud top pressure to a given cloud element using radiances from the CO_2 spectral bands. Recalling that the radiance from a partly cloudy air column region by

$$I_\lambda = \eta I_\lambda^{cd} + (1-\eta)\, I_\lambda^{cl}$$

where η is the fractional cloud cover, I_λ^{cd} is the radiance from the cloud obscured field of view, and I_λ^{cl} is the radiance from a clear field of view for a given spectral band λ. The cloud radiance is given by

$$I_\lambda^{cd} = \varepsilon_\lambda\, I_\lambda^{bcd} + (1-\varepsilon_\lambda)\, I_\lambda^{cl}$$

where p_c is the cloud top pressure, ε_λ is the emissivity of the cloud, and I_λ^{bcd} is the radiance from a completely opaque cloud (black cloud). Using the RTE we can write

$$I_\lambda^{cl} = B_\lambda(T(p_s))\tau_\lambda(p_s) + \int_{p_s}^{o} B_\lambda(T(p))\, d\tau_\lambda ,$$

$$I_\lambda^{bcd} = B_\lambda(T(p_c))\tau_\lambda(p_c) + \int_{p_c}^{o} B_\lambda(T(p))\, d\tau_\lambda .$$

Integrating by parts and subtracting the two terms we get

$$I_\lambda^{cl} - I_\lambda^{bcd} = \int_{p_c}^{p_s} \tau_\lambda(p)\, dB_\lambda$$

therefore

$$I_\lambda - I_\lambda^{cl} = \eta\varepsilon_\lambda \int_{p_s}^{p_c} \tau_\lambda(p)\, dB_\lambda ,$$

where $\eta\varepsilon_\lambda$ is often called the effective cloud amount. The ratio of the deviations in cloud produced radiances and corresponding clear air radiances for two spectral channels, λ_1 and λ_2, viewing the same field of view can thus be written

$$\frac{I_{\lambda 1} - I_{\lambda 1}^{cl}}{I_{\lambda 2} - I_{\lambda 2}^{cl}} = \frac{\varepsilon_{\lambda 1} \int_{p_s}^{p_c} \tau_{\lambda 1}(p)\, dB_{\lambda 1}}{\varepsilon_{\lambda 2} \int_{p_s}^{p_c} \tau_{\lambda 2}(p)\, dB_{\lambda 2}}$$

If the wavelengths are chosen to be close enough together, then $\varepsilon_1 = \varepsilon_2$, and one has an expression by which the pressure of the cloud within the field-of-view (FOV) can be specified.

The left side can be determined from TIROS or VAS observed radiances and clear air radiances calculated from a known temperature and moisture profile. Alternatively, the clear air radiances could be provided from spatial analyses of TIROS or VAS clear sky radiance observations. The right side is calculated from known temperature profile and the profiles of atmospheric transmittance for the spectral channels as a function of P_c, the cloud top pressure. The optimum cloud top pressure is determined when the absolute difference $|\text{right } (\lambda_1,\lambda_2) - \text{left } (\lambda_1,\lambda_2,P_c)|$ is a minimum.

These are two basic assumptions inherent in this method:

(a) that the cloud has infinitesimal thickness; and
(b) that the cloud emissivity is the same for the two spectral channels.

The maximum possible error caused by assumption (a) is one-half the cloud thickness. Errors approaching one-half the cloud thickness occur for optically thin clouds (integrated emissivity roughly less than .6); for optically thick clouds (integrated emissivity roughly greater than .6) the error is small, typically one-fourth the cloud thickness or less. Errors due to assumption (b) can be minimized by utilizing spectrally close channels.

Once a cloud height has been determined, an effective cloud amount can be evaluated from the infrared window channel data using the relation

$$\eta\varepsilon_w = \frac{I_w - I_w^{cl}}{B_w\,(T(p_c)) - I_w^{cl})}$$

where w represents the window channel wavelength, and $B_w\,(T(p_c))$ is the window channel opaque cloud radiance.

Using the ratios of radiances of the three CO_2 spectral channels on the VAS two separate cloud top pressures can be determined (14.2/14.0 and 14.2/13.3). If $(I_\lambda - I_\lambda^{cl})$ is within the noise response of the instrument (roughly 1 mw/m^2 - ster - cm^{-1}) the resulting p_c is rejected. Using the infrared window and the two cloud top pressures, two effective cloud amount determinations are made. To select the most representative cloud height P_{ck}, the algorithm checks the differences between the observed values of $(I_\lambda - I_\lambda^{cl})$ and those calculated from the radiative transfer equation for the two possible cloud top pressures and effective cloud amounts,

$$\left|(I - I^{cl})_\lambda - N\varepsilon_k \int_{p_s}^{P_{ck}} \tau_\lambda \, dB_\lambda \right| = M_{\lambda k} .$$

P_{ck} is chosen when

$$\sum_{\lambda=1}^{3} M_{\lambda k}^{\,2}$$

is a minimum, where the sum is over the three CO_2 channels need to derive the cloud top pressure values.

If neither ratio of radiances (14.2/14.0 or 14.2/13.3) can be reliably calculated because $(I-I^{cl})$ is within the instrument noise level, then a cloud top pressure is calculated directly from the VAS observed 11.2 μm infrared window channel brightness temperature and the temperature profile. In this way all clouds can be assigned a cloud top pressure either by CO_2 absorption or by infrared window calculations.

Menzel et al. utilized the CO_2 absorption method to make several comparisons of cloud heights determined by different techniques; the comparisons were randomly made over several different cloud types including thin cirrus clouds. The CO_2 heights were found to be reliable within about a 50 mb root mean square deviation of other available height determinations. The CO_2 heights produced consistently good results over thin cirrus where the bi-spectral heihgts were inconsistent. This is demonstrated more dramatically in Figure 24, where bi-spectral and CO_2 heights are plotted along a cirrus anvil blowing off the top of a thunderstorm at 1348 GMT 14 July 1982 over western Missouri and eastern Kansas. As one moves away from the dense cumulus clouds towards the thin cirrus, the CO_2 absorption method maintains high altitudes while the bi-spectral method frequently underestimates the altitude by varying amounts depending on the thinness of the cirrus clouds.

The considerable advantage of the CO_2 absorption method is that it is not dependent on the fractional cloud cover or the cloud emissivity (in fact, the effective cloud amount is a by product of the calculations).

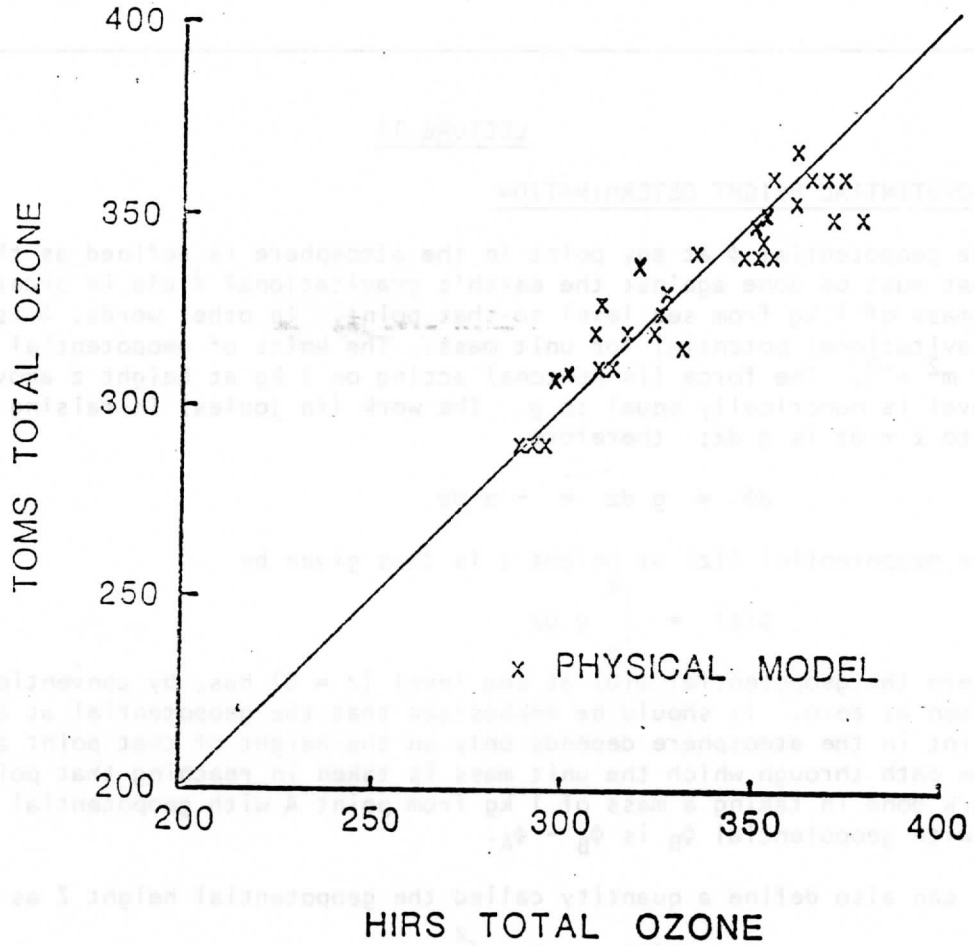

FIGURE 23: Point comparisons of TOMS estimates of total ozone (in Dobson units) and HIRS physical total ozone retrievals (in Dobson units) for April 30, 1982.

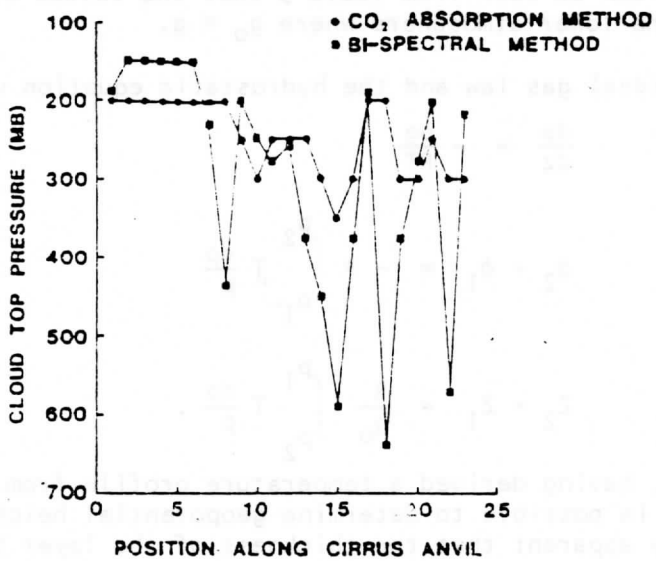

FIGURE 24: Bi-spectral and CO_2 absorption cloud-top pressures (mb) plotted versus the position along the cirrus anvil emanating from the thunderstorm over Missouri and Kansas of 1348 GMT 14 July 1982.

LECTURE 11

GEOPOTENTIAL HEIGHT DETERMINATION

The geopotential Φ at any point in the atmosphere is defined as the work that must be done against the earth's gravitational field in order to raise a mass of 1 kg from sea level to that point. In other words, Φ is the gravitational potential for unit mass. The units of geopotential are 1 kg^{-1} or $m^2\ s^{-2}$. The force (in newtons) acting on 1 kg at height z above sea level is numerically equal to g. The work (in joules) in raising 1 kg from z to z + dz is g dz; therefore,

$$d\Phi = g\ dz = -\alpha\ dp$$

The geopotential $\Phi(z)$ at height z is thus given by

$$\Phi(z) = \int_0^z g\ dz$$

where the geopotential $\Phi(0)$ at sea level (z = 0) has, by convention, been taken as zero. It should be emphasized that the geopotential at a particular point in the atmosphere depends only on the height of that point and not on the path through which the unit mass is taken in reaching that point. The work done in taking a mass of 1 kg from point A with geopotential Φ_A to point B with geopotential Φ_B is $\Phi_B - \Phi_A$.

We can also define a quantity called the geopotential height Z as

$$Z = \frac{\Phi(z)}{g_o} = \frac{1}{g_o} \int_0^z g\ dz$$

where g_o is the globally averaged acceleration due to gravity at the earth's surface (taken as 9.8 ms^{-2}). Geopotential height is used as the vertical coordinate in most atmospheric applications in which energy plays an important role. It can be seen from Table 5 that the values of z and Z are almost the same in the lower atmosphere where $g_o \simeq g$.

From the ideal gas law and the hydrostatic equation we are able to write

$$\frac{dp}{dz} = -\frac{pg}{RT}$$

so that

$$\Phi_2 - \Phi_1 = -R \int_{p_1}^{p_2} T\ \frac{dp}{p}$$

or

$$Z_2 - Z_1 = \frac{R}{g_o} \int_{p_2}^{p_1} T\ \frac{dp}{p}\ .$$

Therefore, having derived a temperature profile from sounding radiance measurements, it is possible to determine geopotential heights (or thicknesses). It is readily apparent that the thickness of the layer between any two pressure levels p_2 and p_1 is proportional to the mean temperature of the layer; as T increases the air between the two pressure levels expands so that the layer becomes thicker.

Geopotential heights and thicknesses are being processed routinely from VAS soundings at the University of Wisconsin-Madison. As part of the NOAA Operational VAS Assessment, NOAA at Wisconsin has been forwarding these data to the National Hurricane Center for comparison with conventional radiosonde and drop wind sonde determinations. Table 6 shows the results for 1982. Thicknesses derived from VAS temperature soundings were excellent with a mean difference of only 10-20 meters when compared with raobs and 5-10 meters when compared with dropsondes.

Geopotential thicknesses are also routinely evaluated from the TIROS polar orbiters, but here the 850-500 and 850-200 mbar layers are estimated from a linear combination of the four MSU brightness temperature observations. Regression coefficients are determined from an analysis of radiosonde data. The 850-500 and 850-200 mbar thicknesses are useful for weather forecasting, since contour analyses of these quantities describe the direction and speed of the circulation at midtropospheric and jet stream levels, respectively. The accuracies of the MSU derived thicknesses are comparable to the accuracies experienced with the VAS derived heights and thicknesses.

AN APPLICATION TO DETERMINE TROPICAL CYCLONE INTENSITY

It has been observed that the upper tropospheric temperature structure of tropical cyclones is characterized by a well defined warm temperature anomaly at upper levels in well developed storms. An intense tropical cyclone with an eye produced by subsidence within the upper tropospheric anticyclone develops a warm core due to adiabatic warming. One theory is the warm air produced by subsidence within the eye is entrained into the eye wall where strong upward motions transport this warmer air to high levels where it then diverges outward away from the eye region.

It has been shown to be possible to monitor the intensity of tropical cyclones as categorized by its surface central pressure and maximum sustained wind speed at the eye wall with satellite microwave observations. The relationship between surface pressure and the intensity of the warm core comes from the ideal gas law and the hydrostatic equation

$$\frac{dp}{p} = -\frac{g}{RT}\,dz$$

or

$$\ln\left(\frac{p_s}{p_t}\right) = \frac{g}{R}\int_o^{z_t}\frac{dz}{T}$$

where p_s is the surface pressure and p_t and z_t are the pressure and height of some level which is undisturbed by the tropical cyclone below. Thus the surface pressure is inversely related to the temperature of the column of air above. Observations show that the transition between the lower level cyclone and upper level anti-cyclone occurs in the vicinity of 10 km. Applying the above equation at the eye and its environment we find

$$\ln\left(\frac{p_s^{eye}}{p_t}\right) = \frac{g}{R}\,\frac{z_t}{\bar{T}_{eye}}$$

and

$$\ln\left(\frac{p_s^{env}}{p_t}\right) = \frac{g}{R}\,\frac{z_t}{\bar{T}_{env}}$$

where $\bar{T}$ is the mean temperature of the column between the surface and the undisturbed pressure level. Combining these expressions we can write

$$p_s^{eye} = p_s^{env} \exp\left[-\frac{gz_t}{R}\left(\frac{\bar{T}^{eye} - \bar{T}^{env}}{\bar{T}^{eye}\,\bar{T}^{env}}\right)\right]$$

Using z_t = 10 km and setting $\bar{T}^{eye}\,\bar{T}^{env} \sim (250^oK)^2$ then

$$p_s^{eye} \simeq p_s^{env} \exp\left[-.0055\,\Delta\bar{T}\right]$$

$$\simeq p_s^{env}\left[1 - .0055\,\Delta\bar{T}\right].$$

Assuming $p_s^{env} \sim 1000$ mb, then

$$p_s^{eye} - 1000 = -5.5\,\Delta\bar{T}$$

so that a 55 mb surface pressure depression is approximately associated with a 10°C contrast between the mean temperatures of the cyclone eye and its environment.

It has been found that the tropical cyclone warm core is usually strongest at about 250 mb. In addition the amplitude of the upper tropospheric temperature anomaly is well correlated with the amplitude of the mean temperature of the tropospheric column below 10 km. Therefore the Laplacian of the temperature field at 250 mb provides a measure of the strength of the warm core, which then is correlated to storm surface intensity. Furthermore, a correlation should also exist for maximum surface winds as they are directly related to the pressure field (although not pure gradient winds because of frictional effects).

In the work of Veldon and Smith (1983), two parameters ($\nabla_p^2 T_{250}$ and ΔT_{250}) are compared to observed surface central pressure and maximum winds, and a statistical basis developed. The $\nabla_p^2 T_{250}$ is defined as the Laplacian on a constant pressure surface

$$(\partial T^2_{250}/\partial x^2 + \partial T^2_{250}/\partial y^2)$$

of the 250 mb temperature field, and ΔT_{250} is the gradient of the 250 mb temperature field defined as the core temperature minus the average environmental temperature at a 6 degree radius from the storm core. Linear regression is used to find a best fit for the data. After studying three tropical cyclones they found that the standard error of estimates for the central pressure and maximum wind are 6 mb and 11 knots respectively. Table 7 shows these results. Figure 25 shows a comparison of National Hurricane Center versus satellite estimates of the central surface pressure for the duration of Hurricane Harvey.

WIND DERIVATION

Gradient winds represent motion parallel to isobars subject to balanced Coriolis, centrifugal, and pressure gradient forces. The three way balance is shown in Figure 25 for cyclonic and anti-cyclonic trajectories. In both cases, the centrifugal force is directed outward from the center of curvature of the air trajectories (denoted by the dashed lines) and has a magnitude given by V^2/R_T, where R_T is the local radius of curvature. In effect, a balance of forces can be achieved with a wind velocity smaller than would be required if the Coriolis force were acting alone. Thus, in this case, it is possible to maintain a subgeostropic flow parallel to the isobars. For the anti-cyclonically curved trajectory the situation is just the opposite: the centrifugal force opposes the Coriolis force and, in effect, necessitates a supergeostrophic wind velocity in order to bring about a three-way balance of forces.

If P_n denotes the normal component of the pressure gradient force per unit mass and f the Coriolis parameter, we can write

$$P_n = fV \pm \frac{V^2}{R_T}$$

The geopotential height fields derived from the TIROS or VAS data can be used to evaluate the gradient wind. This is accomplished by realizing

$$P_n = -\frac{1}{\rho}\frac{\partial p}{\partial n} = -g_o \frac{\partial Z}{\partial n}$$

and then solving for V by using the quadratic formula.

Thermal winds give a measure of the vertical wind shear. By taking the difference of the geostrophic equation (balanced Coriolis and pressure gradient forces) at two pressure levels (denoted here by a lower level 1 and an upper level 2), one finds

$$V_{g2} - V_{g1} = \frac{g_o}{f}\frac{\partial}{\partial n}(Z_2 - Z_1)$$

where the subscript g indicates geostrophic. The vertical wind shear is calculable from the horizontal gradient of the geopotential thickness between two pressure levels. Through the use of the thermal wind equation it is possible to define a geostrophic wind field from pressure observations at a reference level and temperature profiles over the area of interest. Thus a set of sea level pressure observations together with a grid of TIROS or VAS infrared temperature soundings constitutes a sufficient observing system for determining the three dimensional distribution of V_g.

Figure 27 shows streamlines and isotachs of 300 mb gradient winds derived from VAS temperature profile data, where the curvature term is approximated from the geopotential height field contours. As can be seen, the depiction of the flow is quite detailed with a moderately intense subtropical jet streak propagating east-southeastward in time. Such wind fields in time sequence are especially useful in nowcasting applications.

Gradient winds have also been compared on a routine basis with conventional radiosonde and drop wind sonde determinations by NHC as part of the NOVA program. Table 8 shows the results for 1982. The VAS gradient winds averaged about 30% slower than the conventionally observed winds. Several factors may be contributing to this discrepancy: ageostrophic motions, deficient height fields in data void areas, and inaccurate determination of the normal derivative of the geopotential height due to the resolution of the analysis field. Most likely the last factor is very significant. Whatever the cause, for 1982 NHC concluded that gradient winds were less useful than cloud motion winds in their analyses.

SATELLITE MEASURE OF ATMOSPHERIC STABILITY

One measure of the thermodynamic stability of the atmosphere is the total-totals index

$$TT = T_{850} + TD_{850} - 2T_{500}$$

where T_{850} and T_{500} are the temperatures at the 850- and 500-mbar levels, respectively, and TD_{850} is the 850-mbar level dew point. TT is traditionally estimated from radiosonde point values. For a warm moist atmosphere underlying cold midtropospheric air TT is high (e.g., 50-60 K), and intense convection can be expected. There are two limitations of radiosonde derived TT:

(i) the spacing of the data is too large to isolate local regions of probable

convection, and
(ii) the data are not timely being available only twice per day.

If we define the dew point depression at 850 mbar, $D_{850} = T_{850} - TD_{850}$, then

$$TT = 2(T_{850} - T_{500}) - D_{850} .$$

Although point values of temperature and dew point cannot be observed by satellite, the layer quantities observed can be used to estimate the temperature lapse rate of the lower troposphere ($T_{850} - T_{500}$) and the low level relative moisture concentration D_{850}. Assuming a constant lapse rate of temperature betw-en the 850- and 200-mbar pressure levels and also assuming that the dew point depression is proportional to the logarithm of relative humidity, it can be shown from the hydrostatic equation that

$$TT = 0.1489\ \Delta Z_{850-500} - 0.0546\ \Delta Z_{850-200} + 16.03 \ln RH,$$

where ΔZ is the geopotential thickness in meters and RH is the lower tropospheric relative humidity, both estimated from either TIROS or VAS radiance measurements as explained earlier.

Smith and Zhou reported several case studies using this approach. Figure 28 shows the total-totals stability index as observed by radiosondes and infrared from TOVS data on 31 Mar. 1981. One can see the coarse spacing of the radiosonde observations (Fig. 28(a)). The analysis of satellite data possesses much more spatial detail since the spacing of the data is only 75 km (Fig. 28(b)). There is general agreement in the high total-totals over Illinois and Missouri but also some areas of disagreement (e.g. Nebraska). In this case the radiosonde data are not as coherent an indicator of the region of intense convection as are the satellite data.

Also shown on the satellite TT analysis are the streamlines of the wind observed at the surface. On this occasion it appears that the unstable air observed along the Illinois-Iowa border at 1438 GMT was advected into central Wisconsin and supported the development of a tornadic storm at 2315 GMT.

Values of the geometric height (z), geopotential height (Z), and acceleration due to gravity (g) at 40° latitude

z (km)	Z (km)	g (m s^{-2})
0	0	9.802
1	1.000	9.798
10	9.986	9.771
20	19.941	9.741
30	29.864	9.710
60	59.449	9.620
90	88.758	9.531
120	117.795	9.443
160	156.096	9.327
200	193.928	9.214
300	286.520	8.940
400	376.370	8.677
500	463.597	8.427
600	548.314	8.186

TABLE 5.

	$\nabla^2 T_{250}$ vs P_c		ΔT_{250} vs P_c		$\nabla^2 T_{250}$ vs P_c		ΔT_{250} vs P_c		$\nabla^2 T_{250}$ vs V_{max}		ΔT_{250} vs V_{max}		$\nabla^2 T_{250}$ vs V_{max}		ΔT_{250} vs V_{max}		Number of samples
	a	b	a	b	σ (mb)	r	σ (mb)	r	a	b	a	b	σ (kt)	r	σ (kt)	r	
Harvey	1010	−1.475	1013	−16.129	5	0.94	7	0.92	25.4	2.439	21.3	26.667	12	0.90	14	0.87	12
Irene	1012	−1.473	1018	−17.241	5	0.94	6	0.90	25.3	2.320	20	30.303	9	0.93	10	0.91	13
Frederic	1020	−2.083	1017	−20.833	12	0.87	5	0.94	14.8	2.959	18.5	30.303	15	0.86	10	0.93	19
Combined	1013	−1.631	1015	−18.692	7	0.92	6	0.92	22.3	2.558	20	28.986	12	0.90	11	0.91	44

TABLE 7. Correlating central surface pressure and maximum sustained wind speed to the Laplacian of the 250 mb temperature and the average horizontal temperature gradient for Hurricanes Harvey, Irene and Frederic. a is the intercept, b the slope of the linear relation, σ is the standard deviation, and r is the correlation coefficient.

SUMMARY OF COMPARISONS BETWEEN VAS AND RADIOSONDE DATA
FOR BERMUDA, SAN JUAN, AND WEST PALM BEACH
(15 SEPTEMBER-18 NOVEMBER 1982)

Parameter	Mean (VAS-RAOB)	Standard Deviation	Range	Number of Cases
ΔZ850 (m)	11	13	-22 to 60	51
ΔZ700	18	19	-20 to 66	51
ΔZ500	27	27	-23 to 100	51
ΔZ400	29	28	-20 to 84	45
ΔZ300	37	35	-27 to 109	44
ΔZ200	43	53	-23 to 175	48
ΔZ500-850 (m)	16	18	-13 to 71	51
ΔZ400-850	20	21	-14 to 73	45
ΔZ300-850	28	30	-16 to 96	44
ΔZ500-700	9	11	-15 to 34	51
ΔZ400-700	13	16	-13 to 58	45
ΔZ200-400	9	29	-49 to 105	44

SUMMARY OF COMPARISONS BETWEEN VAS AND ODW FOR
14/15 AND 15/16 SEPTEMBER 1982

Parameter	Mean (VAS-ODW)	Standard Deviation	Range	Number of Cases
ΔZ850 (m)	-6	23	-68 to 26	42
ΔZ700	0	22	-58 to 41	42
ΔZ500	1	24	-56 to 44	35
ΔZ400	2	27	-54 to 47	24
ΔZ400-850 (m)	11	17	-16 to 45	24
ΔZ500-850	6	14	-18 to 43	35
ΔZ400-700	4	14	-16 to 34	24

TABLE 6.

SUMMARY OF COMPARISONS BETWEEN VAS AND RADIOSONDE DATA
FOR BERMUDA, SAN JUAN, AND WEST PALM BEACH
(15 SEPTEMBER-18 NOVEMBER 1982)

Parameter		Mean (VAS-RAOB)	Standard Deviation	Range	Number of Cases
ddd850	(°)	26	18	1 to 73	30
ddd700		27	24	0 to 101	27
ddd500		29	24	0 to 90	36
ddd400		30	28	2 to 134	32
ddd300		36	27	2 to 123	38
ddd200		30	21	1 to 85	42
Δff850	(kt)	-6	7	-45 to 8	46
Δff700		-4	6	-36 to 8	46
Δff500		-2	7	-21 to 12	46
Δff400		-2	9	-19 to 16	40
Δff300		-2	11	-23 to 21	41
Δff200		-10	17	-57 to 22	45

SUMMARY OF COMPARISONS BETWEEN VAS AND ODW FOR
14/15 AND 15/16 SEPTEMBER 1982

Parameter		Mean (VAS-ODW)	Standard Deviation	Range	Number of Cases
Δddd850	(°)	39	24	3 to 97	21
Δddd700		44	30	9 to 109	23
Δddd500		24	36	0 to 95	22
Δddd400		20	14	2 to 48	13
Δff850	(kt)	-5	8	-20 to 6	23
Δff700		-5	6	-14 to 4	23
Δff500		-5	7	-18 to 5	22
Δff400		-8	10	-30 to 5	13

TABLE 8.

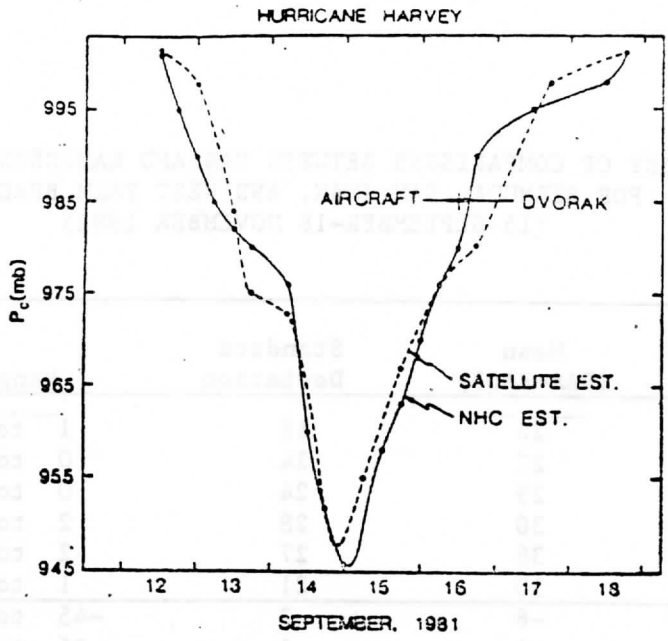

FIGURE 25. Comparison of National Hurricane Center versus satellite estimates of central surface pressure for the duration of Harvey.

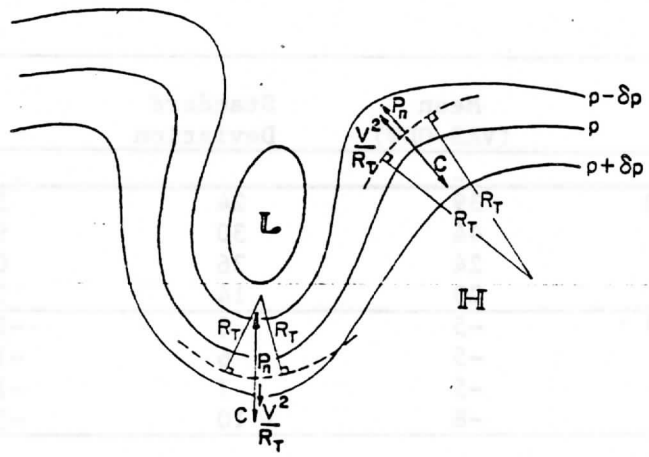

FIGURE 26. The three-way balance between the horizontal pressure gradient force, the Coriolis force and the centrifugal force, in flow along curved trajectories (----) in the Northern Hemisphere.

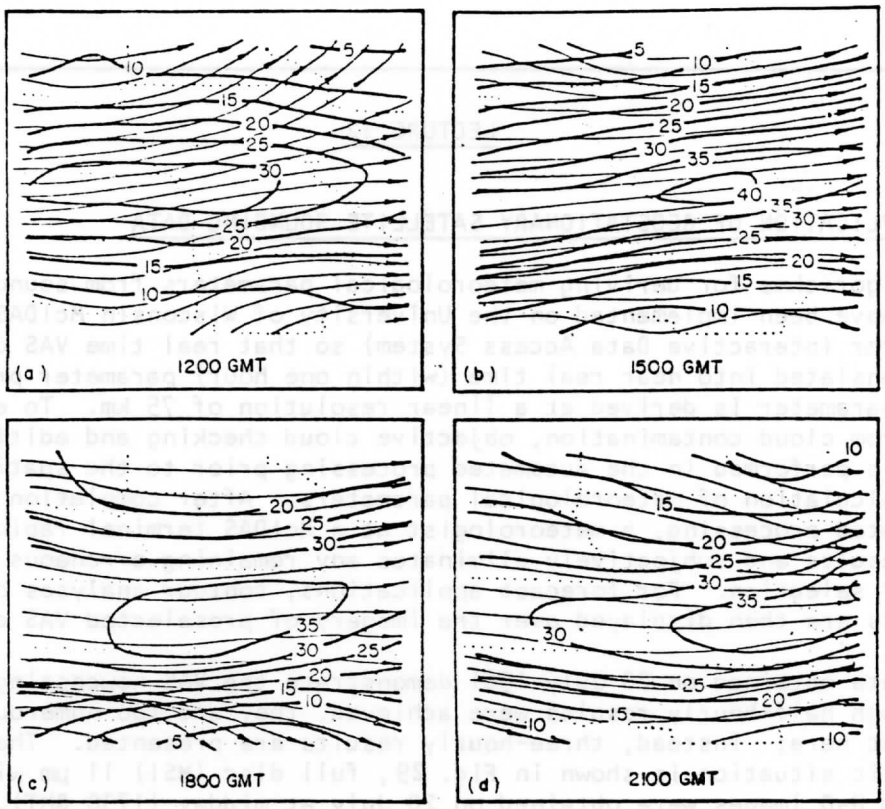

FIGURE 27. Streamlines and isotachs (ms^{-1}) of 300 mb gradient wind calculated from VAS temperature soundings: (a) 12 GMT, (b) 15 GMT, (c) 18 GMT, and (d) 21 GMT on 20 July, 1981.

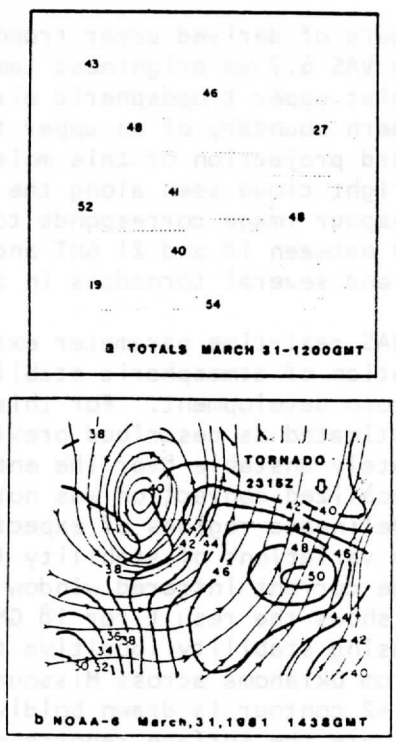

FIGURE 28. Radiosonde observations of total-totals (a) and a contour analysis (heavy lines) of NOAA-6 derived stability values with streamlines (thin lines) of the surface wind superimposed (b).

LECTURE 12

AN APPLICATION OF GEOSTATIONARY SATELLITE SOUNDING DATA

The algorithms for deriving meteorological parameters from sounding radiance data have been implemented on the University of Wisconsin McIDAS (Man computer Interactive Data Access System) so that real time VAS data ingest is translated into near real time (within one hour) parameter production. Each parameter is derived at a linear resolution of 75 km. To ensure freedom from cloud contamination, objective cloud checking and editing of the data is performed in the automated processing prior to the spatial averaging and calculation of meteorological parameters. After completion of the automated processing, a meteorologist at a McIDAS terminal rapidly inspects the results and subjectively eliminates any remaining erroneous data through cursor selection. For forecast applications, contour analyses of the results are then displayed over the imagery of preselected VAS channels.

VAS data obtained on 20 July 1981 demonstrate the VAS nowcasting capabilities. Although half-hourly results were achieved, they are too numerous to present here; instead, three-hourly results are presented. The overall synoptic situation is shown in Fig. 29, full disc (MSI) 11 μm window and 6.7 μm H_2O images were obtained on 20 July at midday (1730 GMT). The 11 μm image shows that the United States is largely free of clouds except near the United States-Canadian border where a cold front persists. However, in the 6.7 μm upper tropospheric moisture image, a narrow band of moist air (delineated by the low radiance greyish white areas of the image) stretches from the Great Lakes into the southwestern United States.

Figure 30 shows contours of derived upper tropospheric relative humidity superimposed over the VAS 6.7 μm brightness temperature images. In this case the narrow band of moist upper tropospheric air stretching across northern Missouri is the southern boundary of an upper tropospheric jet core (Figure 27). The southeastward projection of this moist band and associated jet core is seen. The bright cloud seen along the Illinois - Missouri border in the 21-GMT water vapour image corresponds to a very intense convective storm which developed between 18 and 21 GMT and was responsible for severe hail, thunderstorms, and several tornadoes in the St. Louis, Missouri, region.

An objective of the VAS real-time parameter extraction software is to provide an early delineation of atmospheric stability conditions antecedent to intense convective storm development. For this purpose a Total-Totals stability index is estimated as described previously. On this day, the atmosphere was moderately unstable over the entire midwestern United States yet intense localized convection was not observed during the morning hours. In order to delineate regions of expected intense afternoon convection, three-hourly variations of stability (Total-Totals) were computed and displayed over the current infrared window cloud imagery on an hourly basis. Figure 31(a) shows the result for 18 GMT. A notable feature is the narrow zone of decreasing stability (positive three-hour tendency of Total-Totals) stretching from Oklahoma across Missouri and southern Illinois into western Indiana (the +2 contour is drawn boldly in Figure 31(a)). Also shown on Figure 31(a) are the surface reports of thunderstjrms which occurred between 21 and 23 GMT. Good correspondence is seen between the past three-hour tendency toward instability and the thunderstorm activity 3 to 5 hours ahead.

Figure 31(b) shows the one hour change in the Total-Totals index between 17 GMT and 18 GMT. The greatest 1-h decrease of atmospheric stability is along the border between northern Missouri and central Illinois where the tornado-producing storm developed during the subsequent three-hour period (see Figure 30(d)). The stability variation shown was the largest one-hour variation over the entire period studies, 12-21 GMT.

A few detailed sounding results will now be presented for the Missouri region. The soundings were retrieved from VAS DS data with high spatial resolution (~75 km) using the interactive processing algorithms described by Smith and Woolf (1981). In Figure 32 radiosonde observations of 700-mb temperature, and 700-mb temperatures retrieved from GOES-5 VAS DS radiance data, are presented for a region surrounding the state of Missouri on 20 July 1981. Figure 33 shows a similar comparison for the 300-mb dewpoint temperature. Even though the VAS values are actually vertical mean values for layers centred about the indicated pressure levels, it can be seen from the 12 GMT observations that the VAS is broadly consistent with the available radiosondes while at the same time delineating important small-scale features which cannot be resolved by the widely spaced radiosondes. This is particularly obvious in the case of moisture (Figure 33) where the horizontal gradients of dewpoint temperature are as great as 10°C over a distance of less than 100 km.

The temporal variations of the atmospheric temperature and moisture over the Missouri region are observed in detail by the three-hour interval VAS observations presented in Figures 32 and 33. For example, in the case of the 700-mb temperature, the VAS observes a warming of the lower troposphere with a tongue of warm air protruding in time from Oklahoma across southern Missouri and northern Arkansas, the maximum temperatures being observed around 18 GMT in this region. Although it is believed to be a real diurnal effect, undetected by the 12-h interval radiosonde data, it is possible that it has been exaggerated by the influence of high skin surface temperature. This problem needs to be investigated further. The temporal variation of upper tropospheric moisture may be seen in Figure 33; a narrow intense moist tongue (high dewpoint temperature) across northwestern Missouri steadily propagates southeastward with time. The dewpoint temperature profile results achieved with the interactive profile retrieval algorithm are consistent with the layer relative humidities achieved automatically in real time (Figure 30). It is noteworthy that over central Missouri, where the intense convective storm developed, the VAS observed a very sharp horizontal gradient of upper tropospheric moisture just prior to and during the storm genesis between 18 and 21 GMT. Here again the inadequacy of the radiosonde network for delineating important spatial and temporal features is obvious. The discrepancy between the 21 GMT VAS and 24 GMT radiosonde observation over southern Illinois (Figure 33) is due to the existence of deep convective clouds. A radiosonde observed a saturated dewpoint value of -34°C in the cloud while VAS was incapable of sounding through the heavily clouded area. Nevertheless it appears that the VAS DS data provide, for the first time, the kind of atmospheric temperature and moisture observations needed for the timely initialization of a mesoscale numerical model for predicting localized weather.

Figure 27 shows streamlines and isotachs of 300-mb gradient winds derived from the VAS temperature profile data, where the curvature term was approximated from the geopotential contours. There is agreement (not shown) between the VAS 12GMT gradient winds and the few radiosonde observations in this region. As can be seen there is a moderately intense subtropical jet streak which propagates east-southeastward with time. Note that at 18 GMT the exit region of the jet is over the area where the severe convective storm developed. As shown by Uccellini and Kocin (1981), the mass adjustments and isallobaric

forcing of a low level jet produced under the exit region of an upper tropospheric jet streak can lead to rapid development of a convectively unstable air mass within a 3- to 6-h time period.

Figure 34 shows the three-hour change of total precipitable water prior to the severe convective storm development. The instantaneous fields from which Figure 34 was derived showed a number of short-term variations. Nevertheless it is probably significant that a local maximum exists over the location of the St. Louis storm prior to its development. It is suspected that the convergence of lower tropospheric water vapour is a major mechanism for the thermodynamic destabilization of the atmosphere leading to severe convection between 18 and 21 GMT along the Missouri-Illinois border.

The VAS geostationary satellite sounder offers exciting new opportunities for real-time monitoring of atmospheric processes and for providing on a timely basis the vertical sounding data at the spatial resolution required for initializing mesoscale weather prediction models. Results from this case study and others not reported here suggest that VAS can detect, several hours in advance, the temperature, moisture, and jet streak conditions forcing severe convective development. This work was reported by Smith et al in 1982.

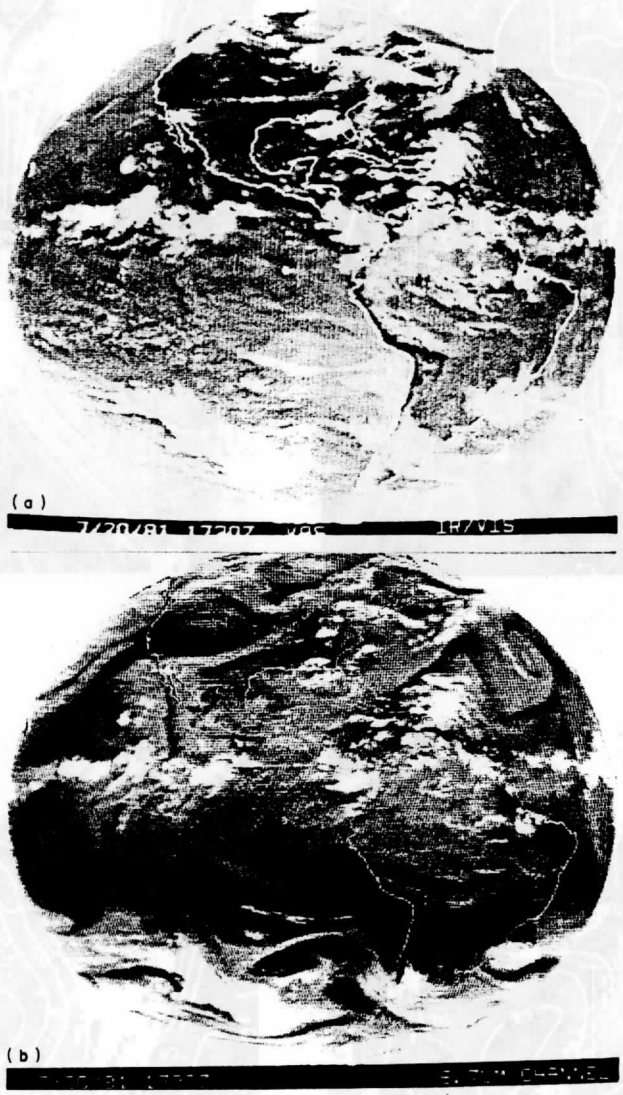

FIGURE 29. Full disk images obtained on 20 July 1981 between 1730 and 1800 GMT:

(a) 11-μm window and
(b) 6.7-μm H_2O.

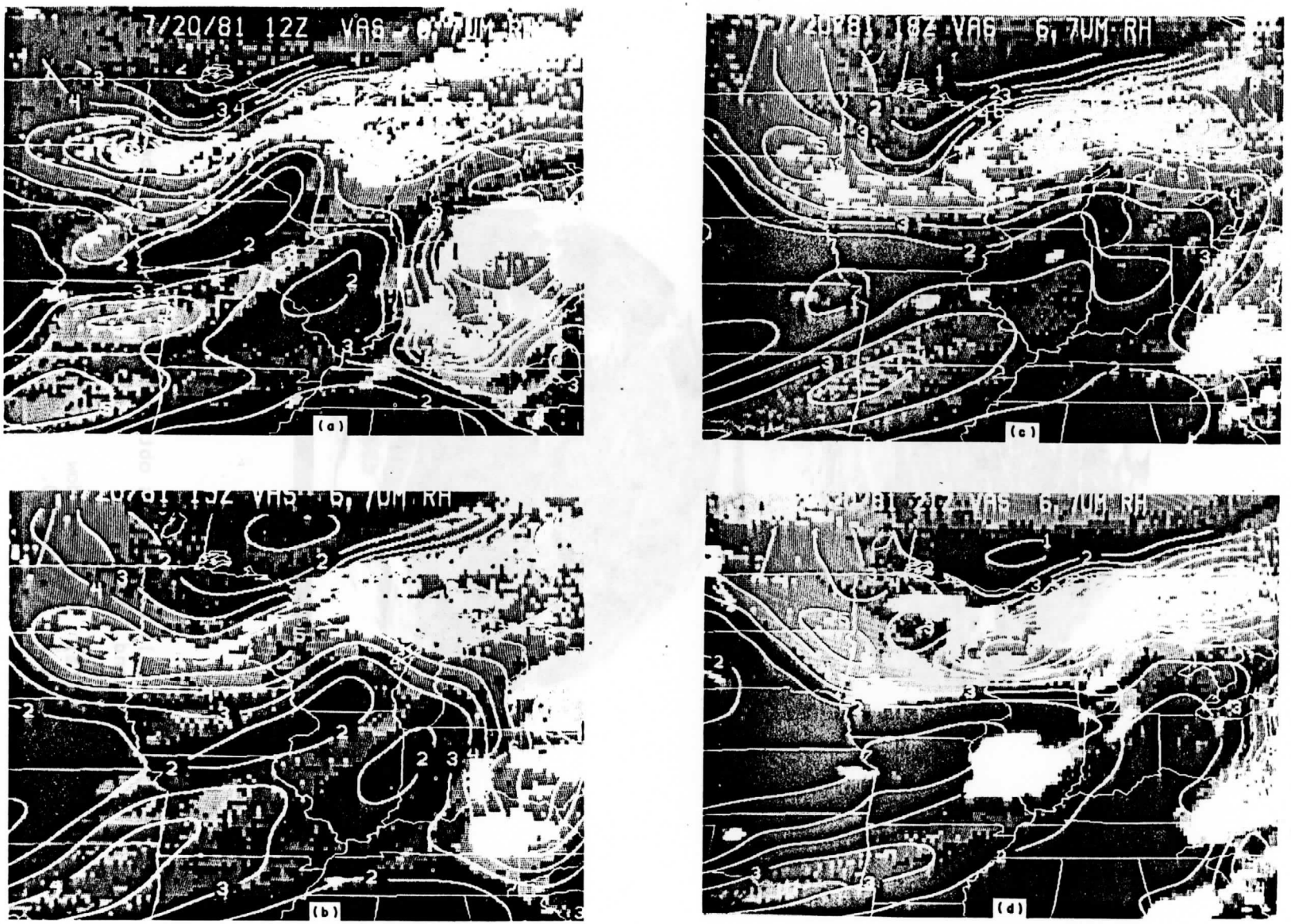

FIGURE 30. Upper tropospheric relative humidity (%/10) over the VAS Image of 6.7-μm atmospheric water vapour radiance emission: (a) 12 GMT; (b) 15 GMT; (c) 18 GMT; and (d) 21 GMT on 20 July, 1981.

FIGURE 31(a). Three-hour variation of VAS derived Total-Totals index (°C) between 15-18 GMT superimposed over the 18-GMT VAS 11- m image of cloudiness. The symbols of thunderstorms (TRW) which were observed between 20 and 23 GMT are also shown,
(b) 1-hour (17018 GMT) variation of Total-Totals index (°C) showing that the maximum one-hour variation (4°C) observed by VAS on 20 July 1981 occurred at the location of and just prior to the development of a severe convective storm.

FIGURE 32. Radiosonde and VAS observations of 700 mb temperature (°C) on 20 July, 1981.

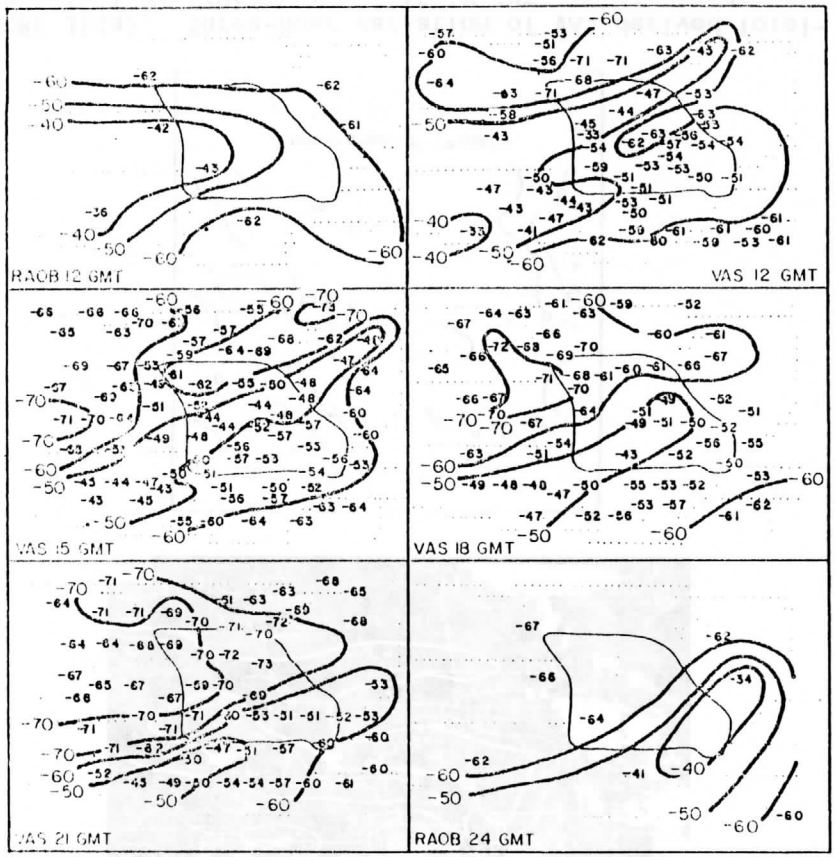

FIGURE 33. Radiosonde and VAS observations of 300-mb dewpoint temperature (°C) on 20 July 1981.

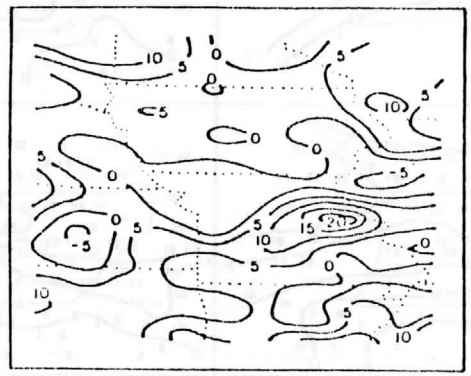

FIGURE 34. Three hour change of precipitable water vapour (mm) between 15 and 18 GMT on 20 July, 1981.

REFERENCES

The following references are a few of the available articles that either summarize an important aspect of Satellite Meteorology or indicate a recent development. They are attached so that the interested reader can delve further.

Anding, D. and Kauth, R. 1970: Estimation of sea surface temperature from space. Remote Sensing of the Environment, 1, 217-220.

Atlas, R., Ghil, M. and Halem, M. 1982: The effect of model resolution and satellite sounding data on GLAS model forecasts. Monthly Weather Review, 110, 662-682.

Bandeen, W.R., Halem, M. and Strange, I. 1965: A radiation climatology in the visible and infrared from the TIROS meteorological satellite. NASA Technical Note, TN-D-2534.

Barton, I.J. 1983: Dual channel satellite measurements of sea surface temperature. Quart. Journal of the Royal Meteorological Society, 60, 197-205.

Bates, J.J. 1982: Sea surface temperatures derived from VAS multispectral data. M.S. Thesis, Department of Meteorology, University of Wisconsin, Madison, Wisconsin, 53706, 40 pp.

Bengtsson, L. 1981: The impact of FGGE on global medium range forecasts. Characteristics of atmospheric planetary circulations and associated model forecast skill during FGGE case studies selected by WGNE. Proceedings of the International Conference on Early Results of FGGE and Large-Scale Aspects of its Monsoon Experiments, Tallahassee, Florida, 12-17 January 1981.

Brower, R.L., Gohrband, H.S., Pichel, W.G., Signore, T.L. and Walton, C.C. 1976: Satellite derived sea surface temperatures from NOAA spacecraft. US Department of Commerce, National Oceanic and Atmospheric Administration, National Environmental Satellite Service, Washington, DC, NOAA Technical Memorandum NESS 78, 74 pp.

Chahine, M.T. 1970: A general realaxation method for inverse solution of the full radiative transfer equation. Journal of Atmospheric Science, 27, 960.

Chahine, M.T. 1974: Remote sounding of cloudy atmospheres, I. The single cloud layer. Journal of Atmospheric Science, 31, 233-243.

Chesters, D., Uccellini, L.W. and Robinson, W. 1982: Low-level water vapour fields from this VISSR Atmospheric Sounder (VAS) "split window" channels at 11 and 12 microns. NASA TM 83951 (available from National Technical Information Service, #82N32914, Washington, DC).

Deschamps, P.Y. and Phulpin, T. 1980: Atmospheric correction of infrared measurements of sea surface temperature using channels at 3.7, 11, and 12 μm. Boundary-Layer Meteorology, 18, 131-145.

Ellis, J. and Vonder Haar, T.H. 1976: Zonal averaged radiation budget measurements from satellites for climate studies. Atmospheric Science Paper #240, Colorado State University, Fort Collins, Colorado.

Fleming, H.E. and Smith, W.L. 1971: Inversion techniques for remote sensing of atmospheric temperature profiles. Reprint from Fifth Symposium on Temperature, Instrument Society of America, 400 Stanwix Street, Pittsburgh, Pennsylvanie, 2239-2250.

Fritz, S., Wark, D.Q., Fleming, H.E., Smith, W.L., Jacobowitz, H., Hilleary, D.T. and Alishouse, J.C. 1972: Temperature sounding from satellites. US Department of Commerce, National Oceanic and Atmospheric Administration, National Environmental Satellite Service, Washington, DC, NOAA Technical Report NESS 59, 49 pp.

Frolich, C. 1977: Contemporary measures of the solar constant, Solar Output and Its Variation. (Ed.) O.R. White, Colorado Associated University Press, Boulder, Colorado, 93-109.

Grody, N.G., Gruber, A. and Shen, W. 1980: Atmospheric water content over the tropical Pacific derived from the Nimbus-6 scanning microwave spectrometer. Journal of Applied Meteorology, 19, 986-996.

Hayden, C.M., Smith, W.L. and Woolf, H.M. 1981: Determination of moisture from NOAA polar orbiting satellite sounding radiances. Journal of Applied Meteorology, 20, 450-466.

Kaplan, L.D., Chahine, M.T., Susskind, J. and Searl, J.E. 1977: Spectral band passes for a high precision satellite sounder. Applied Optics, 16, 322-325.

Ma, X.L., Smith, W.L. and Woolf, H.M. 1983: Total ozone from NOAA satellites - a physical model for obtaining observations with high spatial resolution. Journal of Climate and Applied Meteorology.

McClain, E.P., Pichel, W., Walton, C., Ahmad, A. and Sutton, J. 1982: Multichannel improvements to satellite-derived global sea surface temperatures. Preprint, XXIV COSPAR, Ottawa, Canada, 22-29 May, 1982.

McMillin, L.M., Wark, D.Q., Siomkajlo, J.M., Abel, P.G., Werbowetzki, A., Lauritson, L.A., Pritchard, J.A., Crosby, D.S., Woolf, H.M., Luebbe, R.C., Weinreb, M.P., Fleming, H.E., Bittner, F.E. and Hayden, C.M. 1973: Satellite infrared soundings from NOAA Spacecraft. US Department of Commerce, National Oceanic and Atmospheric Administration, National Environmental Satellite Service, Washington, DC, NOAA Technical Report NESS 65, 112 pp.

McMillin, L.M. and Fleming H.E. 1976: Atmospheric transmittance of an absorbing gas: a computationally fast and accurate transmittance model for absorbing gases with constant mixing ratios in homogeneous atmospheres. Applied Optics, 15, 358.

McMillin, L.M. and Dean, C. 1982: Evaluation of a new operational technique for producing clear radiances. Journal of Applied Meteorology, 12, 1005-1014.

Menzel, W.P., Smith, W.L. and Stewart, T. 1983: Improved cloud motion wind vector and altitude assignment using VAS. Journal of Applied Meteorology.

Phillips, N.A., McMillin, L.M., Wark, D. and Gruber, A. 1979: An evaluation of early operational temperature soundings from TIROS-N. Bulletin of the American Meteorological Society, 60, 118-1197.

Prabhakara, C., Dalu, G. and Kunde, V.G. 1974: Estimation of sea surface temperature from remote sensing in the 11 to 13 μm window region. Journal of Geophysical Research, 79, 5039-5044.

Rodgers, C.D. 1971: Some theoretical aspects of remote sounding in the earth's atmosphere. Journal of Quant. Spectrosc. Radiation Transfer, 11, 767.

Rodgers, C.D. 1976: Retrieval of atmospheric temperature and composition from remote measurements of thermal radiation. Rev. of Geophysics and Space Physics, 14, 609-624.

Rosenkranz, P.W., Komichak, M.J. and Staelin, D.H. 1982: A method for estimation of atmospheric water vapour profiles by microwave radiometry. Journal of Applied Meteorology, 21, 1364-1370.

Schnapf, A. 1982: The development of the TIROS global environmental satellite system. NASA Conference Publication 2227: Meteorological Satellites-Past, Present and Future (available from NASA Scientific and Technical Information Branch, Washington, DC, 20546).

Smith, W.L. 1970: Iterative solution of the radiative transfer equation for temperature and abssorbing gas profiles of an atmosphere. Applied Optics, 9, 1993-1999.

Smith, W.L. and Howell, H.B. 1971: Vertical distribution of atmospheric water vapour from satellite infrared spectrometer measurements. Journal of Applied Meteorology, 10, 1026.

Smith, W.L., Woolf, H.M. and Fleming, H.E. 1972: Retrieval of atmospheric temperature profiles from satellite measurements for dynamical forecasting. Journal of Applied Meteorology, 11, 113.

Smith, W.L. and Woolf, H.M. 1976: The use of eigenvectors of statistical convariance matrices for interpreting satellite sounding radiometer observations. Journal of Atmospheric Science, 35(7), 1127-1140.

Smith, W.L., Woolf, H.M., Hayden, C.M., Wark, D.Q. and McMillin, L.M. 1979: The TIROS-N operational vertical sounder. Bulletin of the American Meteorological Society, 60, 1177-1187.

Smith, W.L., Suomi, V.E., Menzel, W.P., Woolf, H.M., Sromovsky, L.A., Revercomb, H.E., Hayden, C.M., Erickson, D.N. and Mosher, F.R. 1981: First sounding results from VAS-D. Bulletin of the American Meteorology Society, 62, 232-236.

Smith, W.L., Suomi, V.E. Zhou, F.X. and Menzel, W.P. 1982: Nowcasting applications of geostationary satellite atmospheric sounding data. Published in Nowcasting, K.A. Browning (ed.), Academic Press Inc. (London) Ltd., pp. 123-135.

Smith, W.L. and Zhou, F.X. 1982: Rapid extraction of layer relative humidity, geopotential thickness, and atmospheric stability from satellite sounding radiometer data. Applied Optics, 21, 924-928.

Staelin, D.H. 1976: Measurements and interpretation of the microwave spectrum of the terrestrial atmosphere near 1-cm wavelength. Journal of Geophysical Research, 71, 2875.

Staelin, D.H., Kunzi, K.F., Pettyjohn, R.L., Poon, R.K.L., Wilsox, R.W. and Waters, J.W. 1976: Remote sensing of atmospheric water vapour and liquid water with the Nimbus-5 microwave spectrometer. Journal of Applied Meteorology, 15, 1204-1214.

Strand, O.N. and Westwater, E.R. 1968: Statistical estimation of the numerical solution of a Fredholm integral equation of the first kind. J. Ass. Comput. Mach., 15, 100.

Suomi, V.E. 1958: The radiation balance of the earth from a satellite. Annals of the IGY, Vol. I, pp. 331-340.

Suomi, V.E., Fox, R., Limaye, S.S. and Smith, W.L. 1982: McIDAS III: A modern interactive data access and analysis system. Submitted to Journal of Applied Meteorology.

Twomey, S. 1977: An introduction to the mathematics of inversion in remote sensing and indirect measurements. Elsevier, New York.

Uccellini, L.W. and Johnson, D.R. 1979: The coupling of upper and lower tropospheric jet streaks and implications for the development of severe convective storms. Monthly Weather Review, 107, 682-703.

Veldon, C.S. and Smith, W.L. 1983: Monitoring tropical cyclone evolution with NOAA satellite microwave observations. Journal of Applied Meteorology.

Veldon, C.S., Smith, W.L., Mayfield, M. and Burpee, R.W. 1983: Applications of VAS and TOVS to tropical cyclones. Bulletin of the American Meteorological Society.

Vonder Haar, T.H., Campbell, G.G., Smith E.A., Arking, A., Coulson, K., Hickey, J., House, F., Ingersoll, A., Jacobowitz, H., Smith, L. and Stowe, L. 1981: Measurements of the earth radiation budget from satellites during the First GARP Global Experiment. Advance Space Research, 1, 285-297. COSPAR.

Walton, C. 1980: Deriving sea surface temperatures from TIROS-N data. Remote Sensing of Atmospheres and Oceans, Academic Press, 547-579.

Wark, D.Q. and Fleming, H.E. 1966: Indirect measurements of atmospheric temperature profiles from satellites, 1. Introduction. Monthly Weather Review, 94, 351.

Weinreb, M.P. and Crosby, D.S. 1972: Optimization of spectral intervals for remote sensing of atmospheric temperature profiles. Remote Sensing of the Environment, 2, 193-201.

Zandlo, J.A., Smith, W.L., Menzel, W.P. and Hayden, C.M. 1982: Surface temperature determination from an amalgamation of GOES and TIROS-N radiance measurements. Applied Meteorology, 21, 44-50.